SCUOLA DI DOTTORATO
UNIVERSITÀ DEGLI STUDI DI MILANO-BICOCCA

Department of Earth and Environmental Sciences

PhD program in Chemical, Geological and Environmental Sciences, XXX Cycle

Curriculum in Mediterranean Marine Sciences

INTERACTIONS BETWEEN THE OCEAN AND EXTREME METEOROLOGICAL EVENTS

Candidate Agostino Niyonkuru MERONI

Registration number 727604

Tutor Prof. Claudia PASQUERO

Coordinator Prof. Maria Luce FREZZOTTI

Academic year 2017-2018

Urukundo ntirwiziganiriza.

L'amicizia non conserva nulla per sé.

Proverbio kirundi, Burundi

Abstract

Ocean-atmosphere interactions are of paramount importance in both climatic and meteorological contexts. They are known to play important roles from hourly time scales, such as in the intensification of tropical cyclones, to interannual and even longer time scales, such as in El Niño Southern Oscillation mode of variability of the climate system. The focus of this thesis has been on the energy and momentum transfers at the air-sea interface in short time scales processes characterized by extreme conditions. Both the oceanic dynamical response to an extreme atmospheric forcing and the effects of the sea state on the development of a meteorological extreme event are considered. The systems under study are the ocean internal wave field in the wake of a tropical cyclone and the role of the upper ocean thermal structure on the development of heavy rainfalls in the Mediterranean sea.

In particular, the energy exchanges among oceanic internal waves in the wake of an idealized tropical cyclone are studied with a theoretical approach supported by relevant numerical simulations run with a state-of-the-art oceanic numerical model. The purpose of this work is to understand how tropical cyclones might contribute to the internal ocean mixing in locations far from their track. In fact, despite their intermittency in space and time, tropical cyclones are characterized by very intense winds, which are known to excite oceanic internal waves. These, by radiating the energy input by the winds are thought to contribute to ocean mixing far from their generation site through their breaking. Since the energy propagation is linked to the spectral features of the waves, a detailed description of the energy partitioning in different vertical modes and frequencies helps to better constrain the extent and the velocity of such energy propagation. A new detailed analytical description of the exchanges leading to the formation of the first superinertial peak is introduced on the basis of the theory developed. Compared to previous works, a realistic oceanic stratification is included and a path for the energy cascade from the large scales of the atmospheric forcing to the small scales of the mixing is highlighted.

The second category of extreme events considered are the so-called heavy-rain-producing mesoscale convective systems (MCSs). They are common phenomena along the coasts of the Mediterranean sea and they generally trigger intense hydrological responses, since they release large amount of rain in few hours and over relatively small areas, $O(100\ \mathrm{km}^2)$. It is known that an average warmer sea in the vicinity of their location produces a larger volume of rain, but before this thesis work no information was available on the influence that a spatial pattern of sea surface temperature (SST), with structures on the kilometric scale, might have on the precipitation event. Appropriate atmospheric numerical simulations, run with a non-hydrostatic primitive equation model, shed light on the mechanisms through which submesoscale SST oceanic features can influence the surface wind structure and, in turns, can affect the evolution of the heavy rainfall. It is found that through enhanced vertical momentum mixing in the atmosphere over warmer SST areas, the presence of temperature fronts in the sea can significantly affect the surface wind convergence, which is often the trigger for deep convection in MCSs, over hourly time scales. This might also lead to significant displacement of the rain bands.

In the second place, the possibility of an ocean dynamical feedback related to the vertical temperature profile is introduced. By means of atmosphere-ocean coupled numerical simulations, it is found that in particular conditions the intense winds in which the MCS is embedded can mix the upper ocean strongly enough to enhance the stability of the atmospheric boundary layer and suppress deep convection. Such conditions are characterized by shallow mixed layer and strong stratification, which are typical of the late summer period. It is suggested that this is the reason why heavy-rain-producing MCSs are generally observed later during the year, when the mixed layer is deeper and this oceanic mitigating effect is absent.

Contents

Contents **vi**

1 Introduction **1**
1.1 Some GFD properties . . . 3
1.2 Meteo-climatic extremes . . . 11
1.3 Outline . . . 13

2 Nonlinear wave interactions in the wake of a tropical cyclone **15**
2.1 Introduction . . . 15
2.2 Numerical model and equations of motion . . . 21
2.3 Internal mode decomposition . . . 23
2.4 Analytical spectral decomposition . . . 30
2.5 Results . . . 36
2.6 Discussion and conclusions . . . 42
2.7 Comparison with observations . . . 47

3 SST role in the modulation of HPEs **51**
3.1 Introduction . . . 51
3.2 Numerical simulations . . . 58
3.3 The simulated event . . . 62
3.4 Analysis . . . 63
3.5 Results . . . 67
3.6 Discussion and conclusions . . . 75

4 Oceanic vertical thermal structure role in the modulation of HPEs **81**
4.1 Introduction . . . 81
4.2 Setup of the numerical simulations . . . 83
4.3 Effect of the ocean-atmosphere coupling . . . 87
4.4 Role of the vertical oceanic thermal structure . . . 90
4.5 Discussion and conclusions . . . 96

5 Conclusions **101**
5.1 Oceanic internal wave interactions in the wake of a tropical cyclone 101
5.2 Importance of the upper ocean thermal state on heavy-rain-producing MCS dynamics 103
Ringraziamenti 107

Bibliography **109**

One

Introduction

The driver of the earth climate system is the sun. It supplies our planet with its energy in the form of radiation, which is partially reflected and partially absorbed by the earth system. A large fraction of the incoming radiation, which roughly corresponds to the visible range of the electromagnetic spectrum (0.39-0.70 μm), goes through the atmosphere and reaches the earth surface. In particular, 23% is absorbed by the atmosphere, roughly the same amount is scattered by clouds and only 7% is reflected on average by the surface. The remaining radiation, which is almost half of the incoming amount, is absorbed by lands and oceans (Trenberth et al., 2009).

The temperature of the earth surface, controlled by the incoming solar energy input, determines in the black body approximation the thermal radiation emission according to the well-known Stefan-Boltzmann law, which predicts that the emitted radiative energy flux (in units of energy per unit time per unit area) is proportional to the fourth power of the temperature of the body. At equilibrium, this outgoing emitted radiation is equal to the absorbed one.

Figure 1.1 shows in the upper panel (a) the blackbody spectra representative of the sun on the left and of the earth on the right. The values under the curves indicate the corresponding blackbody temperatures. Panels (b) shows the spectrum of monochromatic absorptivity of the part of the atmosphere above 11 km and panel (c) of the whole atmosphere. From this figure one can infer that, firstly, the atmosphere is almost transparent to the visible radiation, as shown by the presence of a window of absorption near the solar blackbody spectral peak. Secondly, the greenhouse gases (water vapor H_2O, carbon dioxide CO_2, methane CH_4, ozone O_3 and nitrous oxide N_2O indicated in the figure) absorb a large fraction of the longwave radiation emitted by the earth, as opposed to the shortwave radiation emitted by the sun, through different absorption modes, e.g. vibrational and rotational ones (Wallace and Hobbs, 2006).

The energy absorbed by the greenhouse gases diluted in the atmosphere partially drives the atmospheric dynamics. In particular, since the atmosphere is mostly heated from below as a result of the greenhouse gases absorption, convective updrafts are continuously formed because of the locally unstable vertical density profile generated. Other factors controlling the atmospheric dynamics include the latitudinal radiative input dependence, that primarily drives zonal motions through meridional pressure gradients;

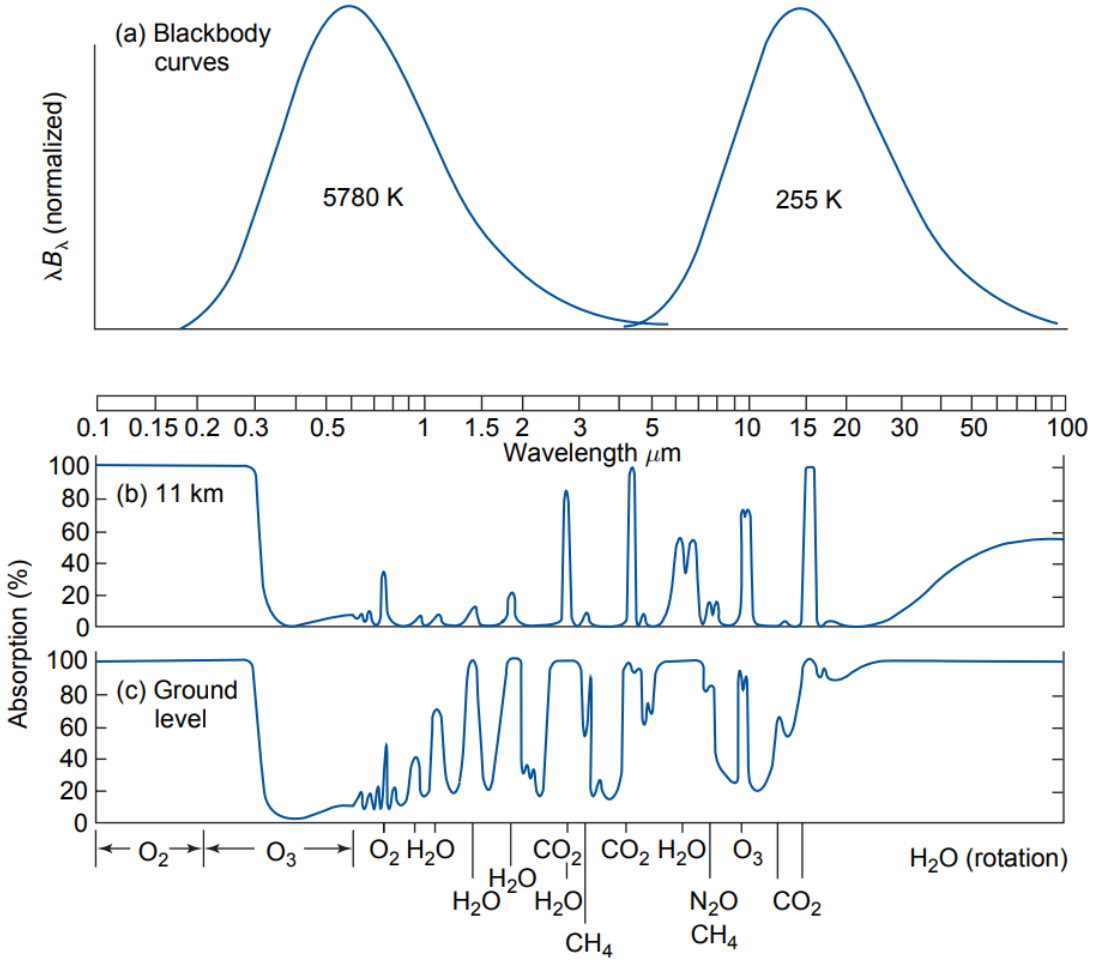

Figure 1.1: (a): Blackbody spectra for the sun (left) and the earth (right). In the other panels, monochromatic absorptivity spectra at 11 km above ground level, i.e. above the troposphere, (b) and at the ground level (c) (Wallace and Hobbs, 2006).

the background rotation of the planet, that introduces non-inertial terms in the equations of motion and generates circular inertial trajectories; and the latent heat due to the evaporation at the marine surface, controlled by local temperature and humidity.

As for ocean dynamics, it is also controlled by a variety of factors including rotation, density changes at the surface (for example due to phase transitions or river and precipitation freshwater inputs) and wind forcing, to cite some. The ocean-atmosphere system is highly connected and strongly interacts with the other components of the earth system, including the cryosphere, the biosphere and the lithosphere. Ocean and atmosphere dynamics share some common features but also have their peculiarities. They are both referred to with the name of geophysical fluid dynamics (GFD), which is the branch of fluid dynamics characterized by the crucial importance of rotation and stratification (i.e. vertical density structure).

Indeed, the complexity of geophysical flows is due to their nonlinear behavior, which, being dominated by turbulence, connects all possible scales of motion and thus determines the well known chaotic nature of the weather and climate system.

1.1 Some GFD properties

Here, some aspects of oceanic and atmospheric dynamics, relevant for the analysis described in the following chapters, are reviewed.

Air-sea contrasts

As mentioned above, oceans and atmosphere, highly connected and dynamically driven by the radiative solar energy input, share some common dynamical features but also have substantial differences. Among these, there are a remarkable density contrast and some differences in thermal and optical properties, that make the air-sea interface a place of particular interest (Gill, 1982).

The density difference, with a factor of roughly 800 between the two fluids (considering the air density at the sea level to be 1.2 kg m^{-3} and the seawater one around 1025 kg m^{-3}), imposes that the interface is very stable under the relatively strong restoring pull due to gravity. Such an important density contrast also determines that the mass of the ocean is by far greater than the mass of the entire atmosphere, which is directly the cause of the very high pressure of the oceanic environments (the atmospheric pressure is equated by the first upper 10 m of seawater) and of the difference in heat capacity. In fact, not only is the density of seawater much greater than the air density, but also the specific heat is larger for water than for air. This means that the heat capacity per unit area (i.e. the amount of energy necessary to change by 1 K the temperature of a column of 1 m^2 of the fluid body considered) of the entire atmosphere is equal to the heat capacity per unit area of just a layer of 2.5 m of ocean. This is one of the most important reasons why atmosphere and oceans play different roles in the climate system. In particular, the ocean, being characterized by slower velocity scales and such a large thermal inertia, introduces the long time scales in the climate system. It responds to

the radiative forcing over longer time scales with respect to the atmosphere, which is a crucial element that determines the internal variability of the system.

Concerning the optical properties, eventually related to the chemical composition of the two fluids, while the atmosphere is almost transparent to the visible incoming solar radiation, as metioned above, the sea quickly absorbs the incident energy flux, so that roughly 80% of the radiation that hits the ocean surface is absorbed in the first 10 m of water. In fact, in the vertical direction the intensity of the radiation in the ocean decays exponentially with typical e-folding lengths of the order $O(1 - 10 \text{ m})$, according to the concentration of suspended materials (the more concentrated the suspensions, the more energy is absorbed).

At the air-sea interface, then, momentum, heat and moisture are exchanged between the two fluids. These exchanges, characterized by a complex turbulent nature, provide the energy to drive a lot of different processes and, for example, are crucial in the control of the ocean currents, the intensity of tropical cyclones and the generation of intense rains. In fact, it is well known that across different length scales winds are a major driver of oceanic motions. To cite some, the large-scale circulation of the gyres is controlled by the latitudinal structure of the zonal winds, but also the local surface Ekman boundary layer is controlled by the wind stress input (Vallis, 2006). At the small scales, momentum is transferred to the sea through pressure differences across the irregularities of the sea surface, i.e. the waves, or by viscous stresses.

In particular, the wind stress imposed by a wind of velocity u near the sea surface, is generally put in the form

$$\tau = c_D \rho_{air} u^2, \tag{1.1}$$

where τ is the force per unit area that acts in a direction parallel to the sea surface (which is physically equivalent to a transfer of linear momentum per unit time per unit area), c_D is a dimensionless parameter that is called drag coefficient and depends on the surface roughness, the wind speed itself and the stability of the air column, and ρ_{air} is the air density (Gill, 1982).

Since the Ekman transport, i.e. the linear momentum per unit volume integrated in the vertical direction over the surface Ekman layer depth, which is the layer directly moved by the winds, is proportional to the wind stress magnitude, there is a nonlinear dependence of the water mass velocity on the wind speed. This is contained both in the quadratic dependence of the wind stress on the wind speed, and in the dependence of the drag coefficient on the wind speed, as well. Associated with this nonlinear relation, the fact that the surface currents are stronger when the wind is stronger produces an intense vertical shear that drives, in turns, vigorous vertical mixing via shear turbulence production. Vertical mixing is thus a nonlinear function of the wind speed. This indicates that extreme wind events might play an important role as oceanic internal mixing sources, even if intermittent and localized. This is the reason why tropical cyclones, which are the large-scale systems with the most intense wind magnitude on earth, are thought to contribute significantly to the ocean interior mixing.

Back to equation (1.1) the value of u is generally chosen to be the anemometer height (usually $z = 10$ m) wind speed. Similarly, the upward heat and moisture fluxes

are written in the form

$$Q_s = c_H \rho_{air} c_p u (T_{sea} - T_{air}) \tag{1.2}$$

and

$$E = c_E \rho_{air} u (q^*_{sea} - q_{air}), \tag{1.3}$$

respectively. Q_s is the sensible heat flux due to the local temperature difference between the fluids $T_{sea} - T_{air}$ and it depends on the wind speed u, the air heat capacity per unit volume $\rho_{air} c_p$ and another dimensionless number c_H that changes with the atmospheric stability. Instead, E is the mass of the water evaporated per unit time per unit area and is expressed as a function of the super-saturation $q^*_{sea} - q_{air}$ (q^*_{sea} being the saturation value of specific humidity of air at the sea surface temperature and q_{air} the specific humidity at the anemometer height, which are all defined in details in the subsection dedicated to atmospheric conditional instability), the wind speed u and the air density ρ_{air}. A third nondimensional number c_E is introduced and, as the other two, c_D and c_H, is obtained empirically (Gill, 1982; Fairall et al., 2003).

Evaporation contributes to another form of heat exchange between ocean and atmosphere. In fact, once the seawater evaporates and is transported in the form of water vapor in a location where the temperature decreases and the air becomes saturated, condensation takes place and water droplets are formed. This releases latent heat that can provide an additional buoyancy forcing in the atmospheric dynamics. In fact, if the air mass finds itself to be less dense than its surroundings, it starts floating. There is, thus, a net heat transfer from the location where the evaporation takes place to the location where the water vapor condenses. Considering the average atmospheric circulation, water molecules in the gaseous phase can be displaced $O(10^3$ km) meridionally and $O(10^4$ km) zonally (Gill, 1982).

Summarizing, the net energy balance at the ocean surface comprises the incoming shortwave solar radiation, the thermal longwave emitted by the ocean itself, the sensible heat flux due to the air-sea temperature difference and the latent heat flux due to the evaporation and condensation processes.

Oceanic kinetic energy

Considering, now, ocean dynamics, it is well known to be mainly driven by winds. The large-scale wind patterns, with their latitudinal structure, are in fact responsible for the large-scale oceanic gyres through the Ekman and the geostrophic balances. In particular, in the upper ocean, where turbulence is the strongest, the balance between turbulent viscous stresses and the Coriolis acceleration, named Ekman balance, determines the net displacement of water masses in the direction perpendicular to the roughly zonal wind stress vector field. This, inducing regions of convergence and divergence in the ocean, produces pressure gradients that drive the oceanic gyres by compensating the Coriolis acceleration in the so-called geostrophic balance (Vallis, 2006).

It is interesting to underline that not only is the energy of the winds trasferred to the ocean directly as kinetic energy, but it also happens to feed the oceanic potential energy reservoir. In fact, the Ekman-driven convergence and divergence regions mentioned

above induce a net elevation of the center of mass of the ocean, by pulling downward light water at the tropics and by pulling upward dense water in the subpolar regions. It is mainly through the so-called baroclinic instability, due to the collapse of lateral density gradients, that potential energy is then converted into kinetic energy (Ferrari and Wunsch, 2009).

Roughly 90% of the oceanic kinetic energy is contained in the geostrophic eddies, that are formed from instabilities of the mean large-scale currents driven by the winds. Such structures are known to be characterized by low vertical shear, which means that they do not contribute to ocean internal mixing. In fact, high values of shear are needed to produce instabilities that generate three dimensional turbulence and, thus, molecular mixing. Such high values of shear are typical of another class of oceanic motions, namely the internal waves (Ferrari and Wunsch, 2009). After recalling the definition of the Coriolis parameter $f = 2\Omega \sin \phi$, where Ω is the earth angular velocity and ϕ is the latitude, a rough distinction between geostrophic eddies and internal waves can be done: while the former dominate the subinertial ($< f$) range, the latter are superinertial ($> f$). Most of the internal wave energy, then, is observed to be in the near-inertial range ($\sim f$).

Near-inertial internal waves, that are almost ubiquitous in the ocean (Garrett and Munk, 1972, 1975, 1979), are generated by all sort of processes including direct wind forcing, resonant higher frequency wave-wave interactions, tide-topography interactions and all the non-geostrophically balanced motions that tend to an equilibrium in the so-called geostrophic adjustment process. Despite they have been known and observed for a long time, some aspects of the internal wave dynamics, such as the energy exchanges and how they take part in the energy cascade towards the mixing scales, are still to be fully understood and thus are object of active research. As an example, it was mentioned that near-inertial internal waves are thought to produce a significant fraction of the ocean interior mixing through their breaking. But near-inertial internal waves excited by wind forcing generally have a low mode vertical structure, meaning that they are characterized by low values of vertical shear. But open ocean observations have found evidences of high vertical mode near-inertial internal waves (Ferrari and Wunsch, 2009). The origin of these waves is still unclear, but a good candidate is the nonlinear interaction between waves that allows for cross-scale energy transfer. Following this idea, in this thesis the interactions between internal waves in the wake of tropical cyclones, which are responsible for the most intense large-scale winds on the planet, are studied and described in chapter 2.

Atmospheric conditional instability

Another key dynamical process related to the peculiar atmospheric condition of being heated from below is the so-called conditional instability. As mentioned before, in fact, the atmosphere is almost transparent to the solar shortwave radiation, while the underlying lands and oceans are not. This means that it is the increased surface temperature that warms up the atmosphere from below through sensible heat fluxes, simply due to the temperature difference and longwave radiation that gets trapped in the atmosphere by

greenhouse gases. Over the sea, then, an increased surface temperature means enhanced evaporation which, in turns, increases the latent heat flux to the atmosphere.

The mechanism of conditional instability is here reviewed following Wallace and Hobbs (2006) because both extreme meteorological events studied in this thesis, tropical cyclones and mesoscale convective systems, crucially depend on it.

Take an air parcel and let T be its temperature, p its pressure, c_p its specific heat and z the vertical coordinate that increases in the direction against the local effective geopotential acceleration g. If the air parcel is dry or it contains some water vapor, but it remains unsaturated (as clarified below), the dry adiabatic lapse rate Γ_d is defined to be the temperature variation that the parcel would undergo if it was moved adiabatically in the vertical direction. Γ_d is found to be

$$-\frac{\mathrm{d}T}{\mathrm{d}z} = \Gamma_d = \frac{g}{c_p}. \tag{1.4}$$

It corresponds to the conservation, along the vertical motion, of the so-called potential temperature θ, which is in fact the temperature that the air parcel would have if brought adiabatically to a reference pressure p_0. This dry lapse rate defines the concept of static stability. Imagine Γ_d to be steeper that the measured temperature variation in the vertical Γ, namely $\Gamma < \Gamma_d$. This means that if the air parcel is quickly moved upward, its temperature decreases in response to the adiabatic expansion at lower pressure so that it is cooler than the surrounding environmental air. Thus, it is negatively buoyant and it moves downward towards its initial position. The stratification is said to be statically stable. If, instead, the environmental lapse rate is steeper than the dry one, namely $\Gamma > \Gamma_d$, even if the parcel is adiabatically cooled in the upward vertical motion, it remains warmer than its surroundings and, thus, it is positively buoyant and keeps moving upward, in a condition that is called static instability. Figure 1.2 schematically shows these two situations: in panel (a) the profile is statically stable and in panel (b) it is statically unstable.

The presence of water vapor in the atmosphere makes things more complex and different quantities are defined to measure it. For example, in a certain volume of air, the ratio of the mass of water vapor m_v and the mass of dry air m_d is called mixing ratio $w = m_v/m_d$, while the ratio of the water vapor mass m_v to the total air parcel mass $m_v + m_d$ is called specific humidity $q = m_v/(m_d + m_v)$. It follows that the relation between mixing ratio and specific humidity is $q = w/(1+w)$. Given a certain temperature T, then, an air mass is said to be saturated (generally with respect to a plane surface of pure water at the same temperature T) if the rate of condensation and the rate of evaporation are equal. The amount of water vapour that corresponds to this equilibrium condition m_v^* can thus be used to define the saturation mixing ratio $w^* = m_v^*/m_d$ or equivalently the saturation specific humidity $q^* = m_v^*/(m_d + m_v^*)$, which eventually only depend on the air mass temperature T through the Clausius-Clapeyron equation. If the rate of evaporation is larger than the rate of condensation, instead, the air parcel is said to be unsaturated.

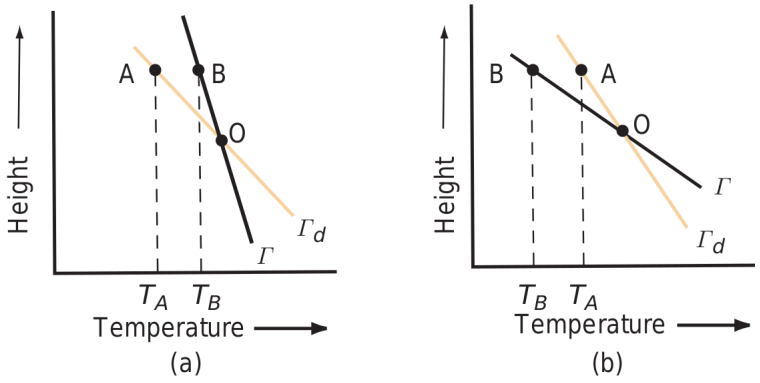

Figure 1.2: (a): Static stability where the dry adiabatic lapse rate Γ_d is steeper than the environmental one Γ, i.e. $\Gamma < \Gamma_d$. (b): Static instability, $\Gamma > \Gamma_d$ (Wallace and Hobbs, 2006).

The inclusion of moisture leads to the definition of the equivalent potential temperature θ_e, which is defined in the same way as θ with the additional condition that all the water vapor condenses and rains out of the air parcel. Conservation of the equivalent potential temperature leads to the definition of the saturated adiabatic lapse rate Γ_s, which depends on pressure and temperature and, since in the condensation process latent heat is released, Γ_s is always smaller than its dry counterpart, namely $\Gamma_s < \Gamma_d$. This means that a saturated air parcel cools at a slower rate while ascending adiabatically with respect to a dry one with the same initial properties, because it is warmed by the latent heat of condensation.

The fundamental concept of conditional instability, which is exclusive of a moist atmosphere and of a saline ocean (Pasquero, 2016), naturally arises. Take a moist air parcel and move it adiabatically upward. As far as it is unsaturated, its temperature changes following the dry adiabatic lapse rate because no latent heat is released and, according to the environmental profile it might be statically stable or unstable. Consider that it is locally stable, i.e. $\Gamma < \Gamma_d$, but the upward motion continues forced by an external factor. At a certain pressure, called lifting condensation level (LCL), the air parcel is so cold that it is saturated and the water vapor starts condensing releasing heat. The adiabatic temperature profile now follows the trend of the local saturated lapse rate, which might warm the air parcel enough to be positively buoyant. If this is the case, the level where this happens is called level of free convection (LFC) and the air parcel starts floating in the environment and moves upward freely. The name of conditional instability comes from the fact that the instability is conditioned on a large enough vertical displacement, to overcome the initial behavior of static stability. Figure 1.3 shows a schematic of such a situation and indicates that the conditional instability is possible when $\Gamma_s < \Gamma < \Gamma_d$. In a moist atmosphere, then, the concepts of static

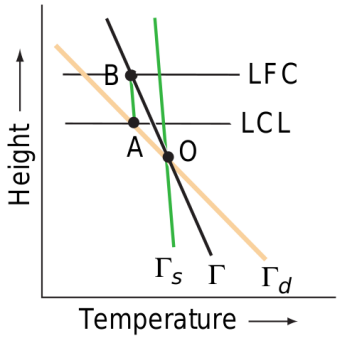

Figure 1.3: Schematic showing a situation of conditional instability, where the environmental lapse rate is between the saturated and the dry one, namely $\Gamma_s < \Gamma < \Gamma_d$ (Wallace and Hobbs, 2006).

stability and instability are generally referred to with the name of absolute stability, when $\Gamma < \Gamma_s < \Gamma_d$, and absolute instability, when $\Gamma > \Gamma_d > \Gamma_s$.

It is common practice, for reasons that will be clarified in what follows, to plot the measured temperature sounding in a so-called skew $T - \log p$ chart, in which the ordinate is $y = -\log p$ and the abscissa is $x = T - C \log p$ where C is a positive arbitrary constant. Different sets of lines are generally plotted in the background to help the reader interpret the data. Figure 1.4 shows an example of such a chart where the red thin lines are isotherms (lines of constant temperature T), the yellow thin lines are dry adiabats (constant potential temperature θ), solid dark green lines are moist adiabats (constant equivalent potential temperature θ_e) and the dashed light green ones are lines of constant saturated mixing ratio w^*. In the same figure, a hypothetical sounding is plotted as a solid thick red line, with the temperature of the surface air parcel marked with T on the horizontal axis together with the corresponding value of the dewpoint temperature T_d, which is another measure of air humidity. In fact, it tells the temperature at which an unsaturated air parcel would need to be cooled down to in order to be saturated, given its moisture content. The adiabatic vertical temperature profile of the surface parcel is also highlighted as a solid line: from the surface to the LCL it follows a dry adiabat (yellow), then, since the air parcel becomes saturated (in fact the dry adiabat intercepts the line of constant saturated mixing ratio that corresponds to the initial dewpoint temperature), it follows a moist adiabat (green). The meaning of the shaded areas defined between the sounding and the vertical adiabatic profile, are the energy per unit mass required to overcome the initially stable stratification and reach the LFC, called convective inhibition (CIN), and the energy per unit mass that can be released in the free ascent when the air parcel is positively buoyant, also known as convective available potential energy (CAPE). In the figure, the lifting condensation level (LCL), where the air parcel becomes saturated; the level of free convection (LFC), where the parcel starts

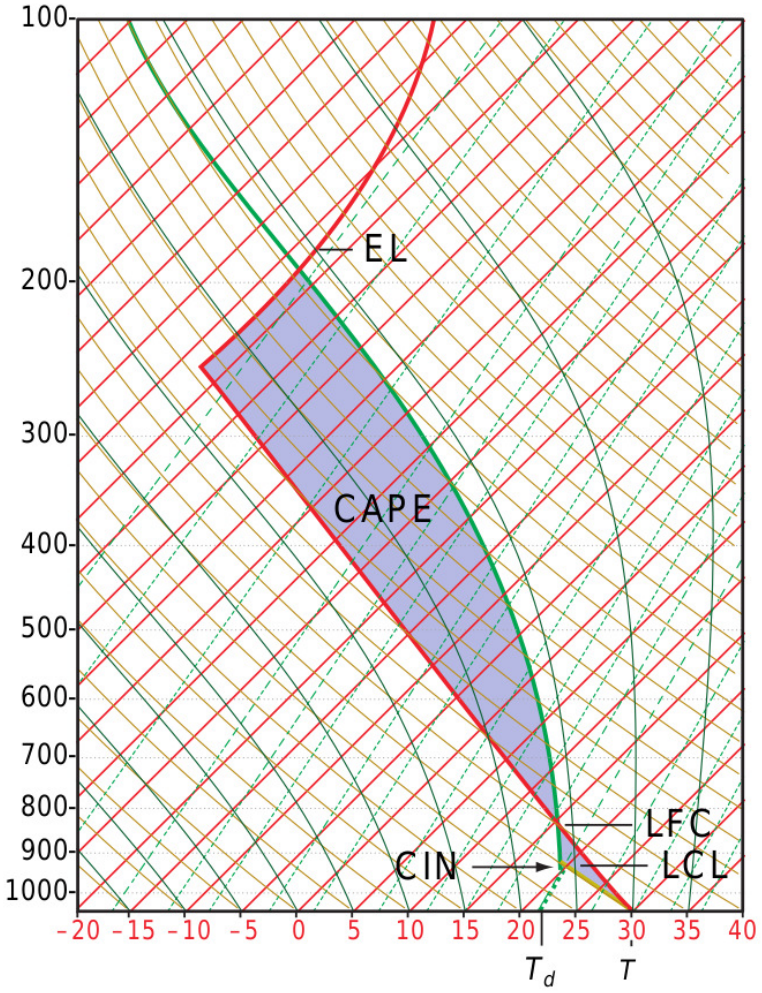

Figure 1.4: Hypothetical sounding used to illustrate the meaning of CIN and CAPE on a skew $T - \log p$ chart (Wallace and Hobbs, 2006).

being buoyant; and the equilibrium level (EL), where the parcel stops being buoyant, are indicated. Mathematically, the CAPE is defined as the vertical integral between the LFC and the EL of the buoyancy force F per unit mass, namely

$$\text{CAPE} = \int_{\text{LFC}}^{\text{EL}} \mathrm{d}z \, \frac{F}{\rho}, \tag{1.5}$$

where ρ is the air density. According to the above definition, the CAPE can be shown to be equivalent to the area highlighted in figure 1.4, which is the reason why the skew $T - \log p$ chart is so widely used in meteorology (Wallace and Hobbs, 2006).

1.2 Meteo-climatic extremes

Sometimes, the climate system evolves in unusual ways and, among all its possible realizations, visits some rare state, which is characterized by anomalous conditions. It is in these cases that extreme events happen.

In the last few decades, extensive international efforts have been made to understand the physics controlling the extreme events, both on meteorological and climatic time scales, because of the strong impacts they can have on the society (IPCC, 2012, 2013). In the literature, extreme events are generally defined in two ways. The former definition is statistical and considers extreme an event that falls in one of the tails of the observed frequency distribution of the variable considered. For example, take a temperature time series in a specific location and choose a relative threshold, e.g. 5% of the most unlikely events. The extreme events are those which belong to these extreme intervals, either in the upper or in the lower tail of the distribution. The latter definition, instead, involves an absolute threshold, chosen on the basis of a specific impact either on the society, the ecosystems or the human beings (e.g. body temperature above 40° C can cause severe damages to some human biological mechanisms), and whenever the variable under study falls above (or below) the threshold chosen, the event is considered to be extreme. Note that, especially for the extreme events defined from a statistical point of view, the threshold value is specific for the location and time of the year considered. For example, an extremely cold day in Russia is surely different from an extremely cold one in Egypt.

Not all meteo-climatic extreme events lead to disasters. *"Disaster signifies extreme impacts suffered when hazardous physical events interact with vulnerable social conditions to severely alter the normal functioning of a community or a society"* (IPCC, 2012). The occurrence of a disaster depends on the location and timing of the physical event, on the preparedness of the society and on how vulnerable it is to the kind of event considered. Figure 1.5 shows a schematic of how a disaster happens when different conditions occur simultaneously.

Following the definition of IPCC (2012), three main categories of extreme events are generally identified:

- atmospheric or climatic variable extremes, such as temperature, rain or wind magnitude;
- more complex weather and climate dynamical phenomena, like monsoons, ENSO variability and tropical cyclones, that lead to extremes in the variables of the above or are extreme themselves;
- extreme impacts on the natural environment that trigger, for example, flash floods, landslides, droughts, etc.

These three categories are somehow arbitrary and there are events that could fit in one or more of them. Some extreme events, then, are the result of multiple conditions happening simultaneously, which might not be extreme by themselves, or are determined

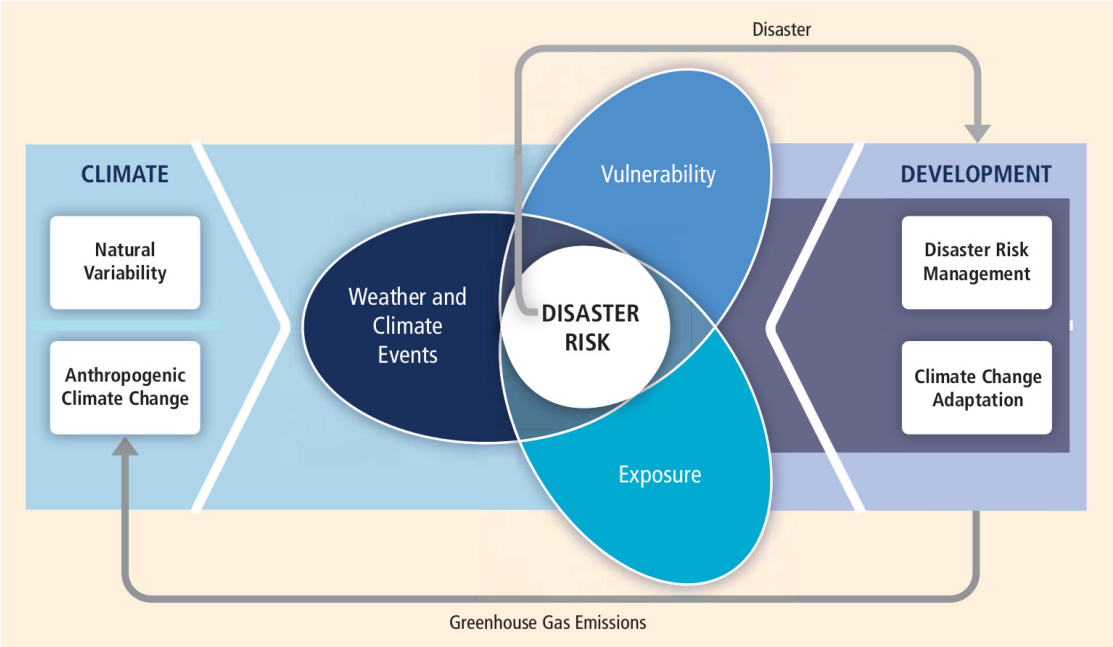

Figure 1.5: Schematic of the different conditions that have to occur simultaneously to lead to a disaster and how climate change and sustainable development are thought to interact with that. Meteo-climatic extreme events are one of the factors (IPCC, 2012).

by the anomalous persistence of normal conditions. As an example, heat waves and cold spells are generally associated with atmospheric blocking.

When looking at the causes of these extreme events, natural variability is indeed to be taken into account, but there are increasing evidences that the climate change, with its partially anthropogenic origin, is leading to modifications of the frequency, intensity, spatial extent and duration of such events, which might also lead to unprecedented extremes. Since, then, disasters are caused by meteo-climate extremes together with high exposure and vulnerability, not only is the effort made in understading the underlying physics, but also strategies of adaptation and mitigation are being developed for a wide variety of societal conditions (IPCC, 2012, 2013).

Some of the changes in the observed extremes have been linked with significant confidence to the human impacts on the climate system. Among those, there are a decrease (increase) in cold (warm) temperature extremes, an increase in exceptionally high sea level and an increase in the number of heavy rainfalls in multiple locations. In particular, it seems that over land there are more places where the number of intense rain events has increased than places where it has decreased and such global intensification of heavy precipitation seems to be due to the anthropogenic forcing (IPCC, 2012). Considering another kind of extreme event, the positive trends in the intensification and increased frequency of tropical cyclones are almost certain over the North Atlantic from

the 1970s. The likelihood of tropical cylone activity trends on longer time scales is much lower, as well as the one for small-scale severe weather events, such as thunderstorms and mesoscale convective systems (IPCC, 2013).

A key point that explains the low confidence that is often associated with the observations of extreme events and their trends is the fact that they are intrinsecally rare to observe and thus the number of available observations and data sets is particularly low. From a theoretical and modeling point of view, recent works have been able to tackle this issue by forcing the simulated climate system to remain in the vicinity of an extreme state, so that the confidence level of the modeled statistical properties is higher. In particular, this has been achieved in the framework of the large deviation theory (Touchette, 2009; Ragone et al., 2017), which, compared to the alternative approach of the generalized extreme value theory (Lucarini et al., 2016; Faranda et al., 2017), is not purely statistical but also takes into account the equations of motion of the system.

The intrinsic difficulty in detecting and attributing changes in the frequency of extreme events and, thus, in making predictions on their future occurrence can be partially offset by understanding the physical processes that favor their occurrence, which might depend on conditions that are easier to measure and to predict. One example of this method is the analysis presented in Mei et al. (2015), where the intensification of typhoons in the western tropical Pacific has been linked to the large-scale thermal structure of the upper ocean. The ocean physical properties are easier to study than the atmospheric ones as they vary on longer time scales. Following this approach, the role of the thermal upper ocean state in the development and evolution of intense precipitation events is studied in this thesis and presented in chapters 3 and 4.

1.3 Outline

The goal of this thesis is to study at meteorological time scales, O(days), the physical processes that control two kinds of atmospheric extreme events that strongly interact with the ocean. Both atmospheric processes influencing ocean dynamics and ocean properties affecting atmospherical phenomena are considered. In particular, the energy exchanges among ocean internal waves in the wake of a tropical cyclone and the role of the upper ocean thermal structure (both horizontal and vertical) in the generation of heavy-rain-producing mesoscale convective systems are studied by means of numerical integration of the appropriate primitive equations with state-of-the-art regional numerical models. Both categories of events are extreme in the statistical sense and are related to their probability of occurrence and not to an absolute impact-related threshold. It is deliberately chosen to study two different kinds of phenomena characterized by extreme meteorological conditions, the former having a focus on the oceanic response to an extreme atmospheric forcing and the latter on the atmospheric response to the oceanic state.

The relevant literature is reviewed at the beginning of each chapter and, then, the specific research question is posed. Methods, results, discussions and conclusions follow. Chapter 2 is dedicated to the study of the nonlinear interactions of oceanic internal waves

in the wake of a moving cyclone. Theoretical arguments, supported by relevant numerical simulations in an idealized setup, are used to describe such interactions. Chapters 3 and 4 are devoted to the analysis of the role of the upper ocean thermal state in the influence of the atmospheric boundary layer dynamics leading to heavy-rain-producing mesoscale convective systems (MCSs). In particular, chapter 3 studies the role of the horizontal sea surface temperature (SST) structure in the dynamics of a MCS, with a focus on how the SST patterns force dynamical features in the low-level winds on hourly time scales. Chapter 4 considers the role of the vertical thermal structure of the ocean in the generation and evolution of such heavy rainfalls through the wind-induced mixing, which enables deeper water to reach the surface and modify the SST. General conclusions are given in chapter 5.

Two

Nonlinear wave interactions in the wake of a tropical cyclone

The nonlinear dynamics leading to the generation of superinertial internal waves in the ocean, in the wake of a cyclonic storm, is investigated by means of theoretical arguments and of numerical integration of the hydrostatic Boussinesq equations in a simplified realistic open-ocean setting. The velocity fields are first decomposed into internal baroclinic modes and then the energy transfer across modes and at different frequencies is calculated analytically. The energy transfer across modes is dominated by the advection of high mode (m) waves by the second and third mode waves ($n = 2$ or 3), which are the most energetic, and this results in the excitation of the $l = m - 2$ or $m - 3$ mode wave at the double inertial frequency. The analyzed nonlinear interactions lead to a transfer of energy from near-inertial waves, directly excited by the storm, to superinertial waves, which typically propagate faster and further than their lower frequency parents and can lead to internal mixing even at large distances from the region of large air-sea momentum fluxes. Energy is found to flow from large scales to small scales, as well. Thus, the double inertial peak formation is thought to represent a small but fundamental intermediate step in the energy cascade towards dissipation.[1]

2.1 Introduction

Internal waves are ubiquitous in the ocean and show almost universal spectral features, described by the empirical spectrum developed by Garrett and Munk (1972, 1975, 1979). The physical processes responsible for the observed spectrum are still to be fully understood but the waves are forced mostly by atmospheric forcing (Rubenstein, 1994; Nilsson, 1995) and tide-topography interactions (Sjöberg and Stigebrandt, 1992) and the spectrum is believed to be the result of nonlinear interactions.

[1]For most part, the content of this chapter has been published as Meroni, A. N., M. D. Miller, E. Tziperman and C. Pasquero, 2017: Nonlinear energy transfer among ocean internal waves in the wake of a moving cyclone. *J. Phys. Oceanogr.*, **47**, 1961-1980, doi:10.1175/JPO-D-16-0232.1.

Internal waves are important among other reasons because they play a non-negligible role in ocean interior mixing, which is known to be very spatially inhomogeneous (Polzin et al., 1997; Whalen et al., 2012; Waterhouse et al., 2014), but still not yet fully understood (Ledwell et al., 1993; Munk and Wunsch, 1998; Ledwell et al., 2000; Heywood et al., 2002; Eden, 2011, 2012; Olbers and Eden, 2013; Griesel et al., 2015).

Internal waves propagate from their forcing regions into the interior of the ocean, where they can interact nonlinearly (Olbers, 1976; McComas and Bretherton, 1977; Ripa, 1981; Müller et al., 1986) and, when they become unstable, finally break. With their breaking, they contribute to the vertical diapycnal mixing of heat, salt and dissolved chemical species (Olbers, 1974, 1976; Hibiya et al., 1996) and, since they transport energy and momentum, they can induce mean flow changes (Staquet and Sommeria, 2002).

Ocean response to tropical cyclones

Among the atmospheric sources of oceanic internal waves there are both the climatological winds and the more intermittent and non uniformly distributed intense wind events, such as tropical cyclones. Estimates of the annual mean upper ocean thermal diffusivity resulting from the passage of tropical cyclones are of the order of $O(10^{-5})$ or $O(10^{-4})$ m^2 s^{-1} (Korty et al., 2008; Sriver and Huber, 2007), at least 10 times larger than the observed background tropical thermocline thermal diffusivity (Ledwell et al., 1998). This happens because momentum fluxes depend nonlinearly on wind intensity and it means that, even if intermittent and localized, tropical cyclones contribution to the upper ocean mixing is non-negligible.

Geisler (1970) showed in his linear analysis that if the hurricane speed is greater than the eigenspeed of the wave (in terms of the internal mode decomposition, as clarified in what follows), the baroclinic response of the ocean is excited (see figure 2.1). In a continuously stratified ocean, this means that the storm has a three dimensional near-inertial internal wave wake. Instead, if the hurricane is too slow, there is no wake. Tropical cyclones usually move with a speed which ranges from 1 m s^{-1} to 10 m s^{-1} and the eigenspeeds are typically smaller than 3 m s^{-1}, which means that tropical cyclones are generally effective sources of internal waves. Geisler (1970) also showed that the pressure anomaly of the tropical cyclone induces a deformation in the free surface height, but has a very small effect on the baroclinic oscillating response. In fact, by writing the equation for the baroclinic mode he explicitly showed that the forcing due to the pressure low is negligible compared to the forcing due to the wind stress. Another linear solution to the equations of motion in the ocean forced by a moving cyclone was given by Gill (1982, chap. 9), who found a resonant behavior in the energy of the vertical velocity oscillations as a function of the translation speed of the hurricane. In particular, if the residence time of the storm (the ratio of its typical length to its translation speed) is close to the local inertial period (the inverse of the Coriolis parameter), the coupling between the forcing and the inertial currents is very efficient and the tropical cyclone can transfer energy to the ocean optimally. The sensitivity of the response to the hurricane translation speed was further studied by Greatbatch (1984); Samson et al. (2009); Mei et al. (2012) with

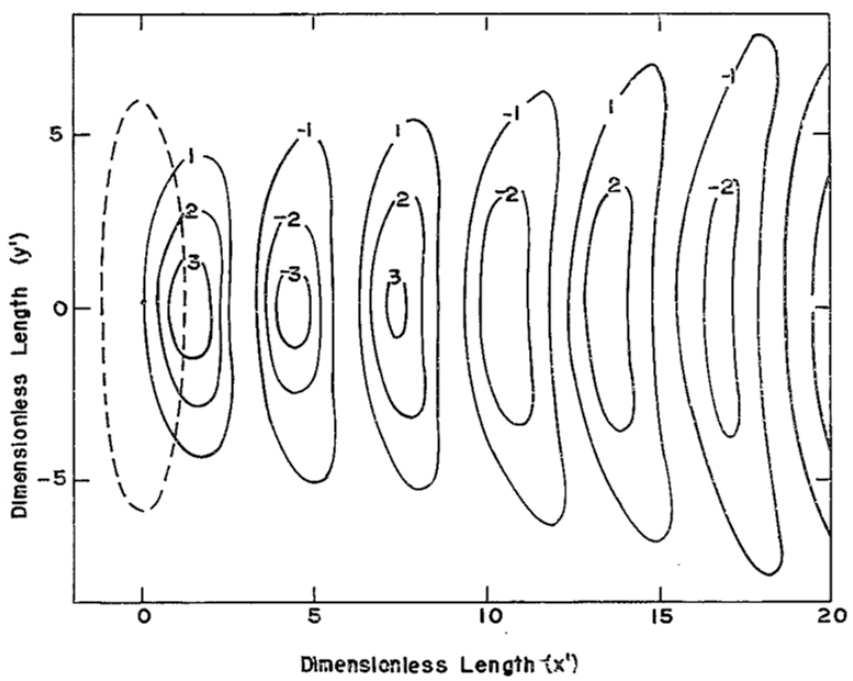

Figure 2.1: Example of analytical baroclinic steady response of the ocean to the forcing of a tropical cyclone (confined to the dashed region). The storm is moving to the left at constant speed U, five times the eigenspeed of the system. The contours are proportional to the vertical velocity at the interface of the two layer model studied by Geisler (1970).

both numerical simulations and data analysis. A detailed theoretical description of the energy transfer from a translating hurricane to the ocean was given by Nilsson (1995).

Many other works focused on the dynamical and thermodynamical response of the ocean to hurricanes (Price, 1981; Chang and Anthes, 1978; Sanford et al., 2007; D'Asaro et al., 2007; Black and Dickey, 2008) and their consequence on the global climate and meridional heat transport (Pasquero and Emanuel, 2008; Jansen and Ferrari, 2009; Jansen et al., 2010).

Superinertial waves

The focus of the analysis presented in this chapter is on the generation mechanism of superinertial waves, i.e., waves with a frequency equal to the double (or higher multiple) of the local Coriolis parameter. They were first found by Price (1983) in his numerical study of the internal wave wake but no explanation of their generation was given (see figure 2.2). The main interest in studying these superinertial waves is that they can propagate further than the near-inertial ones (Niwa and Hibiya, 1997; Zedler, 2009) and thus they can supply energy to the local internal wave field far from their generation

region. In fact, the lower limit of the range of frequency of internal waves is determined by their latitude and the upper one by the local stratification. In particular, the Coriolis parameter sets the minimum value of frequency of an internal wave that can be sustained by the system. Thus, if a wave is travelling polewards and if its frequency $\omega = f_0 + \varepsilon$ is close to the Coriolis parameter f_0 at the initial latitude ϕ_0 (a near-inertial internal wave), it may reach a latitude ϕ_1 at which the Coriolis parameter f_1 equals the frequency of the wave $f_1 = f_0 + \varepsilon$. At higher latitude ($\phi_2 > \phi_1$, with $f_2 > f_1$) the wave would have a frequency that falls out of the admissible frequency range for internal waves and thus it experiences internal reflection at the critical latitude ϕ_1 (Kroll, 1975; Munk, 1981; Garrett, 2001), unless in presence of an appropriate mean flow (Gerkema et al., 2013; Xie et al., 2016). It is clear that superinertial waves are less prone to critical latitude reflection and can therefore propagate further than near-inertial ones.

Niwa and Hibiya (1997) analyzed the superinertial wave field using an internal baroclinic mode decomposition of a uniformly stratified ocean. With such analysis, low modenumbers correspond to large vertical scales and high modenumbers to small vertical scales. They discovered that the most prominent superinertial waves appear in the lowest mode and in particular they studied with a bispectral analysis the high mode near-inertial waves that interact to give the first mode double inertial waves. They found that some couples of modes contribute to the formation of the first mode double inertial waves (modes around 7-9), while others subtract energy from them (the first few modes), as figure 2.3 shows. Thus, the energy flows in both directions and this might suggest that the formation of the double inertial peak plays a role in the energy cascade towards the small scales. The limit of their explanation is that the stratification is uniform, which means that a realistic oceanic vertical structure (mixed layer and thermocline) is not included. Their analysis is simplified due to the fact that the baroclinic modes of a uniformly stratified ocean are sinusoidal functions and therefore the modenumber is directly proportional to the vertical wavenumber. The case of non-uniform stratification is much harder to treat with the bispectral approach because there is no direct relation between a vertical wavenumber and an internal baroclinic mode.

Danioux and Klein (2008) generalized Niwa and Hibiya (1997)'s results to a non-uniform stratification profile using a perturbation approach. They considered a zonal barotropic jet $U = U(y)$ and showed that a necessary condition for nonlinear interactions that generate waves at $2f$ is that the relative vorticity of the mean flow $\zeta = -\mathrm{d}U/\mathrm{d}y$ has a non-zero Fourier component at the wavenumber that corresponds to the double inertial wave $\mathbf{k}_{2f}$. They showed that the generation mechanism is local in wavenumber space and is driven by the eddy relative vorticity field acting at the right wavenumber $\mathbf{k}_{2f}$, through a resonant mechanism due to the advective terms. They also proved that a single internal mode can interact with itself and generate superinertial motion.

Zedler (2009) used a numerical study over an ocean region with a realistic initial density profile, showing that the nonlinear interactions take place in the region of the mixed layer and the upper thermocline (first 200 m in her setup) and then are radiated to the interior through vorticity conservation as a linear mode. This seems to be in conflict with Niwa and Hibiya (1997)'s result which states that nonlinear interactions

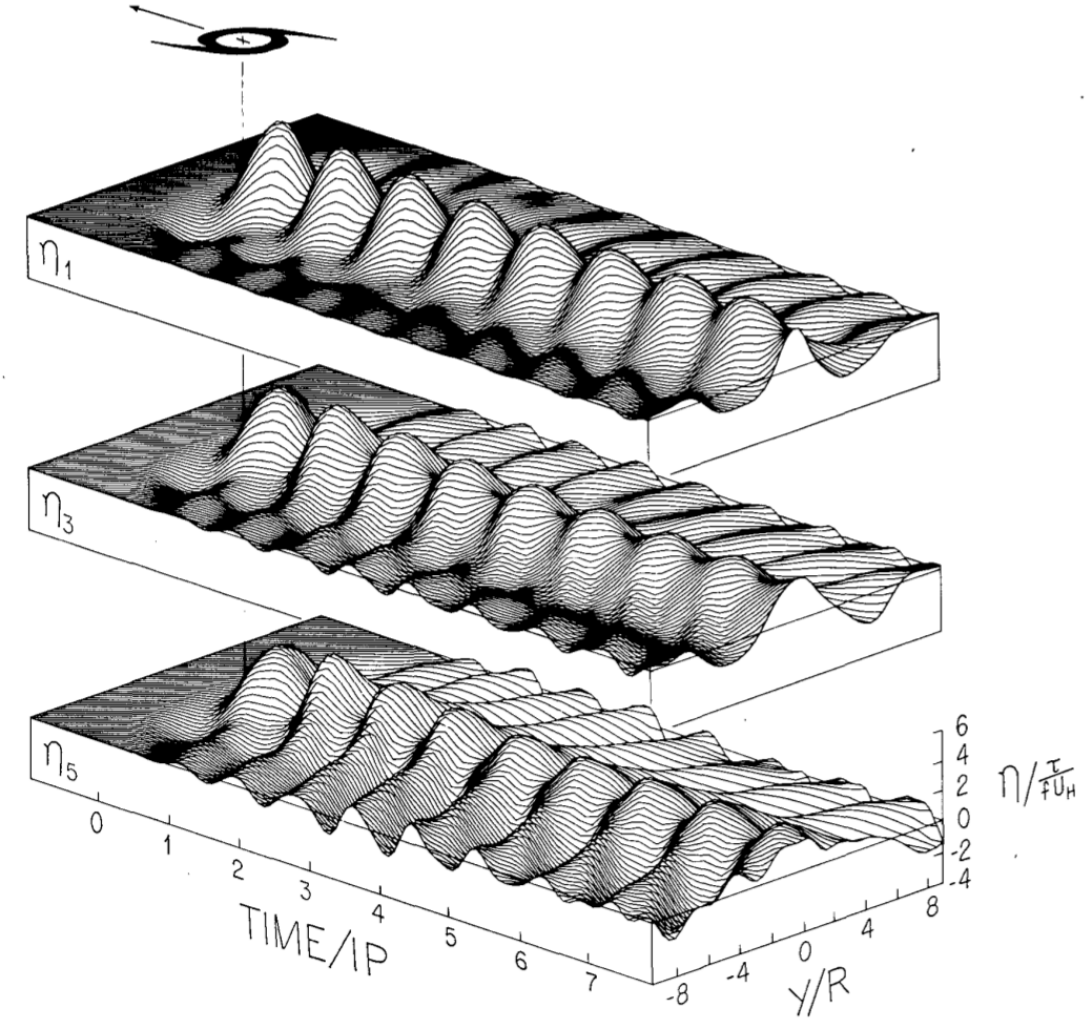

Figure 2.2: Isopycnal surfaces calculated numerically by Price (1983) in the wake of a tropical cyclone moving to the upper left. The upper surface (η_1) is at the base of the mixed layer, the middle one (η_3) is at the mid-thermocline and the lower one (η_5) is in the deep thermocline. In this last layer, double inertial oscillations can be seen starting from roughly 6 inertial periods (IP) after the passage of the storm. The other symbols are as follows: f is the Coriolis parameter, R is the radius of the storm, U_H its translation speed and τ its maximum wind stress value.

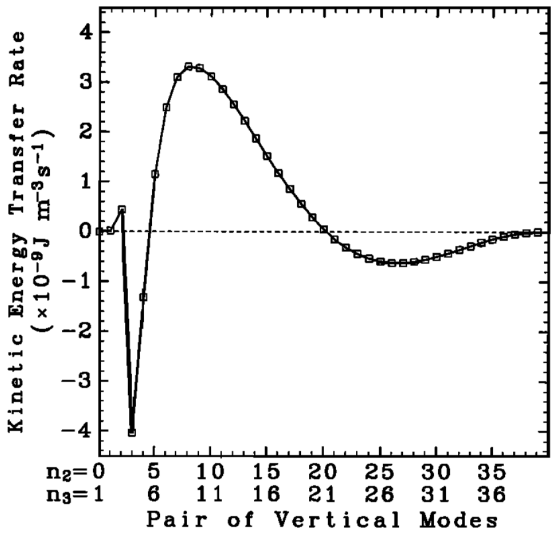

Figure 2.3: Rate of kinetic energy transfer to the first vertical mode double inertial frequency range as a function of the pair of near-inertial interacting waves vertical modes taken from Niwa and Hibiya (1997). The first few modes appear to remove double inertial energy from the first mode, while there is a positive peak at modes 7-9.

take place throughout the entire water column. But since a thorough description of the vertical structure of the stratification down to the bottom of the ocean was not included in the work, it is hard to explain whether the differences with respect to Niwa and Hibiya (1997)'s results are an effect of the different stratification. This would be the interpretation in a WKB-scaling, in which the energy scales with the stratification (Gill, 1982) and thus the energy exchanges would dominate the region of maximum $N = N(z)$, the buoyancy frequency profile, i.e. the upper ocean in the case of Zedler (2009) and the entire water column in the case of Niwa and Hibiya (1997).

In the following analysis, Niwa and Hibiya (1997)'s normal mode analysis is extended to a non-uniformly stratified ocean, to give a detailed and quantitative description of the exchange of energy between the waves excited by the tropical cyclone. The nonlinear hydrostatic Boussinesq equations are solved with two numerical simulations and an analytical theory is developed to describe the nonlinear interactions of the linear solutions, with a slightly simplified set of equations. In particular, a set of coefficients that measure the energy transfers between modes is derived analytically.

In section 2.2 the numerical model and the equations of motion used in the theoretical analysis are introduced. Section 2.3 describes how to decompose the nonlinear equations on the normal modes and in section 2.4 the analytical theory that introduces the energy transfer coefficients in the spectral domain is developed. Section 2.5 and 2.6 are devoted to the presentation of the results and the conclusions.

2.2 Numerical model and equations of motion

The problem is studied by solving numerically the fully nonlinear set of hydrostatic Boussinesq primitive equations on an f-plane. This is accomplished with two simulations run with the Region Ocean Modeling System-Adaptive Grid Refinement in Fortran (ROMS_AGRIF) in a simplified realistic setup. ROMS is a three-dimensional, free-surface, split-explicit ocean model (Penven et al., 2006; Debreu et al., 2012).

The main difference between the two simulations is the horizontal extent of the domain. In the simulation called D4000 the flat basin is 4000 km × 4000 km wide with a horizontal resolution of 20 km, while in the simulation D8000, the side of the squared basin is 8000 km and the horizontal resolution is 40 km. The numerical ocean is 5 km deep (H=5000 m) and it is discretized on a grid with 44 vertical levels, with different thicknesses, ranging from 7 m at the top to 500 m at the bottom. Turbulent vertical mixing is accomplished via the nonlocal K-Profile Parametrization, KPP (Large et al., 1994), the horizontal diffusion is set to zero and open boundary conditions on all sides allow the waves to propagate outside of the basin, reducing significantly their reflection.

The initial conditions are set analytically. The initial velocity field and the initial free surface height are zero everywhere. The potential temperature vertical profile, independent of the horizontal position, is chosen to have a climatological mixed layer depth (H_{mix}) of 50 m and then an exponential decaying profile, with a length scale $\lambda = 400$ m, namely

$$\theta(z) = \begin{cases} \theta_s & \text{for} \quad -H_{mix} < z \leq 0 \\ \theta_d + \Delta\theta \mathrm{e}^{(H_{mix}+z)/\lambda} & \text{for} \quad -H < z < -H_{mix} \end{cases} \tag{2.1}$$

where $\theta_s = 22$ °C is the surface temperature, $\theta_d = 2$ °C is the temperature at depth and $\Delta\theta = \theta_s - \theta_d$. The salinity has a constant value everywhere equal to 35 psu, so that variations in density come directly from variations in temperature through the nonlinear equation of state implemented in the model (with the SPLIT_EOS option activated). This equation is described by Shchepetkin and McWilliams (2003) and is a modified version of the one described by Jackett and McDougall (1995).

Momentum, temperature and salinity fluxes are defined as top and bottom boundary conditions. In the simulations the bottom stress, the fresh water flux and the heat flux are zero. No pressure low associated with the tropical cyclone is considered, because Geisler (1970) showed that it does not influence the internal wave wake, which is the object of this study. The only non-zero forcing is the surface wind stress, which is modeled as a radially symmetric vortex. In a reference frame moving with the storm, the wind stress is only tangential, it increases linearly with the distance for small radii and then it has a gaussian-like decay (Nilsson, 1995). In polar coordinates $\{r, \theta\}$ such a vortex with the center in the origin of the reference frame is defined as

$$\tau_s^r = 0, \quad \tau_s^\theta = \tau_o (r/R) \mathrm{e}^{(1-r^2/R^2)/2} \tag{2.2}$$

where the constant τ_o is the maximum value of the wind stress, attained at the distance R from the center (see figure 2.4). The values are chosen to be $R = 200$ km and $\tau_o = 1$

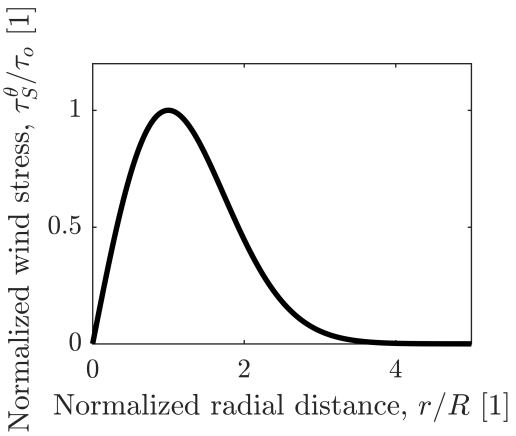

Figure 2.4: Radial profile of the wind stress considered, as defined in equation (2.2).

Pa. In a short initial phase, starting when the vortex center is still out of the domain, the amplitude of the wind stress increases from zero to the maximum value $\tau_o = 1$ Pa. Then, it moves at constant speed $U = 5$ m s^{-1} from East to West on a horizontal line in the middle of the basin, which is itself centered at 15° latitude North on an f-plane, where the inertial frequency is $f/2\pi \simeq 6 \times 10^{-5}$ s^{-1} that corresponds to a period of roughly 46 hours. The duration of the simulations is chosen so that they begin when the storm center is one diameter (400 km) out of the eastern edge of the domain and they end when the storm center is one diameter out of the western edge.

With respect to the set of equations integrated by the numerical model, a slightly simplifed one is here introduced to develop the analytical theory. Firstly, it is assumed that the equation of state is linear. This means that, since salinity is uniform and constant, the adiabatic equation for density can replace the temperature equation. Then, vertical diffusivity is set to zero and the wind stress, instead of imposing the momentum flux at the surface, acts as a body force over the entire mixed layer depth. Thus, the analytical theory is built on the following equations

$$\frac{\partial u}{\partial t} + \left(u\frac{\partial}{\partial x} + v\frac{\partial}{\partial y} + w\frac{\partial}{\partial z} \right) u - fv = -\frac{1}{\rho_o}\frac{\partial p}{\partial x} + \frac{1}{\rho_o}\frac{\tau_s^x}{H_{mix}}\sigma(z), \tag{2.3}$$

$$\frac{\partial v}{\partial t} + \left(u\frac{\partial}{\partial x} + v\frac{\partial}{\partial y} + w\frac{\partial}{\partial z} \right) v + fu = -\frac{1}{\rho_o}\frac{\partial p}{\partial y} + \frac{1}{\rho_o}\frac{\tau_s^y}{H_{mix}}\sigma(z), \tag{2.4}$$

$$\frac{\partial p}{\partial z} + \rho g = 0, \tag{2.5}$$

$$\frac{\partial u}{\partial x} + \frac{\partial v}{\partial y} + \frac{\partial w}{\partial z} = 0, \tag{2.6}$$

$$\frac{g}{\rho_o}\left[\frac{\partial \rho}{\partial t} + \left(u\frac{\partial}{\partial x} + v\frac{\partial}{\partial y} + w\frac{\partial}{\partial z} \right) \rho \right] - wN^2 = 0, \tag{2.7}$$

where the usual symbols are used: f is the Coriolis parameter; u, v and w are the velocity components; τ_s^x, τ_s^y are the Cartesian components of the surface wind stress; ρ and p are the density and the pressure anomalies with respect to the reference profiles, $\rho_o + \hat{\rho}(z)$ and $\hat{p}(z)$, which are in hydrostatic balance and with $|\rho|, |\hat{\rho}| \ll \rho_o$ and $|p| \ll \hat{p}$. The profile $\rho_o + \hat{\rho}(z)$ is defined so that its vertical derivative is equal to the adiabatic vertical derivative of the total density in its unperturbed state. This means that the density anomaly ρ plays the role of a locally referenced potential density and it is suitable for calculating the squared buoyancy frequency profile,

$$N^2 = -\frac{g}{\rho_o}\frac{\partial \rho}{\partial z}, \tag{2.8}$$

where g is the acceleration due to gravity (Shchepetkin and McWilliams, 2003). The depth of the mixed layer is denoted with H_{mix} and the step function is $\sigma(z) = 1$ if $-H_{mix} < z < 0$ and $\sigma(z) = 0$ otherwise.

At the flat bottom $z = -H$ the boundary condition is $w = 0$ and, since the baroclinic modes are found in the rigid lid approximation (Gill, 1982), at the surface $z = 0$ the condition $w = 0$ holds as well.

2.3 Internal mode decomposition

The internal modes have largely proved to be a valuable tool to describe the vertical structure of the response of the ocean to wind forcing (Pollard, 1970; Gill, 1982, 1984; Kundu and Thomson, 1985; Shay et al., 1989; Nilsson, 1995). In this section the nonlinear equations (2.3)-(2.7) are projected on the internal modes.

Following the notation used by Nilsson (1995), the internal baroclinic modes $h_n(z)$ and the correspondent eigenspeed c_n, with $n \in \mathbb{N}, n \geq 1$, are the solutions of the Sturm-Liouville problem

$$\frac{h_{nzz}}{N^2} + \frac{h_n}{c_n^2} = 0 \quad \text{with} \quad h_n(0) = h_n(-H) = 0, \tag{2.9}$$

where the subscript $_z$ denotes derivation with respect to the vertical direction and N is the buoyancy frequency profile considered.

Since the normal modes are defined up to a multiplicative constant, a normalization condition has to be imposed and a common choice is $h_{nz}(0) = 1$. The buoyancy frequency corresponding to the unperturbed anomaly density profile obtained from the numerical simulations (both shown in figure 2.5) is used to numerically calculate the internal baroclinic modes of the problem, by solving equation (2.9). The first four modes are shown in figure 2.6 together with their vertical derivatives. The modes calculated in this way are used both in the analysis of the simulations and in the analytical part of this work.

The complete theory of normal modes includes also the barotropic one. However, at least since Geisler (1970) it is known that there is no barotropic contribution to the wave

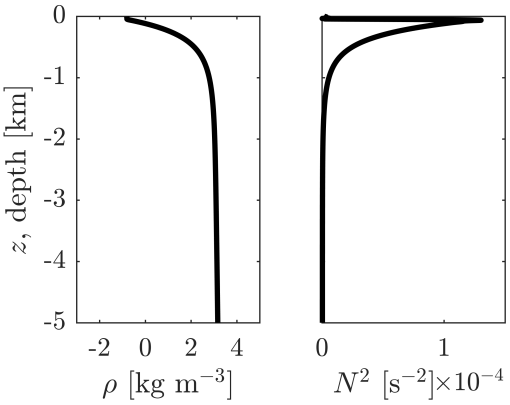

Figure 2.5: The left panel shows the unperturbed density anomaly vertical profile ρ and the right one shows the squared buoyancy frequency N^2, as defined in equation (2.8).

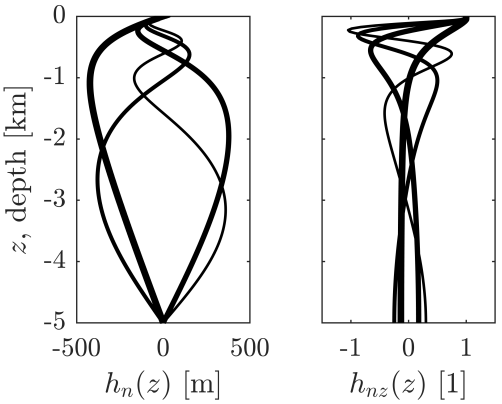

Figure 2.6: First four baroclinic modes $h_n(z)$ and their vertical derivatives $h_{nz}(z)$ for $n = 1, ..., 4$. The thickness of the lines decreases with increasing modenumber.

wake. Moreover, as in the present study direct calculations confirmed that the role of the barotropic mode is negligible (not shown), only the baroclinic modes are considered.

The dynamical variables can thus be projected on the internal modes as

$$w = \sum_{l=1}^{+\infty} w_l h_l, \tag{2.10}$$

$$[u, v, p/\rho_o, \sigma] = \sum_{l=1}^{+\infty} [u_l, v_l, p_l, \sigma_l] h_{lz}, \tag{2.11}$$

$$-\rho/\rho_o = \sum_{l=1}^{+\infty} \eta_l h_{lzz}, \tag{2.12}$$

where h_l and their vertical derivatives h_{lz} and h_{lzz} contain all the dependence on the depth z and the expansion coefficients are function of (x, y, t). By exploiting the orthogonality of the internal modes (Gill, 1982, chap. 6), the expansion coefficients can be found as

$$w_l = \frac{\int_{-H}^{0} \mathrm{d}z\, N^2 h_l w}{\int_{-H}^{0} \mathrm{d}z\, N^2 h_l^2},$$

$$[u_l, v_l, p_l, \sigma_l] = \frac{\int_{-H}^{0} \mathrm{d}z\, h_{lz}\, [u, v, p/\rho_o, \sigma]}{\int_{-H}^{0} \mathrm{d}z\, h_{lz}^2},$$

$$\eta_l = p_l/g,$$

with the last equality given by the hydrostatic equation. These integrals are calculated directly with the outputs of the simulations to find the projections of the fully nonlinear solutions.

Using the decomposition introduced above, equations (2.10)-(2.12), it is well known that the linearized governing equations for a stratified ocean can be replaced by an infinite set of linear shallow water equations (Gill, 1982, chap. 6). In particular, η_l plays the role of the free surface height and with the definitions of equivalent depth $H_l = c_l^2/g$ and equivalent forcing depth $H_l^F = H_{mix}/\sigma_l$, the dynamics is described by the linear shallow water equations in the variables u_l, v_l, η_l. This linear problem was solved by Gill (1982, chap. 9), who showed that the energy of the waves is concentrated in a peak around the nondimensional frequency

$$\frac{\omega_{Gl}}{f} = \frac{1}{\sqrt{1 - c_l^2/U^2}}, \tag{2.13}$$

where c_l is the eigenspeed of the mode considered and U is the storm translation speed. Then, Shay et al. (1989) solved the problem by finding its Green's function, following Geisler (1970)'s approach. Finally, Nilsson (1995) used the linear solution written in the spectral space to calculate analytically the energy flux from a travelling tropical cyclone to the oceanic internal wave field.

However, in this work the focus is on nonlinearities and it is shown that they break the analytical equivalence between a stratified ocean and the infinite set of shallow water systems. Equation (2.6) projected on the l-th internal mode gives

$$w_l = -\left(\frac{\partial u_l}{\partial x} + \frac{\partial v_l}{\partial y}\right). \tag{2.14}$$

The advective term can be brought to the right hand side of equation (2.3) and then projected on the l-th mode as follows

$$\begin{aligned} &-\left(u\frac{\partial}{\partial x} + v\frac{\partial}{\partial y} + w\frac{\partial}{\partial z}\right)u = \\ &= \sum_{n=1}^{+\infty}\left[-h_{nz}\left(u_n\frac{\partial}{\partial x} + v_n\frac{\partial}{\partial y}\right) + h_n\left(\frac{\partial u_n}{\partial x} + \frac{\partial v_n}{\partial y}\right)\frac{\partial}{\partial z}\right]\sum_{m=1}^{+\infty}(h_{mz}u_m) = \\ &= \sum_{n,m=1}^{+\infty}\left[-h_{nz}h_{mz}\left(u_n\frac{\partial}{\partial x} + v_n\frac{\partial}{\partial y}\right) + h_n h_{mzz}\left(\frac{\partial u_n}{\partial x} + \frac{\partial v_n}{\partial y}\right)\right]u_m. \end{aligned} \tag{2.15}$$

Now the products $-h_{nz}h_{mz}$ and $h_n h_{mzz}$ can be decomposed on the basis of the modes for the horizontal velocity $\{h_{lz}\}_{l\in\mathbb{N}}$, so that

$$-h_{nz}h_{mz} = \sum_{l=0}^{+\infty}\alpha_{nml}h_{lz} \quad \text{and} \quad h_n h_{mzz} = \sum_{l=0}^{+\infty}\beta_{nml}h_{lz}$$

with the expansion coefficients given explicitly by

$$\alpha_{nml} = -\frac{\int_{-H}^{0}\mathrm{d}z\, h_{nz}h_{mz}h_{lz}}{\int_{-H}^{0}\mathrm{d}z\, h_{lz}^2}, \tag{2.16}$$

$$\beta_{nml} = \frac{\int_{-H}^{0}\mathrm{d}z\, h_n h_{mzz}h_{lz}}{\int_{-H}^{0}\mathrm{d}z\, h_{lz}^2}. \tag{2.17}$$

The same coefficients appear while projecting on the modes the v velocity component equation, (2.4), so that the advective terms in the momentum equations are

$$-\left(u\frac{\partial}{\partial x} + v\frac{\partial}{\partial y} + w\frac{\partial}{\partial z}\right)u = \sum_{n,m,l=1}^{+\infty}\mathcal{U}_{nml}h_{lz} \tag{2.18}$$

$$-\left(u\frac{\partial}{\partial x} + v\frac{\partial}{\partial y} + w\frac{\partial}{\partial z}\right)v = \sum_{n,m,l=1}^{+\infty}\mathcal{V}_{nml}h_{lz} \tag{2.19}$$

with

$$\mathcal{U}_{nml} = \left[\alpha_{nml}\left(u_n\frac{\partial}{\partial x} + v_n\frac{\partial}{\partial y}\right) + \beta_{nml}\left(\frac{\partial u_n}{\partial x} + \frac{\partial v_n}{\partial y}\right)\right]u_m, \tag{2.20}$$

$$\mathcal{V}_{nml} = \left[\alpha_{nml}\left(u_n\frac{\partial}{\partial x} + v_n\frac{\partial}{\partial y}\right) + \beta_{nml}\left(\frac{\partial u_n}{\partial x} + \frac{\partial v_n}{\partial y}\right)\right]v_m. \tag{2.21}$$

Considering now the density equation, (2.7), divided by the squared buoyancy frequency N^2, the coefficients

$$\lambda_{nml} = -\frac{c_l}{c_m}\frac{\int_{-H}^{0} \mathrm{d}z\, N^2 h_{nz} h_m h_l}{\int_{-H}^{0} \mathrm{d}z\, N^2 h_l^2}, \tag{2.22}$$

$$\mu_{nml} = -c_l c_m \frac{\int_{-H}^{0} \mathrm{d}z\, h_n h_{mzzz} h_l}{\int_{-H}^{0} \mathrm{d}z\, N^2 h_l^2}, \tag{2.23}$$

are defined, so that one can write

$$-\frac{g}{\rho_o N^2}\left(u\frac{\partial}{\partial x} + v\frac{\partial}{\partial y} + w\frac{\partial}{\partial z}\right)\rho = \sum_{n,m,l=1}^{+\infty} \mathcal{R}_{nml}\frac{h_l}{c_l} \tag{2.24}$$

with

$$\mathcal{R}_{nml} = \left[\lambda_{nml}\left(u_n\frac{\partial}{\partial x} + v_n\frac{\partial}{\partial y}\right) + \mu_{nml}\left(\frac{\partial u_n}{\partial x} + \frac{\partial v_n}{\partial y}\right)\right]\frac{g\eta_m}{c_m}. \tag{2.25}$$

The $\alpha_{nml}, \beta_{nml}, \lambda_{nml}, \mu_{nml}$ coefficients are calculated directly using their integral definitions introduced in equations (2.16), (2.17), (2.22) and (2.23). They represent the geometrical equivalent of the well-known triangle condition for the vertical wavenumber

$$|k_z' \pm k_z''| = k_z''', \tag{2.26}$$

which is one of the necessary condition for a triad interaction to be resonant. A triad is resonant, i.e. it implies efficient energy exchange among the waves involved, when the conditions $\mathbf{k}' \pm \mathbf{k}'' = \mathbf{k}'''$ and $\omega' \pm \omega'' = \omega'''$ are satisfied (Phillips, 1966; Thorpe, 2005; Olbers et al., 2012).

Let us now consider for a moment the simpler case of constant stratification, to gain a better understanding of the meaning of the coefficients α_{nml}, β_{nml}, λ_{nml} and μ_{nml} introduced above. The solutions of the Sturm-Liouville problem (2.9) when $N = N_o$ are

$$h_n(z) = \frac{H}{n\pi}\sin\left(\frac{n\pi}{H}z\right),$$

$$h_{nz}(z) = \cos\left(\frac{n\pi}{H}z\right),$$

which means that the vertical wavenumber is directly proportional to the modenumber. The eigenspeeds are given by $c_n = HN_o/n\pi$, which means that $c_n \sim n^{-1}$. Then, for $n, m, l \geq 1$, the definitions (2.16), (2.17), (2.22) and (2.23) give analytically

$$\alpha_{nml} = -\frac{1}{2\pi}(\delta_{n+m,l} + \delta_{n-m,l} + \delta_{-n+m,l}), \tag{2.27}$$

$$\beta_{nml} = \frac{1}{2\pi}\frac{m}{n}(\delta_{n+m,l} - \delta_{n-m,l} - \delta_{-n+m,l}), \tag{2.28}$$

$$\lambda_{nml} = \frac{1}{2\pi}(-\delta_{n+m,l} + \delta_{n-m,l} - \delta_{-n+m,l}), \tag{2.29}$$

$$\mu_{nml} = \frac{1}{2\pi}\frac{m}{n}(\delta_{n+m,l} + \delta_{n-m,l} - \delta_{-n+m,l}), \tag{2.30}$$

where the Kronecher delta appears and it imposes that the nonzero coefficients are only on the lines $n = m \pm l$ and $n = -m + l$. These relations, since the vertical wavenumber is directly proportional to the modenumber, simply represent the triangle condition for the vertical wavenumber, equation (2.26). Thus, the α_{nml}, β_{nml}, λ_{nml} and μ_{nml} coefficients can be interpreted as the geometrical equivalent in the modenumber space of the triangle condition (2.26).

Back to the exponential-like stratification under study (see figure 2.5), by computing the above coefficients (not shown), it is found that the effect of the variation of N with depth is to allow resonant interactions also out of the lines $|n \pm m| = l$ (Pomphrey et al., 1980), which is consistent with the fact that in the case of depth-varying stratification the local wavenumber of mode l varies with depth as $N(z)/c_l$ and thus there is no one-to-one correspondence between vertical wavenumbers and modenumbers. This, in turns, implies that the condition (2.26) can be respected locally even if $|n \pm m| \neq l$.

Another interesting feature that characterizes the geometrical coefficients of the above is that only the α_{nml} ones are symmetrical under the exchange of the indices n and m, while all the others are not. This is part of the reason why also the $\mathcal{U}_{nml}$, $\mathcal{V}_{nml}$ and $\mathcal{R}_{nml}$ terms introduced above are not symmetrical under the n, m exchange and in the entire following discussion, thus, one should keep in mind the different roles played by the advecting (n) and the advected wave (m).

By introducing the variable $r_l = g\eta_l/c_l$, the set of governing equations (2.3)-(2.7) can be projected on the l-th internal mode as

$$\frac{\partial u_l}{\partial t} - f v_l + c_l \frac{\partial r_l}{\partial x} = \tau_l^x + \sum_{n,m}^{+\infty} \mathcal{U}_{nml} \tag{2.31}$$

$$\frac{\partial v_l}{\partial t} + f u_l + c_l \frac{\partial r_l}{\partial y} = \tau_l^y + \sum_{n,m}^{+\infty} \mathcal{V}_{nml} \tag{2.32}$$

$$\frac{\partial r_l}{\partial t} + c_l \left(\frac{\partial u_l}{\partial x} + \frac{\partial v_l}{\partial y} \right) = \sum_{n,m}^{+\infty} \mathcal{R}_{nml} \tag{2.33}$$

together with the diagnostic equations $p_l = c_l r_l$ and $w_l = -(\partial u_l/\partial x + \partial v_l/\partial y)$.

It is known that the response of the ocean is steady in the frame of reference of the storm (Price, 1981; Gill, 1982) and thus, introducing the coordinate $\xi = x + Ut$, for a storm moving in the negative x direction, the derivatives change according to

$$\frac{\partial}{\partial x} = \frac{\partial \xi}{\partial x}\frac{\partial}{\partial \xi} = \frac{\partial}{\partial \xi} \quad \text{and} \quad \frac{\partial}{\partial t} = \frac{\partial \xi}{\partial t}\frac{\partial}{\partial \xi} = U\frac{\partial}{\partial \xi}.$$

The set of equations (2.31)-(2.33) becomes

$$U\frac{\partial u_l}{\partial \xi} - f v_l + c_l \frac{\partial r_l}{\partial \xi} = \tau_l^x + \sum_{n,m}^{+\infty} \mathcal{U}_{nml} \tag{2.34}$$

$$U\frac{\partial v_l}{\partial \xi} + f u_l + c_l \frac{\partial r_l}{\partial y} = \tau_l^y + \sum_{n,m}^{+\infty} \mathcal{V}_{nml} \tag{2.35}$$

$$U\frac{\partial r_l}{\partial \xi} + c_l \left(\frac{\partial u_l}{\partial \xi} + \frac{\partial v_l}{\partial y} \right) = \sum_{n,m}^{+\infty} \mathcal{R}_{nml} \tag{2.36}$$

with the appropriate replacements in the $\mathcal{U}_{nml}$, $\mathcal{V}_{nml}$ and $\mathcal{R}_{nml}$ terms as well.

While l varies from one to infinity, a small finite number of modes explains the majority of the total energy transferred to the ocean from the passing storm. To compare the relative importance of a single mode, the total energy of the inital set of equations, (2.3) - (2.7), is integrated vertically from the bottom to the top and decomposed as

$$\int_{-H}^{0} \mathrm{d}z \, \frac{1}{2} \left(u^2 + v^2 + \frac{g^2 \rho^2}{N^2 \rho_o^2} \right) = \sum_{l=1}^{+\infty} \frac{1}{2} \left(u_l^2 + v_l^2 + r_l^2 \right) ||h_{lz}||^2,$$

which applies because of the orthogonality of the modes. The squared norm $||h_{lz}||^2$ arises naturally in the solution of the Sturm-Liouvile problem (2.9) and it is defined as

$$||h_{lz}||^2 = \int_{-H}^{0} \mathrm{d}z \, h_{lz}^2. \tag{2.37}$$

The fields u, v, ρ are the ones obtained from the numerical simulations and they are steady in the frame of reference of the storm, thus they depend on (ξ, y, z) only. By introducing the 2D Fourier transform with wavenumbers k_x and k_y associated to the dimensions ξ and y respectively, the spectral energy density for each mode can be defined. In particular, in the spectral domain, the steadiness condition for a storm moving in the negative x direction is

$$\omega = -k_x U, \tag{2.38}$$

which is a direct link between the frequency of the wave and the along-track wavenumber.

Since the Fourier transform (denoted with a hat $\hat{}$) is a linear operator, then, also the spectral fields $\hat{u}$, $\hat{v}$ and $\hat{\rho}/\rho_o$ can be expanded in the usual way

$$[\hat{u}, \hat{v}] = \sum_{l=1}^{+\infty} [\hat{u}_l, \hat{v}_l] h_{lz}, \quad \hat{\rho}/\rho_o = \sum_{l=1}^{+\infty} \hat{\eta}_l h_{lzz}$$

which leads to a similar decomposition on the modes for the power spectrum

$$\begin{aligned} \int_{-H}^{0} \mathrm{d}z \, \frac{1}{2} \left(|\hat{u}|^2 + |\hat{v}|^2 + \frac{g^2 |\hat{\rho}|^2}{N^2 \rho_o^2} \right) &= \sum_{l=1}^{+\infty} \frac{1}{2} \left(|\hat{u}_l|^2 + |\hat{v}_l|^2 + |\hat{r}_l|^2 \right) ||h_{lz}||^2 \\ &= \sum_{l=1}^{+\infty} \hat{E}_l ||h_{lz}||^2. \end{aligned} \tag{2.39}$$

The spectral energy density for the l-th mode, $\hat{E}_l(k_x, k_y) = (|\hat{u}_l|^2 + |\hat{v}_l|^2 + |\hat{r}_l|^2)/2$, is the spectral correspondent of the energy associated to the linear set of equations (2.34)

- (2.36). The above expression shows how energy is partitioned both in horizontal wavenumbers and in modenumbers. By denoting with a tilde the spectral variables integrated along the across-track wavenumber, namely

$$\tilde{E}_l(k_x) = \int_{-\infty}^{+\infty} \mathrm{d}k_y \, \hat{E}_l(k_x, k_y),$$

one can introduce the functions $\tilde{E}_l||h_{lz}||^2$, shown for $l = 1, 2, 3$ in the left panel of figure 2.7. To study the stationary wake in the frame of reference of the storm starting from the numerical simulations, the projections of the wake on the internal modes are averaged by superimposing the center of the cyclone in the origin of the new frame of refence (ξ, y) at any given time. This averages out the transient response, that is not stationary in the frame of reference of the storm. A simple 2D Fourier transform is then applied to the steady wake. The near-inertial peak of the l-th mode is around the Geisler wavenumber, which corresponds to the blueshifted frequency of equation (2.13) through the steadiness condition (2.38). From figure 2.7, it is clear that the most prominent blueshift appears in the first mode, as described by Gill (1982, chap.9) in his linear theory.

The integral of the power spectrum around the near-inertial peak of the other modes ($l \geq 2$) monotonically decreases with the modenumber. This is equivalent to the near-inertial energy

$$\mathrm{NIE}(l) = \int_{I(f/U)} \mathrm{d}k_x \, \tilde{E}_l||h_{lz}||^2 \tag{2.40}$$

decreasing monotonically except for the first mode, as shown in the right panel of figure 2.7. On the other hand, for the energy around the double inertial peak,

$$\mathrm{DIE}(l) = \int_{I(2f/U)} \mathrm{d}k_x \, \tilde{E}_l||h_{lz}||^2 \tag{2.41}$$

the first mode is the most energetic. The intervals of integration are chosen to be $I(f/U) = \{k_x \in \mathbb{R} : 0.8f/U < k_x < 1.6f/U\}$ and $I(2f/U) = \{k_x \in \mathbb{R} : 1.8f/U < k_x < 2.2f/U\}$ and they are shown as horizontal bars in the left panel of figure 2.7. Results are not sensitive to small changes in the choice of the intervals of integration.

The important point to emphasize is that, for NIE(l), the second mode dominates, tightly followed by the third mode, while for DIE(l) it is the first one that has most of the energy. Therefore, due to the fast decrease of the DIE(l), the analysis is limited to consideration of the first three, $l = 1, 2, 3$.

2.4 Analytical spectral decomposition

By writing down the nonlinear projected equations in the spectral domain, it is possible to quantify analytically the relative contribution of the linear forcing and the nonlinear advection terms to the energy around the double inertial frequency of the first three modes.

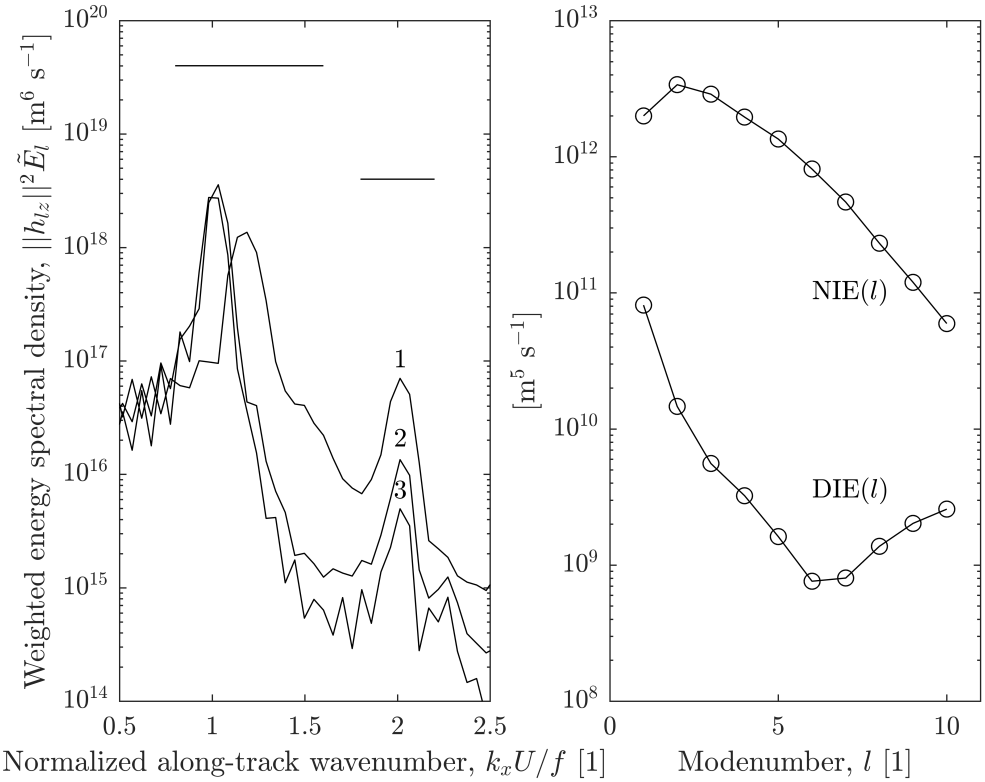

Figure 2.7: In the left panel, the first three weighted power spectra, $||h_{lz}||^2\tilde{E}_l(k_x)$ with $l = 1, 2, 3$, obtained from the simulation D8000 are shown. The tilde is used to denote spectral variables integrated along the across-track wavenumber and the squared norm of the mode is the weight needed to correctly compare the contribution of each mode. The horizontal bars show the intervals of integration used to define the near-inertial energy, NIE(l) of equation (2.40), and the double inertial energy, DIE(l) of equation (2.41), shown in the right panel as a function of the modenumber. It is important to notice that the second and the third mode are the most energetic in terms of NIE(l), but it is the first one that contains most of the DIE(l).

2D energy spectral density

In the Fourier space, the equations (2.34) - (2.36) become

$$ik_xU\hat{u}_l - f\hat{v}_l + ik_xc_l\hat{r}_l = \hat{\tau}_l^x + \sum_{n,m}^{+\infty}\hat{\mathcal{U}}_{nml} \tag{2.42}$$

$$ik_xU\hat{v}_l + f\hat{u}_l + ik_yc_l\hat{r}_l = \hat{\tau}_l^y + \sum_{n,m}^{+\infty}\hat{\mathcal{V}}_{nml} \tag{2.43}$$

$$ik_xU\hat{r}_l + c_l\left(ik_x\hat{u}_l + ik_y\hat{v}_l\right) = \sum_{n,m}^{+\infty}\hat{\mathcal{R}}_{nml} \tag{2.44}$$

which can be rewritten in matricial form as $\mathbf{A}\hat{\mathbf{x}} = \hat{\mathbf{b}}$ with

$$\mathbf{A} = \begin{bmatrix} ik_xU & -f & ik_xc_l \\ f & ik_xU & ik_yc_l \\ ik_xc_l & ik_yc_l & ik_xU \end{bmatrix}, \hat{\mathbf{x}} = \begin{pmatrix} \hat{u}_l \\ \hat{v}_l \\ \hat{r}_l \end{pmatrix},$$

$$\hat{\mathbf{b}} = \hat{\mathbf{b}}_o + \sum_{n,m}^{+\infty}\begin{pmatrix} \hat{\mathcal{U}}_{nml} \\ \hat{\mathcal{V}}_{nml} \\ \hat{\mathcal{R}}_{nml} \end{pmatrix}, \hat{\mathbf{b}}_o = \begin{pmatrix} \hat{\tau}_l^x \\ \hat{\tau}_l^y \\ 0 \end{pmatrix}. \tag{2.45}$$

With this notation, it is straightforward to calculate the spectral energy density for the l-th mode as

$$\hat{E}_l = \frac{1}{2}(|\hat{u}_l|^2 + |\hat{v}_l|^2 + |\hat{r}_l|^2) = \frac{1}{2}[\hat{\mathbf{b}}^{*T}(\mathbf{A}\mathbf{A}^{*T})^{-1}\hat{\mathbf{b}}], \tag{2.46}$$

where the star * denotes the complex conjugate and the superscript ^{T} denotes the transpose. With the definition of the matrix $\mathbf{C} = (\mathbf{A}\mathbf{A}^{*T})^{-1}$, which also satisfies $\mathbf{C} = -(\mathbf{A}\mathbf{A})^{-1}$, since $\mathbf{A}$ is anti-hermitian, one finds

$$\hat{E}_l = \frac{1}{2}(C_{11}|\hat{b}_1|^2 + C_{22}|\hat{b}_2|^2 + C_{33}|\hat{b}_3|^2) + \mathrm{Re}\{C_{12}\hat{b}_1^*\hat{b}_2 + C_{13}\hat{b}_1^*\hat{b}_3 + C_{23}\hat{b}_2^*\hat{b}_3\}. \tag{2.47}$$

The coefficients C_{ij} are polynomials in the wavenumber components k_x, k_y and they can be obtained by inverting $-\mathbf{A}\mathbf{A}$. Once the determinant of $-\mathbf{A}\mathbf{A}$ is known thanks to the Binet theorem,

$$\det(-\mathbf{A}\mathbf{A}) = \det(-\mathbb{I})[\det(\mathbf{A})]^2 = k_x^2U^2[k_x^2(U^2 - c_l^2) - k_y^2c_l^2 - f^2]^2, \tag{2.48}$$

then, with the cofactors method, the entries of the inverse matrix are

$$C_{11}(k_x,k_y) = \frac{1}{k_x^2U^2} + \frac{f^2+c_l^2k_x^2}{k_x^2U^2}W + 2(f^2+c_l^2k_x^2)W^2 \tag{2.49}$$

$$C_{22}(k_x,k_y) = \frac{1}{k_x^2U^2} + \frac{f^2+c_l^2k_y^2}{k_x^2U^2}W + 2(f^2+c_l^2k_y^2)W^2 \tag{2.50}$$

$$C_{33}(k_x,k_y) = \frac{1}{k_x^2U^2} + \frac{c_l^2(k_x^2+k_y^2)}{k_x^2U^2}W + 2c_l^2(k_x^2+k_y^2)W^2 \tag{2.51}$$

$$C_{12}(k_x,k_y) = \frac{k_yc_l^2}{k_xU^2}W + 2(k_xk_yc_l^2 - ifk_xU)W^2 \tag{2.52}$$

$$C_{13}(k_x,k_y) = \frac{ifk_yc_l}{k_x^2U^2}W + 2(-k_x^2Uc_l + ifk_yc_l)W^2 \tag{2.53}$$

$$C_{23}(k_x,k_y) = -\frac{ifc_l}{k_xU^2}W - 2(k_xk_yUc_l + ifk_xc_l)W^2 \tag{2.54}$$

with

$$W(k_x,k_y) = \frac{1}{U^2k_x^2 - f^2 - c_l^2(k_x^2+k_y^2)} \in \mathbb{R}. \tag{2.55}$$

This function is important because, as Nilsson (1995) explains well, the locus of wavenumbers defined by the zero of its denominator selects the waves that can move steadily with the storm. This, in the present analysis, means that only waves whose wavenumber (k_x, k_y) belongs to the hyperbola

$$U^2k_x^2 = f^2 + c_l^2(k_x^2+k_y^2) \tag{2.56}$$

are steady in the frame of reference of the storm and, thus, are considered in the energy exchanges. As a consequence, this excludes that the second harmonic peak is phase-locked to the fundamental peak, which is the one centered on the Geisler wavenumber

$$\mathbf{k}_{Gl} = \left(\frac{f}{\sqrt{U^2-c_l^2}}, 0\right). \tag{2.57}$$

In fact, the wavenumber of a second harmonic phase-locked wave is the double of the Geisler wavenumber, $\mathbf{k}_{2,p.l.} = 2\mathbf{k}_{Gl}$, which one can easily verify that does not belong to the hyperbola of the above.

Going back the spectral energy density equation, by replacing the forcing vector $\hat{\mathbf{b}}$ of (2.45) in (2.47), $\hat{E}_l(k_x,k_y)$ becomes

$$\hat{E}_l(k_x,k_y) = \Psi_l^0 + \sum_{n,m=1}^{+\infty}\Psi_{nml}^1 + \sum_{q,s,n,m=1}^{+\infty}\Psi_{qsnml}^2, \tag{2.58}$$

where

$$\Psi_l^0(k_x,k_y) = \frac{1}{2}\left(C_{11}|\hat{\tau}_l^x|^2 + C_{22}|\hat{\tau}_l^y|^2\right) + \mathrm{Re}\{C_{12}(\hat{\tau}_l^x)^*\hat{\tau}_l^y\} \tag{2.59}$$

contains no advection term,

$$\begin{aligned}\Psi^1_{nml}(k_x,k_y) =& \mathrm{Re}\left\{[C_{11}(\hat{\tau}^x_l)^* + C^*_{12}(\hat{\tau}^y_l)^*]\hat{\mathcal{U}}_{nml}\right\} + \\ &+ \mathrm{Re}\left\{[C_{12}(\hat{\tau}^x_l)^* + C_{22}(\hat{\tau}^y_l)^*]\hat{\mathcal{V}}_{nml}\right\} + \\ &+ \mathrm{Re}\left\{\left[C_{13}(\hat{\tau}^x_l)^* + C_{23}(\hat{\tau}^y_l)^*\right]\hat{\mathcal{R}}_{nml}\right\} \end{aligned} \tag{2.60}$$

contains advection terms to the first power and

$$\begin{aligned}\Psi^2_{qsnml}(k_x,k_y) = \mathrm{Re}\left\{C_{12}\hat{\mathcal{U}}^*_{qsl}\hat{\mathcal{V}}_{nml} + C_{13}\hat{\mathcal{U}}^*_{qsl}\hat{\mathcal{R}}_{nml} + C_{23}\hat{\mathcal{V}}^*_{qsl}\hat{\mathcal{R}}_{nml}\right\} + \\ +\frac{1}{2}\left(C_{11}\mathrm{Re}\{\hat{\mathcal{U}}^*_{qsl}\hat{\mathcal{U}}_{nml}\} + C_{22}\mathrm{Re}\{\hat{\mathcal{V}}^*_{qsl}\hat{\mathcal{V}}_{nml}\} + C_{33}\mathrm{Re}\{\hat{\mathcal{R}}^*_{qsl}\hat{\mathcal{R}}_{nml}\}\right)\end{aligned} \tag{2.61}$$

contains products of two advection terms. It is easy to see, now, that if all the advection terms were zero, i.e. $\hat{\mathbf{b}} = \hat{\mathbf{b}}_o$ in equation (2.45), $\Psi^1_{nml} = 0\,\forall\, n,m,l \in \mathbb{N}$ and $\Psi^2_{qsnml} = 0\,\forall\, q,s,n,m,l \in \mathbb{N}$, so that $\hat{E}_l(k_x,k_y) = \Psi^0_l$ as in Nilsson (1995)'s solution.

Along-track energy spectral density

In order to focus on the energy exchanges involving the double inertial frequency range, one can make use of the steadiness condition (2.38), that relates directly the along-track wavenumber to the frequency. Denoting with a tilde the functions integrated along the k_y axis, for example

$$\tilde{\Psi}^0_l(k_x) = \int_{-\infty}^{+\infty} \mathrm{d}k_y\, \Psi^0_l(k_x,k_y),$$

one obtains the power spectrum density and its components as a function of the along-track wavenumber only, namely

$$\tilde{E}_l(k_x) = \tilde{\Psi}^0_l + \sum_{n,m=1}^{+\infty} \tilde{\Psi}^1_{nml} + \sum_{q,s,n,m=1}^{+\infty} \tilde{\Psi}^2_{qsnml}. \tag{2.62}$$

But the zeros in the denominator of the function $W(k_x,k_y)$ of equation (2.55) make it necessary to regularize the above k_y integrals by taking their Cauchy principal value, denoted with a P. Using $f(s)$ as a general form of the function of equations (2.59) -(2.61) with s, the variable of integration, playing the role of k_y, the general form of such integrals is

$$P\int_{-\infty}^{\infty} \mathrm{d}s\, f(s)\frac{s^\gamma}{D^\nu} \quad \text{with} \quad D = (s-\chi)(s+\chi)(s-\chi^*)(s+\chi^*), \tag{2.63}$$

where γ, ν are positive integer numbers, $\chi \in \mathbb{C}$ is a first order pole in correspondence of the singularities of the W function and $f(s)$ is a smooth regular function that decays fast enough as s increases, so that the Jordan's lemma and the residues theorem can be applied. The fact that $\mathrm{Im}\{\chi\} \neq 0$ is a consequence of the introduction of a small imaginary parameter that mimics some form of dissipation in the equations of motion.

This is necessary, especially when calculating the the linear analytical solution of the problem $\mathbf{A}\hat{\mathbf{x}} = \hat{\mathbf{b}}_o$, in order to overcome the famous mathematical ambiguity discussed by Lighthill (1978, chap.3). See section 2.5 for further details about that.

Back to the integrals of equation (2.63), remember that the real function $f(s)$ of a real variable s can always be decomposed as a sum of its even part and its odd one, i.e. $f(s) = f_E(s) + f_O(s)$, with $f_E(s) = [f(s) + f(-s)]/2$ and $f_O(s) = [f(s) - f(-s)]/2$. This means that in the integral (2.63) only one of the two gives a nonzero contribution according to the parity of $f(s)s^\gamma$. The parameters $\gamma \in [0, 6] \subset \mathbb{N}$ and $\nu \in [1, 2] \subset \mathbb{N}$ come from the structure of the C_{ij} polynomials introduced above.

By Fourier transforming along s, which corresponds to decompose the function on the Fourier basis $\{\mathrm{e}^{isk}\}_{k\in\mathbb{R}}$, and by extending the integral in the complex s plane, the path of integration can be correctly closed in the upper half-plane or in the lower one following the Jordan's lemma. With the definition of

$$f(s) = \frac{1}{\sqrt{2\pi}} \int_{-\infty}^{+\infty} \mathrm{d}k\, \mathrm{e}^{iks} \hat{f}(k) \tag{2.64}$$

and a little algebra, the residues theorem gives

$$P \int_{-\infty}^{\infty} \mathrm{d}s\, f(s) \frac{s^\gamma}{D^\nu} = 2i\sqrt{2\pi} \int_0^{+\infty} \mathrm{d}k \hat{f}(k) \sum_{\mathrm{UP}} \mathrm{Res} \left\{ \frac{s^\gamma \mathrm{e}^{iks}}{D^\nu} \right\}, \tag{2.65}$$

where UP denotes the upper half-plane corresponding to $\mathrm{Im}\{s\} > 0$. The advantage of this approach is that the residues that appear in the last equation can be calculated analytically while the form of the function $f(s)$ may not be known analytically.

Energy transfer coefficients

Once the integrals along the k_y axis are performed, the final step to have a simple measure of the relative importance of a certain interaction of waves in the generation of the double inertial energy peak of the l-th wave is to integrate equation (2.62) around the value $k_x = 2f/U$. In particular, the following coefficients can be defined

$$\epsilon_l = \int_{I(2f/U)} \mathrm{d}k_x\, \tilde{E}_l, \tag{2.66}$$

$$\phi_l^0 = \frac{1}{\epsilon_l} \int_{I(2f/U)} \mathrm{d}k_x\, \tilde{\Psi}_l^0, \tag{2.67}$$

$$\phi_{nml}^1 = \frac{1}{\epsilon_l} \int_{I(2f/U)} \mathrm{d}k_x\, \tilde{\Psi}_{nml}^1, \tag{2.68}$$

$$\phi_{qsnml}^2 = \frac{1}{\epsilon_l} \int_{I(2f/U)} \mathrm{d}k_x\, \tilde{\Psi}_{qsnml}^2, \tag{2.69}$$

where

$$I(2f/U) = \{k_x \in \mathbb{R} : 2f/U - \Delta k_x \leq k_x \leq 2f/U + \Delta k_x\}, \tag{2.70}$$

with an appropriate Δk_x. As for the calculation of the DIE(l) of equation (2.41), $\Delta k_x = 0.2f/U$ and it was checked that the results are not sensitive to small changes in the choice of this value, as far as only the double inertial peak is included in the integrals. Thanks to these definitions, equation (2.62) becomes

$$1 = \phi_l^0 + \sum_{n,m=1}^{+\infty} \phi_{nml}^1 + \sum_{q,s,n,m=1}^{+\infty} \phi_{qsnml}^2 \tag{2.71}$$

and each of the three addenda express the relative contribution of linear, first order advection and second order advection terms to the energy of mode l in the double inertial range.

In order to show the results, all the series that appear in equations (2.62) and (2.71) are stopped to a certain modenumber M, so that the truncated energy spectral density is defined as

$$\tilde{E}_l^{(M)}(k_x) = \tilde{\Psi}_l^0 + \sum_{n,m=1}^{M} \tilde{\Psi}_{nml}^1 + \sum_{q,s,n,m=1}^{M} \tilde{\Psi}_{qsnml}^2, \tag{2.72}$$

which leads to the definition of the truncated double inertial energy

$$\epsilon_l^{(M)} = \int_{I(2f/U)} \mathrm{d}k_x \, \tilde{E}_l^{(M)} \tag{2.73}$$

and the truncated coefficients $\phi_l^{0(M)}$, $\phi_{nml}^{1(M)}$ and $\phi_{qsnml}^{2(M)}$. Those are defined as in (2.67)-(2.69) with $\epsilon_l^{(M)}$ instead of ϵ_l, which means that equation (2.71) holds even for these truncated coefficients.

2.5 Results

In this section the energy transfer coefficients defined above, which, thus, satisfy

$$1 = \phi_l^{0(M)} + \sum_{n,m=1}^{M} \phi_{nml}^{1(M)} + \sum_{q,s,n,m=1}^{M} \phi_{qsnml}^{2(M)}, \tag{2.74}$$

the truncated version of equation (2.71), are calculated analytically from the linear solution of the problem $\mathbf{A}\hat{\mathbf{x}} = \hat{\mathbf{b}}_o$, whose terms are defined in equation (2.45).

Linear analytical solution

The solution of the linear problem describing the system under study are obtained by transforming the spectral variables

$$\hat{\mathbf{x}} = \mathbf{A}^{-1}\hat{\mathbf{b}}_o \tag{2.75}$$

back to the physical space, which is done as explained below.

In the first place, a famous ambiguity arises. It comes from the fact that the mathematical problem includes wave solutions coming from infinity, but the physical problem describes waves excited by the forcing acting in the domain considered. This ambiguity can be solved by adding an imaginary part to the frequency ω or the wavenumber k_x (in this problem this is achieved by replacing k_x with $k_x - i\delta$, $\delta > 0$) before inverting the Fourier integrals of equation (2.75) and then by taking the limit where the imaginary part goes to zero (Lighthill, 1978, chap. 3). Therefore, the linear solutions formally are

$$\mathbf{x} = \begin{pmatrix} u_l \\ v_l \\ r_l \end{pmatrix} = \lim_{\delta \to 0} \frac{1}{2\pi} \iint_{-\infty}^{\infty} \mathrm{d}k_x \mathrm{d}k_y \, \mathrm{e}^{i(k_x \xi + k_y y)} \hat{\mathbf{x}}(k_x - i\delta, k_y) \tag{2.76}$$

where

$$\hat{\mathbf{x}}(k_x - i\delta, k_y) = \left(\mathbf{A}^{-1} \hat{\mathbf{b}}_o \right) \big|_{k_x = k_x - i\delta}. \tag{2.77}$$

While inverting the Fourier integrals of the above, the technique introduced in section 2.4 to overcome the singularities due to the W function is used. In particular, these inverse Fourier integrals are rewritten as in equation (2.63), with s representing here the along-track wavenumber k_x. Then, by applying once again the residues theorem, the linear solutions can be written as a function of the Fourier transform of the Fourier transform of the forcing wind stress. As an example, here is the linear solution for v_l,

$$v_l(\xi, y) = \frac{1}{\sqrt{2\pi}} \int_{-\infty}^{+\infty} \mathrm{d}k_y \left\{ \frac{1}{U^2 - c_l^2} \left[-\frac{k_y c_l^2}{U} \cos(k_y y) + f \sin(k_y y) \right] J(\xi, k_y) + \frac{\cos(k_y y)}{U} Y(\xi, k_y) \right\} \tag{2.78}$$

with

$$J(\xi, k_y) = \int_0^{+\infty} \mathrm{d}q \, \mathrm{FT} \left\{ \mathrm{e}^{ik_x \xi} \mathrm{Im}\{\hat{\tau}_l^x(k_x, k_y)\} \right\} \frac{1}{a} \sin(qa), \tag{2.79}$$

$$Y(\xi, k_y) = \int_0^{+\infty} \mathrm{d}q \, \mathrm{FT} \left\{ i\mathrm{e}^{ik_x \xi} \mathrm{Im}\{\hat{\tau}_l^y(k_x, k_y)\} \right\} \cos(qa), \tag{2.80}$$

where FT denotes the Fourier transform along the k_x direction, namely

$$\mathrm{FT}\{f(k_x)\}(q) = \frac{1}{\sqrt{2\pi}} \int_{-\infty}^{+\infty} \mathrm{d}k_x \mathrm{e}^{-iqk_x} f(k_x) \tag{2.81}$$

and a is given by

$$a = \sqrt{\frac{f^2 + c_l^2 k_y^2}{U^2 - c_l^2}}. \tag{2.82}$$

As already mentioned, this approach makes it possible to find the linear steady solution even in the case where the wind stress is not known analytically. Thus, in principle, the wind forcing could be given by observations.

The analytical solutions are computed for the first $M = 10$ modes on a bigger grid compared to the one used in the numerical simulation, to have a finer wavenumber

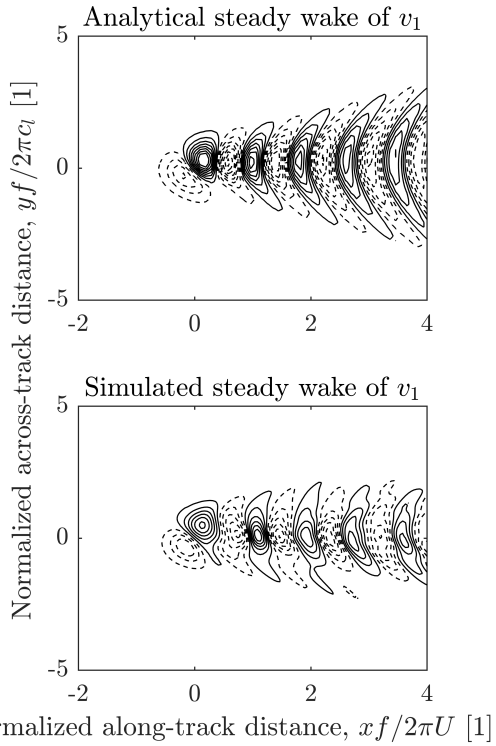

Figure 2.8: Steady wave wake of the v velocity component projected on the first internal mode. The contour lines go from -0.15 m s^{-1} to 0.15 m s^{-1} with a step of 0.02 m s^{-1}. Solid contours are for positive values and dashed contours for negative ones. The along-track distance from the center of the storm is normalized by the inertial wavelength $2\pi U/f$, while the across-track distance is normalized by the wavelength associated to the baroclinic radius of deformation, i.e. $2\pi c_l/f$.

step. The grid is 64×10^3 km long in the longitudinal direction and 24×10^3 km in the latitudinal one, with grid spacing $\Delta x = \Delta y = 80$ km. Figure 2.8 shows the wave wake for the first projection of the v field calculated analytically (upper panel) and obtained from the numerical simulation (lower panel).

Double inertial energy transfer coefficients

Once the linear u_l, v_l, r_l are known for many l, one can compute the advection terms of equations (2.20), (2.21), (2.25) and then the spectral functions of equations (2.59)-(2.61). The integrals along k_y (as explained in section 2.4) and the integrals around the double inertial peak are finally calculated to find the truncated coefficients of equation (2.74). These coefficients, once again, measure the energy exchanged between the l-th

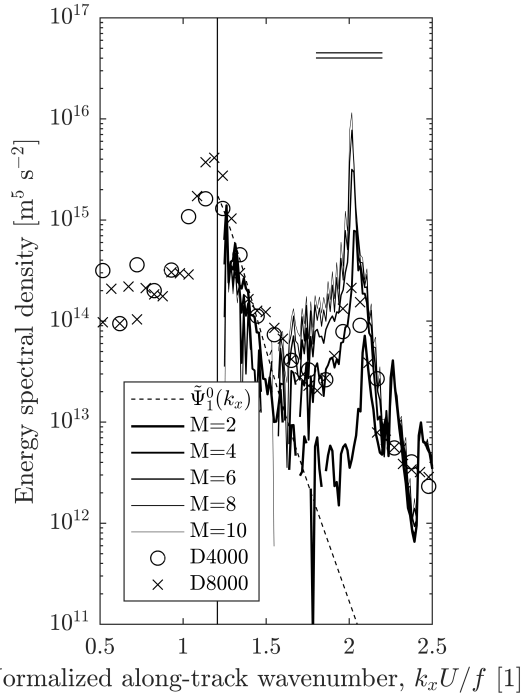

Figure 2.9: The dashed line shows the linear spectrum $\tilde{\Psi}_l^0(k_x)$ with $l = 1$. The solid lines show the truncated energy spectral density $\tilde{E}_l^{(M)}(k_x)$, as in equation (2.72), for some values of M. The peak near $k_xU/f = 2$ increases with increasing M. The circles show the total energy spectral density $\tilde{E}_l(k_x)$ obtained from the simulation D4000 and the crosses from the simulation D8000. The horizontal double line marks the interval of integration $I(2f/U)$ of equation (2.70).

mode double inertial peak and the q-th, s-th, n-th and m-th waves.

As shown in figure 2.9, the net effect of nonlinear interactions is to add energy to the double inertial range. In the same figure, one can also see that the variation of M in the range $[6, 10]$ does not influence the position of the double inertial peak. Its height changes because more and more interactions are taken into consideration and, in the analytical solution, they are all certainly happening. Thus, compared to the numerical spectra, the analytical solution gives an upper bound to the height of the double inertial peak, in the case that all possible interactions among the waves in the wake behind the storm are exchanging energy. The peaks in the D8000 spectrum are higher than the D4000 ones both because the domain is larger (the D8000 domain is twice as large as the D4000 one) and because more wave interactions happen and bring energy to the double inertial peak.

In order to quantify the role of the single interaction of waves in the generation of the

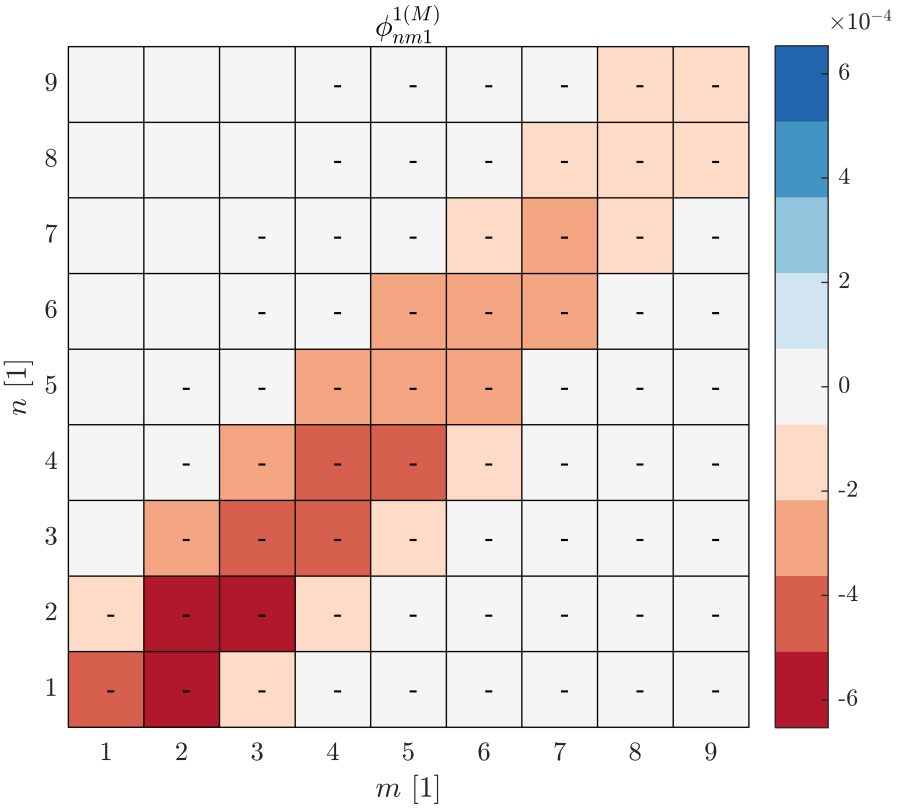

Figure 2.10: $\phi^{1(M)}_{nml}$ coefficients for $M = 10$, $n, m \in [1, 9]$ and $l = 1$. The minus denotes negative values.

first mode double inertial peak, the coefficients $\phi^{1(M)}_{nml}$ are shown in figure 2.10 for $l = 1$, $n, m \in [1, 9]$, $M = 10$ and the coefficients $\phi^{2(M)}_{qsnml}$ in figure 2.11 for $l = 1$, $n, m \in [1, 6]$, $q, s \in [1, 6]$ and $M = 10$. Positive values correspond to nonlinear interactions that bring energy to the l-th mode double inertial peak from the interacting waves, while negative values correspond to interactions that take energy away from the l-th mode double inertial peak. There is no balance between the sum of all the positive coefficients and the negative ones, because that would correspond to a zero net contribution of the nonlinear interactions in the generation of the double inertial peak and to an energy spectral distribution decaying as $\tilde{\Psi}^0_l(k_x)$, i.e. with no double inertial peak. A total zero sum could be expected if the coefficients under study were energy exchange rates and not integrated energy transfer, as they are in the present work.

The following figures (2.12 - 2.15) confirm the description of the energy exchanges between near-inertial and double inertial waves of different modes, by showing the same coefficients $\phi^{1(M)}_{nml}$ and $\phi^{2(M)}_{qsnml}$ for $l = 2$ and $l = 3$. In this way some general features can

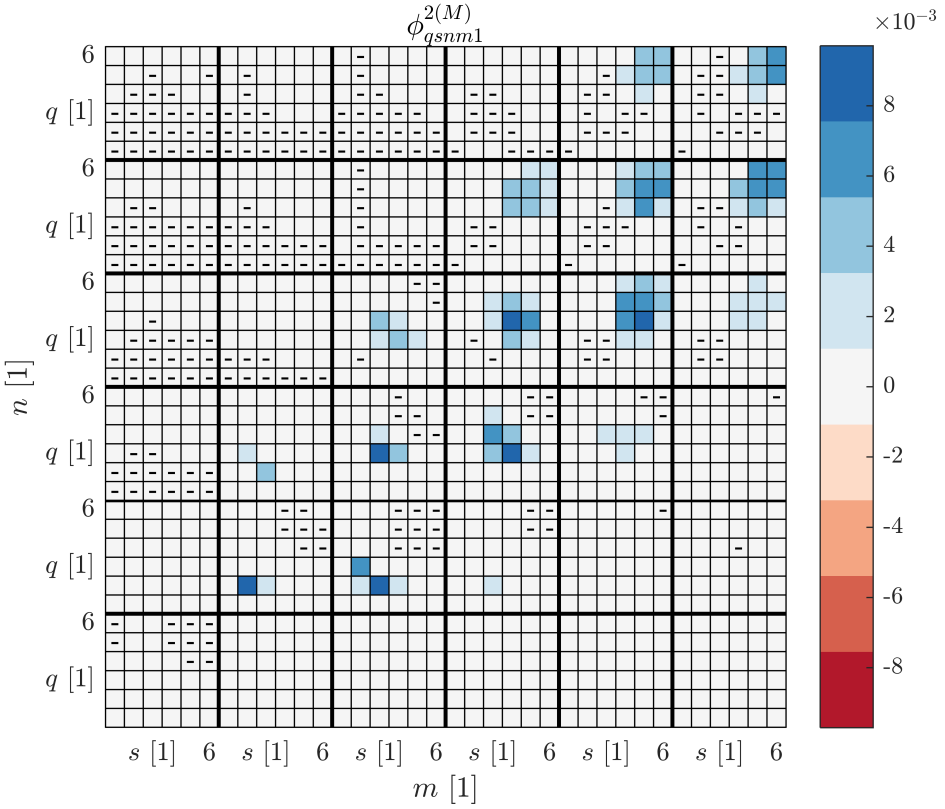

Figure 2.11: $\phi^{2(M)}_{qsnml}$ coefficients for $M = 10$, $q, s \in [1, 6]$, $n, m \in [1, 6]$ and $l = 1$. The minus denotes negative values.

be drawn. First of all, the geometrical constraint due to the structure of the α_{nml}, β_{nml}, λ_{nml} and μ_{nml} coefficients, i.e. the triangle condition on the modenumbers, appears in all the cases. In particular, the dominant coefficients in figures 2.10 - 2.15 are always the one with (n =2 or 3, $m = l + n$) or (q =2 or 3, $s = l + q$, n =2 or 3, $m = l + n$). It was proved that the entire interpretation of the mechanism does not depend on the value of M, as far as it is high enough to capture the dominant interaction for the selected mode. This means that for the first three modes, the figures 2.10 - 2.15 are qualitatively the same for $M \in [6, 10]$, in the sense that the relative importance of the coefficients with respect to one another is independent of M.

The same coefficients of figures 2.10 - 2.15 were calculated using the waves simulated in D4000 and D8000 and very small differences with the coefficients shown here were found, of the order of few percent points (not shown). This means that the presence of some energy in the double inertial range of the interacting waves does not influence the picture of the mechanism outlined above.

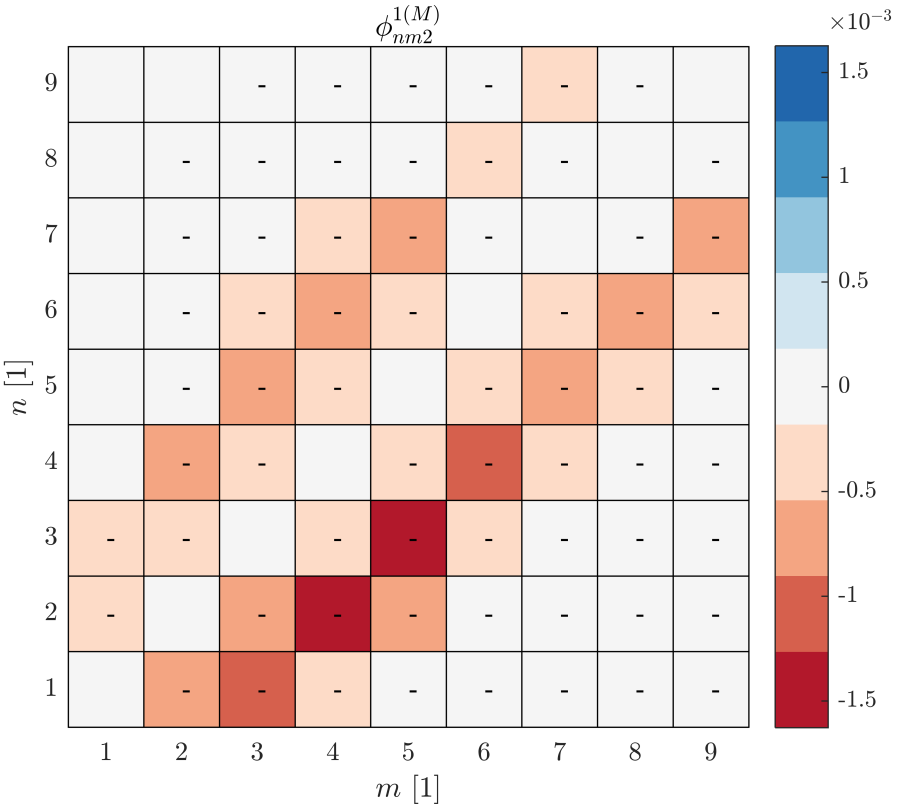

Figure 2.12: $\phi^{1(M)}_{nml}$ coefficients for $M = 10$, $n, m \in [1, 9]$ and $l = 2$. The minus denotes negative values.

2.6 Discussion and conclusions

The generation mechanism of the double inertial frequency waves is analyzed using the internal mode decomposition and defining analytically the coefficients of equations (2.68) and (2.69), that measure the relative importance of the contribution of the interacting modes (q, s, n, m)-th to the double inertial frequency range of the power spectrum of the reference mode l. The analytical theory describes the nonlinear interactions of the linear solutions of the problem, which are compared to the fully nonlinear solutions obtained from two numerical simulations. This gives a more detailed view of the process compared to previous works (Niwa and Hibiya, 1997; Danioux and Klein, 2008; Zedler, 2009), in a realistic setting with a non-uniform oceanic stratification profile and it highlights the role played by superinertial waves to ocean interior mixing.

First of all, let us comment the apparent discrepancy between Niwa and Hibiya (1997) and Zedler (2009) identification of the depth at which nonlinear interactions take place. In the present analysis, it is found that the relatively dominant interactions which bring

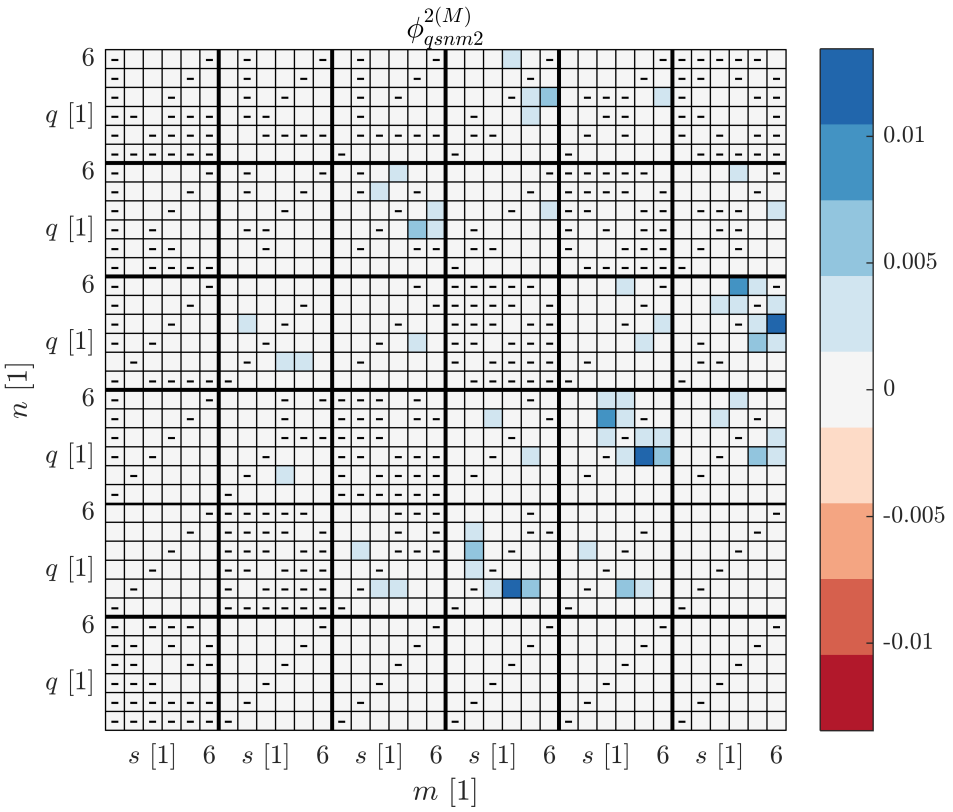

Figure 2.13: $\phi^{2(M)}_{qsnml}$ coefficients for $M = 10$, $q, s \in [1, 6]$, $n, m \in [1, 6]$ and $l = 2$. The minus denotes negative values.

energy to the low modenumber double inertial range waves generally involve a second or third mode wave ($n = 2$ or 3). This suggests that nonlinear interactions are important where the second and third modes peak, i.e. in the range 1000-2500 m for the h_n modes and in the region of 500-750 m for the h_{nz} modes (see figure 2.6). As pointed out in the introduction, according to a WKB-like scaling, the energy should scale vertically as the buoyancy frequency profile and, thus, most of the energy exchanges would take place at the base of the mixed layer (see figure 2.5). Thus, the present analysis supports the idea that Niwa and Hibiya (1997) and Zedler (2009) interpretations of the depths at which nonlinear interactions take place is different simply because they use different vertical buoyancy frequency profiles but also that a simple WKB-like scaling would underestimate the depth at which nonlinear interactions are important.

Moreover, concerning the first mode ($l = 1$), which contains most of the double inertial frequency energy, figure 2.11 proves that high mode near-inertial energy is transferred to the first mode double inertial peak, which is consistent with the results of Niwa and Hibiya (1997). This can be shown to correspond to a faster lateral energy propagation

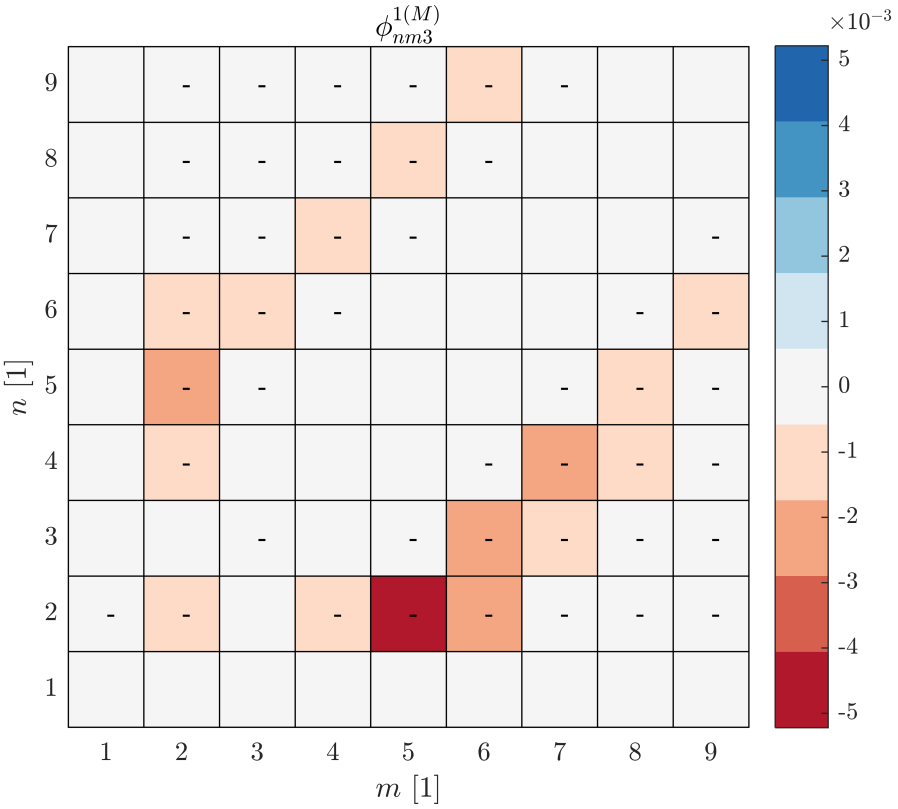

Figure 2.14: $\phi^{1(M)}_{nml}$ coefficients for $M = 10$, $n, m \in [1, 9]$ and $l = 3$. The minus denotes negative values.

speed and must be taken into account when studying the radiation of energy from a wake excited by a tropical cyclone. In particular, one can find a sufficient condition for having an increase of the lateral energy propagation speed during the transfer of energy from a high mode near-inertial wave to a low mode double inertial one for an exponential stratification, $N(z) = N_o e^{z/\lambda}$ with $z \in [-H, 0]$, as follows. First of all, for l-th mode waves, the dispersion relation is

$$\omega_l = \sqrt{f^2 + c_l^2(k_x^2 + k_y^2)} \tag{2.83}$$

and the magnitude of the group speed as a function of frequency is

$$|\mathbf{c}_{gl}(\omega_l)| = c_l \sqrt{1 - \frac{f^2}{\omega_l^2}}. \tag{2.84}$$

Therefore, at the Geisler frequency $\omega_l = \omega_{Gl}$ of equation (2.13) and at the double inertial

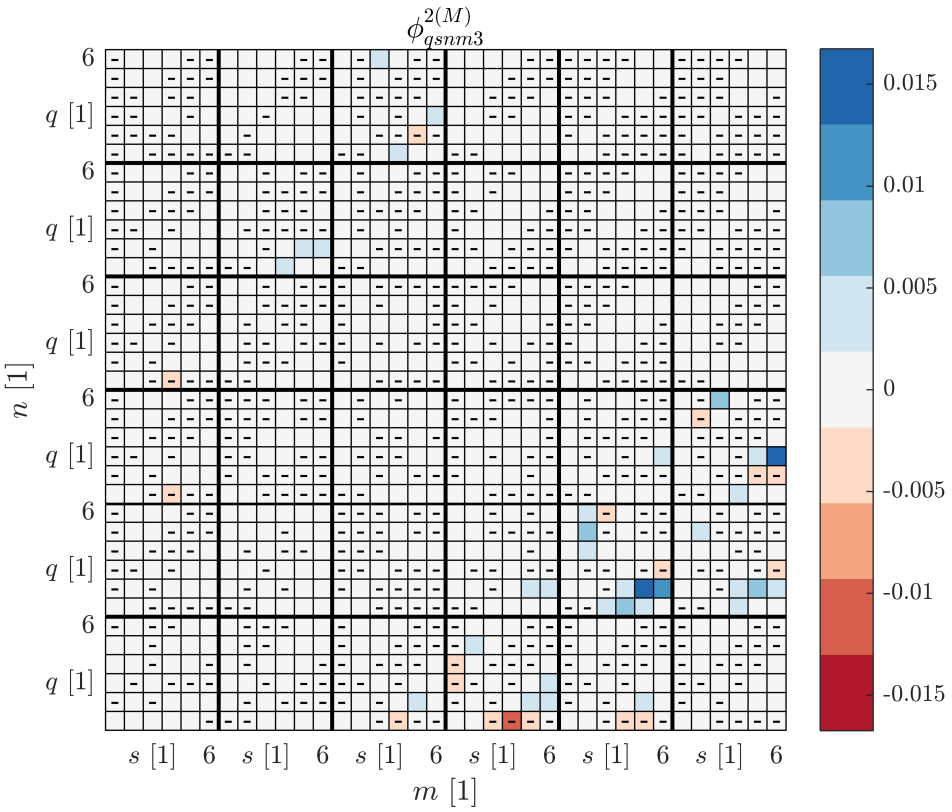

Figure 2.15: $\phi^{2(M)}_{qsnml}$ coefficients for $M = 10$, $q, s \in [1, 6]$, $n, m \in [1, 6]$ and $l = 3$. The minus denotes negative values.

frequency $\omega_l = 2f$,

$$|\mathbf{c}_{gl}(\omega_{Gl})| = \frac{c_l^2}{U}, \tag{2.85}$$

$$|\mathbf{c}_{gl}(2f)| = c_l\sqrt{\frac{3}{4}}. \tag{2.86}$$

Considering now the ratio of the magnitude of the group speed of the m-th mode at the near-inertial frequency ω_{Gm} to the magnitude of the group speed of the l-th mode at the double inertial frequency one writes

$$Q_{m,l} = \frac{|\mathbf{c}_{gm}(\omega_{Gm})|}{|\mathbf{c}_{gl}(2f)|} = \frac{c_m^2/U}{c_l\sqrt{3/4}} = \frac{\overline{U}_{m,l}}{U} \tag{2.87}$$

with $\overline{U}_{m,l} = 2c_m^2/c_l\sqrt{3}$. If the condition $Q_{m,l} < 1$ is fulfilled, the transfer of energy from the m-th mode near-inertial range to the l-th mode double inertial range results in an increase of the propagation velocity of the energy itself. The same condition can

be written as $U > \overline{U}_{m,l}$. An analytical expression of $\overline{U}_{m,l}$ can be found in the case of exponential stratification of a deep ocean, i.e. $N(z) = N_o e^{z/\lambda}$ with $z \in [-H, 0]$ and with $H/\lambda \gg 1$. In such a case, the eigenspeeds are given by the implicit condition

$$J_o(\lambda N_o / c_l) = 0, \tag{2.88}$$

where $J_o(x)$ is the zero-th order Bessel function of the first kind. Thus, if X_l denotes the l-th zero of the function $J_o(x)$, the eigenspeeds are

$$c_l = \frac{\lambda N_o}{X_l} \tag{2.89}$$

and, in turns,

$$\overline{U}_{m,l} = \frac{2}{\sqrt{3}} \frac{X_l}{X_m^2} \lambda N_o. \tag{2.90}$$

Since the zeros of the Bessel function J_o increases with l, one finds immediately that $\overline{U}_{m,l} \leq \overline{U}_{2,1} \forall m > l$, thus the condition on the ratio of the group speeds introduced above, $Q_{m,l} < 1$, becomes $U > \overline{U}_{2,1} \simeq \lambda N_o \times 10^{-1}$. This means that if the cyclone translation speed U exceeds the threshold value $\overline{U}_{2,1}$, a transfer of energy from a high mode near-inertial range to the first mode double inertial one correponds to an increase in lateral energy propagation speed. Considering as upper bound the values $N_o \simeq 10^{-2}$ s^{-1} and $\lambda \simeq 10^3$ m (Pickard and Emery, 1990), one finds $\overline{U}_{2,1} \simeq 1$ m s^{-1} which means that for nearly all the tropical cyclones, that generally move with a translation speed between 1 m s^{-1} and 10 m s^{-1}, the transfer of energy from a high mode m near-inertial range to a low mode l double inertial range corresponds to an increase of the lateral energy propagation speed. Since for the modes $l = 1, 2, 3$ this kind of transfer is very common (in correspondence of all the positive values of figures 2.10 - 2.15), nonlinearities account for an increase of the lateral energy propagation speed from the wake excited by a tropical cyclone.

On the other hand, the presence of negative values in figures 2.10 - 2.15 (in particular in figures 2.10, 2.12 and 2.14) shows energy flowing from the double inertial range of mode l to some higher mode $n, m > l$. This is in agreement with the possibility of a parametric subharmonic instability mechanism acting in the wave wake (McComas and Müller, 1981) and, since this energy is going towards high modes, these figures explicitly show a step in the cascade towards small scales, where the mixing happens.

Thus, the complete underlying mechanism that is found and that is in full agreement with the recent results of Wagner and Young (2016) can be summarized in few steps:

- the wind stress inputs energy in the near-inertial range of all vertical modes;
- nonlinear interactions bring part of this energy towards the double inertial range (which means that the waves are less likely to undergo critical latitude reflection) of the lowest modes (which have a higher horizontal group speed);
- the double inertial energy, which has been brought further and faster compared to a purely linear system, is transferred back to the near-inertial range of some high vertical mode, i.e. energy flows towards the small mixing scales.

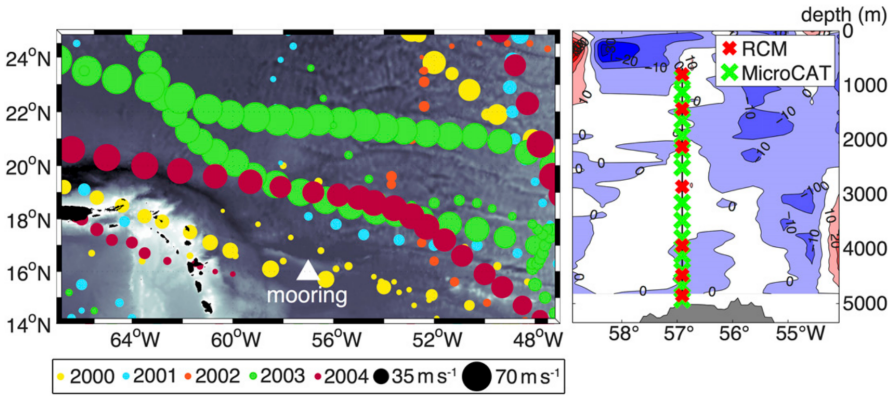

Figure 2.16: Left panel: location of the mooring station and tropical cyclone tracks between 2000 and 2004 (HURDAT2 dataset). Right panel: vertical structure of the mooring with RCM (currents) and MicroCAT (pressure, salinity and temperature). In the background a section of the horizontal velocity measured in a cruise in June 2000 (Köhler et al., 2018).

In the present analysis, the temporal evolution of the nonlinear interactions has not been analyzed, as the focus has been on the equilibrated oceanic response. It would be interesting to study in a future work the time scale for such equilibrated state to be reached.

2.7 Comparison with observations

Preliminary analysis on a dataset of current and temperature measurements in the north-western Atlantic, at 16°N (Köhler et al., 2018), highlight the possibility of observing some of the features developed in the theory described above. Köhler et al. (2018) show that the most prominent changes in the near-inertial range of the measured signal are due to the passage of internal waves excited by tropical cyclones. The database consists of a 5-yr mooring time series of horizontal velocity, temperature, salinity and pressure in a 5 km water column. The left panel of figure 2.16 shows the location of the mooring (denoted with a white triangle) and the tracks of the tropical cyclones that passed in the area in the years 2000-2004 (from the HURDAT2 dataset). The right panel of the same figure shows the vertical structure of the mooring with RCM (Recording Current Meter) measuring the currents and MicroCAT measuring the pressure, temperature and salinity of the water column, together with a vertical section of the horizontal current measurements taken from a cruise in June 2000.

In their analysis, Köhler et al. (2018) find that in the 2003-2004 hurricane season there is an increase of depth-mean near-inertial energy by a factor of 3.8 with a delay of 2 to 3 weeks after the passage of two intense hurricanes, Isabel and Fabian, in the region.

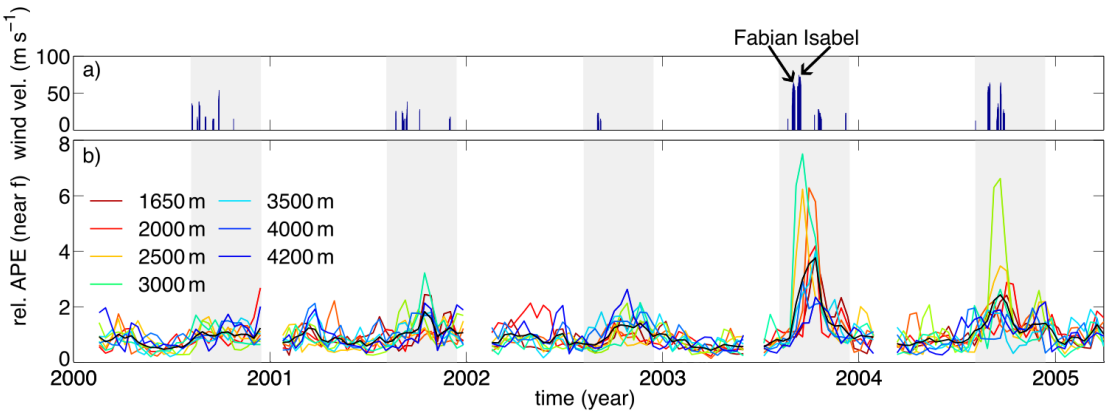

Figure 2.17: (a) Wind speed time series of the hurricanes in the region $[15; 25]$°N latitude and $[45; 70]$°W longitude (HURDAT2 dataset). (b) Time series of the near-inertial APE, see equation (2.91), normalized by its time-average value at different depths (colored curves) and the deth-mean near-inertial APE normalized in the same way (black curve). Adapted from Köhler et al. (2018).

This can be seen in figure 2.17, where (a) the wind speed of the hurricanes passing in the region between 15°N and 25°N latitude and 45°W and 70°W longitude and (b) the normalized near-inertial available potential energy at the different depths are shown. In particular, the available potential energy is the quantity

$$\text{APE} = \frac{1}{2}\overline{\rho}N^2\eta^2, \tag{2.91}$$

where $\overline{\rho}$ is the depth average density, N is the buoyancy frequency and η is the internal wave-induced vertical displacement obtained from the temperature measurements as

$$\eta = \frac{T - T_7}{\mathrm{d}T_7/\mathrm{d}z}, \tag{2.92}$$

with T_7 denoting the 7-day low-pass filtered temperature time series. The near-inertial range is here defined as $[f - 0.15 \text{ cpd}; f + 0.3 \text{ cpd}]$, with $f = 0.55$ cpd being the value of the Coriolis parameter at the latitude of the mooring, i.e. 16°N.

Further investigations show that a considerable fraction of the observed increase of APE in 2003 comes from the latitudes where the hurricanes transit (Köhler et al., 2018), directly proving that the near-inertial internal waves excited by tropical cyclones can propagate for hundreds of kilometers and bring energy far from their generation region. Figure 2.18, then, shows a detail of the near-inertial vertical displacement time series for the 2003-2004 hurricane season.

This kind of analysis suggests to go further and to explore the possibility to compare the data with the theoretical description of the problem described in the previous sections. Preliminary analysis on the double inertial response show that the double inertial

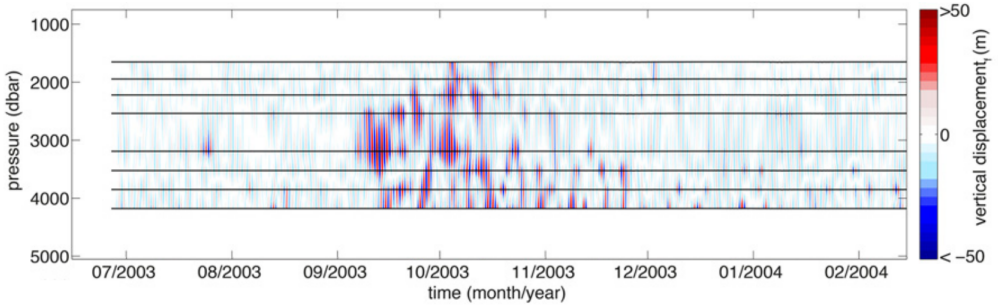

Figure 2.18: Near-inertial $[f - 0.15$ cpd$; f + 0.3$ cpd$]$ vertical displacement time series for the 2003-2004 hurricane season. There is a clear signal in the month of September, i.e. after the passage of Isabel and Fabian in the region. Adapted from Köhler et al. (2018).

waves propagate faster than the near-inertial ones, which is consistent with the theory. With the knowledge of the fine structure vertical buoyancy profile of the region, then, it is possible to calculate the internal modes, which, together with the structure of the surface wind stress of hurricanes Isabel and Fabian, enable to calculate the linear analytical steady solution of the three dimensional wave wake. Once the wave wake is known, the comparison of the analytical solution with the observations will possibly highlight some spatial and temporal features of nonlinear interactions leading to the generation of the double inertial peak.

At the same time, since the theory developed so far focuses only on the steady oceanic response, it is planned to further investigate the time evolution of the wake from a theoretical point of view in order to quantify where and when the nonlinear interactions take place. This would surely support and be supported by the comparison between data and observations. Other factors that are planned to be included in the theory in the near future are the β effect (Gill, 1984; Niwa and Hibiya, 1997) and the interaction with a varying bottom topography.

Finally, a suggestion for a future measurement campaign would be to have a mooring also on the northern side of the hurricane track, in order to be able to reduce the near-inertial signal thanks to the critical latitude reflection. With an array of mooring, then, it would also be possible to monitor the time evolution of the wake, so that the analytical solution could be constrained further.

Three

SST role in the modulation of HPEs

The mechanisms controlling the influence of the sea surface temperature (SST) structure on the surface winds are studied by means of realistic numerical simulations run with a non-hydrostatic fully compressible primitive equation model in a midlatitudes pre-convective rain setup, leading to the 9 October 2014 Genoa heavy precipitation event (HPE). Starting from a simulation with high resolution submesoscale eddy-permitting SST field (with grid spacing of 1.4 km), a series of simulations is run with SST forcings whose horizontal gradients are enhanced (or attenuated) at the same spatial resolution and another series is forced with coarser and coarser SST fields. Statistically significant spatial correlation coefficients between the appropriately defined quantities show that the marine atmospheric boundary layer responds to the submesoscale SST forcing structures over time scales of the order of hours. In particular, through the downward momentum mixing mechanism, the presence of SST horizontal gradients impacts the spatial structure of the surface wind convergence, which is likely to displace the convective heavy rain bands that develop over the sea.[1]

3.1 Introduction

Heavy convective rainfalls

Along the coasts of the Mediterranean sea, the vicinity of relatively high orography to the sea and, thus, the consequent strong gradients in the air properties (pressure, temperature, moisture) are thought to be a key factor in the generation of the so-called heavy-rain-producing mesoscale convective systems (MCSs). This kind of systems, which are typically embedded in larger synoptic structures, by bringing large volumes of rain in few hours and over areas of the order of 100 km^2 (Ducrocq et al., 2014), can trigger consistent hydrological responses, that can cause economical damages and even casualties (Gaume et al., 2009; Nuissier et al., 2008; Llasat et al., 2013).

[1]For most part, this chapter has been submitted for peer-review as Meroni, A. N., A. Parodi and C. Pasquero, 2018 (expected): Role of the horizontal SST structure in the modulation of heavy precipitations over the Ligurian Sea. *J. Geophys. Res. Atmos.*

The reason why such rainfalls are so intense is because multiple convective cells are regenerated in the same position at the same rate at which they are advected away (Chappell, 1986; Schumacher and Johnson, 2005; Ducrocq et al., 2008; Schumacher and Johnson, 2008, 2009). This condition can be reached in a scenario where in a quasi-stationary synoptic system, a low-level moist and conditionally unstable jet, typically blowing from the sea, is lifted by the presence of some orographic barrier (Ducrocq et al., 2008) or some cold dry continental air mass (Davolio et al., 2016; Fiori et al., 2017). These four elements (conditionally unstable atmosphere, low-level moisture, slow-evolving synoptic conditions and mesoscale lifting) are crucial ingredients in the development of such MCSs (Nuissier et al., 2008; Fiori et al., 2017).

The origin of the low-level moisture in heavy precipitation events (HPEs) in the northwestern Mediterranean is studied by means of numerical simulations by Dufforg and Ducrocq (2011). They find that both the Mediterranean sea and the Atlantic ocean can act as significant sources of moisture, with relative importance determined by the vorticity of the large-scale synoptic structure (cyclonic or anticyclonic). These findings are in good agreement with Pinto et al. (2013) showing that the strongest rainfall events over the Northwest Italy are characterized by strong and persistent upper air troughs inducing not only moisture advection from the North Atlantic into the western Mediterranean, but also strong northward flow towards the southern Alpine ranges. Homar et al. (2002); Nuissier et al. (2008) study the synoptic conditions leading to HPEs through numerical simulations, while surface gauge observations and reanalysis are combined to study the large-scale patterns producing HPEs by Romero et al. (1999) for southern Spain, Rudari et al. (2005) for northern Italy and Nuissier et al. (2011) for southern France. Dayan et al. (2015) give a general review of these large-scale dynamical structures that cause HPEs all over the Mediterranean sea.

The numerical simulations of Pastor et al. (2001) and Lebeaupin et al. (2006) show that, by changing the average temperature over a certain area near the precipitation, the total amount of rainfall is modified: the warmer the sea, the more it rains. On the other hand, Lebeaupin et al. (2006); Pastor et al. (2015) show that in their simulations the convection that causes the heavy rain can be shut off by sufficiently cold SST patches near the convection itself. Other works have investigated the effects on HPE forecast of an increase in the horizontal resolution of the SST in numerical simulations. Millán et al. (1995); Pastor et al. (2001); Lebeaupin et al. (2006); Cassola et al. (2016) generally find that a SST forcing with higher spatial resolution leads to a better forecast in terms of spatial distribution and/or rainfall temporal peaks, but does not seem to affect the total precipitation volume much. In particular, Cassola et al. (2016), by simulating a HPE with different initialization time, show that an increased SST horizontal resolution typically leads to more realistic precipitation peaks for the 36-48 h forecast. Other works, such as Katsafados et al. (2011), show evidence of the importance of the upper troposphere dynamics in the control of heavy precipitations. In their numerical simulations of an explosively developing storm over the eastern Mediterranean, they show that when they change the sea surface temperature (SST) forcing with four different realistic fields, the general structure of the precipitation is unaffected. The location of the rain bands

and the spatial structure of the local heat fluxes, instead, show a significant dependence on the SST, which is also found in the coupled atmosphere-ocean numerical simulations of Carniel et al. (2016); Ricchi et al. (2016, 2017).

Concerning the tiggering of such events, Ducrocq et al. (2008) use a regional atmospheric model to show that different HPEs can be triggered and maintained in the same position by different mechanisms. In fact, the mesoscale lifting necessary to initiate the convection can be provided by the orography or by the surface wind convergence, which, in turns, is typically generated by the encounter of a relatively warm and moist low-level jet with a colder and drier continental air mass or the cold pool due to the rain evaporation itself. Fiori et al. (2017), by means of very high horizontal resolution numerical simulations (250 m grid spacing), explain in details how a cold dry continental air mass plays the role of a virtual orographic barrier in lifting the moist warm low-level jet that produces the HPE considered. The same mechanism occurred also in historical events (Parodi et al., 2017).

SST-wind relationship

Since it is known that the SST structure can control the dynamical and thermodynamical properties of the marine atmospheric boundary layer (Small et al., 2008), one of the possible ways through which the SST can influence heavy convective rains is by modifying surface wind convergence. Evidence of that comes from, for example, Toy and Johnson (2014), who, by comparing different kind of observations (ground-based rain gauges, satellites and radar data) with numerical simulations, are able to assess that the presence of a moderately sharp meridional SST gradient (roughly 1 K / 100 km for 200 km) is fundamental to have the surface wind convergence necessary to correctly simulate the heavy rainfall under study. Minobe et al. (2008) give another example of control of the SST on convective precipitations. Combining both observations and model simulations, they find that the Gulf Stream has an influence on the entire troposphere, through the locking of a band of convective rain along the profile of the Gulf Stream itself. This happens following a pressure gradient adjustment in the marine boundary layer, which determines the position of the convergence line, as shown in figure 3.1. On the same spatial scales of $O(100\text{ km})$, a similar process has been observed over SST mesoscale eddies in the tropical ocean (Li and Carbone, 2012). There, the surface convergence associated with the laplacian SST structure appears to be an order of magnitude larger than the regional background surface convergence and, thus, is thought to be responsible for the initiation of most of the observed convective rain events.

In order to explain this relationship between surface wind convergence and mesoscale SST structure, two basic mechanisms acting in the marine boundary layer have been introduced: a pressure adjustment (PA) one (Lindzen and Nigam, 1987) and a downward momentum mixing (DMM) one (Wallace et al., 1989; Hayes et al., 1989). According to the former, the presence of a warm SST patch induces a local low in the sea level pressure, which in turns induces surface convergence. This means that the convergence is enhanced over a local maximum of SST, where the magnitude of the SST gradient is, thus, very small. According to the latter mechanism, the increase in temperature while

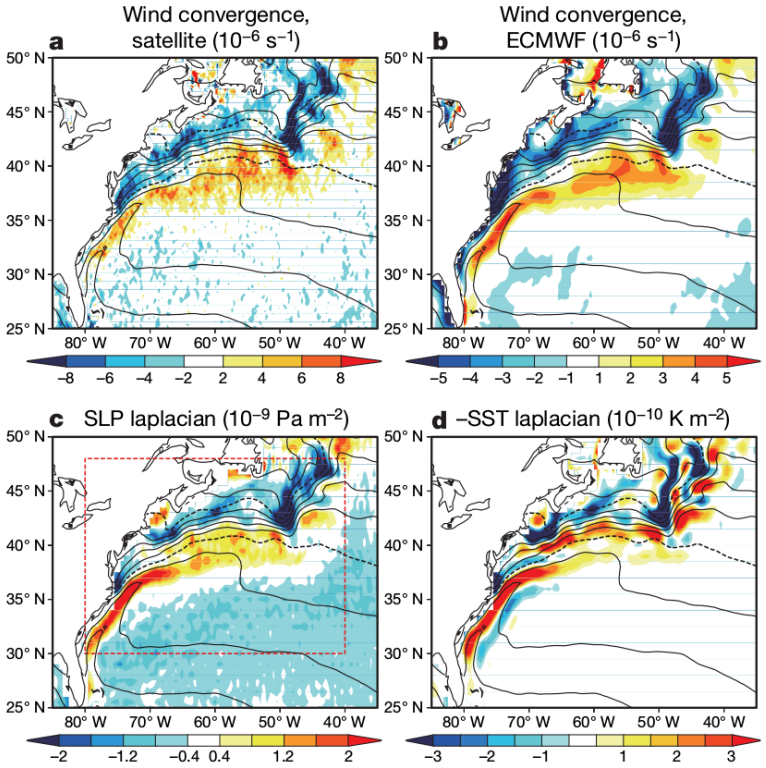

Figure 3.1: Annual climatologies of different variables: 10-m wind convergence in QuickSCAT satellite observations (a) and in ECMWF analysis (b); sea level pressure laplacian (c) and sign-reversed SST laplacian (d) from the ECMWF analysis. SST contours are shown as black lines (every 2° C) and the 10° C and 20° C contours are shown as dashed lines. The spatial correlation between the SST laplacian and the surface wind convergence is visible by inspection. Adapted from Minobe et al. (2008).

crossing a SST gradient from cold to warm reduces the air column stability and enhances the vertical mixing. This means that, on the warmer side of the front, the surface wind is accelerated by downward momentum mixing. Spall (2007) actually points out that at midlatitudes, in a relatively high wind regime, $O(10\ \text{m s}^{-1})$, also the Coriolis term plays a significant role in accelerating (decelerating) the surface across-front momentum while overcoming a cold-to-warm (warm-to-cold) SST front. In particular, by running some primitive equation idealized coupled ocean-atmosphere numerical simulations, he is able to show that in the leeside of a SST front there is a net transfer of momentum between the across-front and the along-front components through the Coriolis term. This is due to the fact that the momentum balance far from the front is between the Coriolis term and the turbulent drag term. At the rapid change of the turbulent term at the SST front

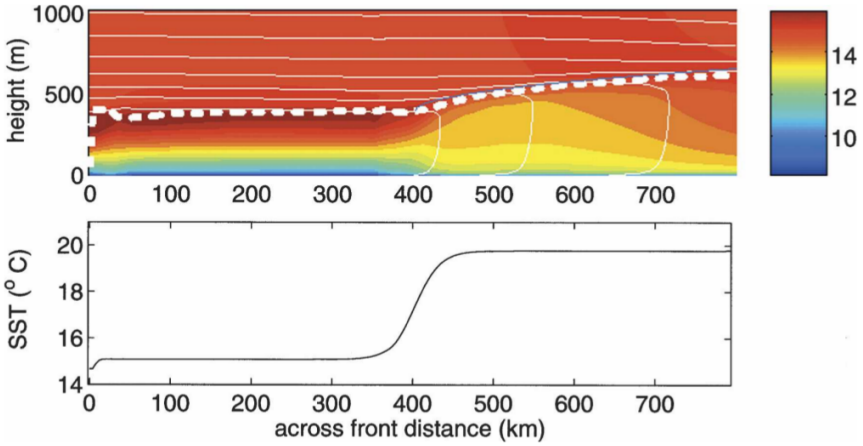

Figure 3.2: A zonal section of zonal wind is shown in the upper panel as color shading [m s^{-1}], together with potential temperature contours (white thin lines each 1 K) and the top of the planetary boundary layer as a thick dashed white line. Wind is blowing from cold to warm SST (from left to right), shown in the lower panel, and the effect of the enhanced vertical mixing after crossing the SST front can be noticed from the fact the wind velocity is more homogenized in the vertical direction. Adapted from Spall (2007).

(that controls the DMM mechanism of the above), it corresponds a slower change of the Coriolis term, which results in a net transfer between the two momentum components, typical of systems with background rotation. Figure 3.2 shows the simple geometrical setup in which Spall (2007) performs its numerical analysis. A comprehensive review of the observations and numerical simulations that explain such mechanisms can be found in Small et al. (2008).

Examples of observational studies are Liu et al. (2000); Chelton et al. (2001), that investigate the impact of tropical instability waves in the SST on surface winds; Song et al. (2006); Minobe et al. (2008); O'Neill et al. (2010), that study midlatitude western current systems; Li and Carbone (2012), that study convective rainfalls over the western Pacific warm pool. All the above studies generally focus on structures with typical length scales of O(100 km) and time scales of O(months). On the same climatological time scales, Takatama et al. (2012, 2015) introduce some analytical diagnostics that help to discriminate the contribution of the two mechanisms outlined above, PA and DMM, in the control of the surface layer vertically integrated wind magnitude, wind convergence and wind curl. At shorter time scales, idealized numerical studies focus on the understanding of the basic mechanisms. For example, De Szoeke and Bretherton (2004) study the DMM mechanism in a near-equatorial setup, while Skyllingstad et al. (2007) do it in a midlatitudes one. They both find that the DMM mechanism acts over

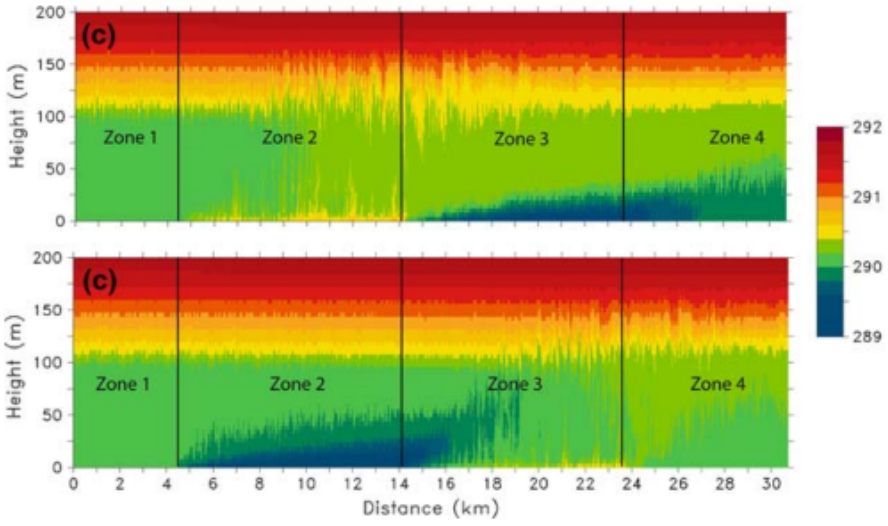

Figure 3.3: Steady state vertical sections of the potential temperature of the LES simulations from Skyllingstad et al. (2007). The upper panel shows the warm to cold case (WC) and the lower panel shows the CW one. Adapted from Skyllingstad et al. (2007).

length scales of the same order of the length scale of the front, $O(10$ km), with negligible changes in the pressure gradient term.

In particular, Skyllingstad et al. (2007) perform LES numerical simulations in an idealized setup to study the basic physics of the flow controlling the marine atmospheric boundary layer (MABL) over a simple SST front. They study the flow in two simplified settings in which a neutrally stable MABL first transitions over a warm zone and then over a cold one (case WC) and the opposite (case CW). The initial temperature is 17°C, the temperature of the cold and the warm patches are respectively 15°C and 19°C. Vertical sections of the potential temperature of the MABL are shown in figure 3.3 both for the WC and the CW cases. In the upper panel, that shows the WC case, it is clear how the enhanced vertical turbulent mixing makes the MABL more homogeneous and then, over the cold patch, an internal boundary layer (IBL) forms, where the air column is strongly stratified and there is little vertical velocity. As for the CW case, the vertical section of the lower panel shows how the strong convective turbulence that develops over the warm area destroys the IBL formed over the cold one.

The mechanisms controlling the SST-wind relationship introduced above, DDM and PA, have not been extensively studied in numerical simulations with a realistic midlatitudes setup leading to a HPE. Toy and Johnson (2014) argue that the presence of a SST gradient of the order $O(1$ K/100 km) near Taiwan is crucially important to determine the location of the convergence line that triggers the heavy-rain-producing deep convection, but information on the influence of SST on convergence patterns at smaller scales have not been given yet. By means of numerical simulations run with a primitive equation

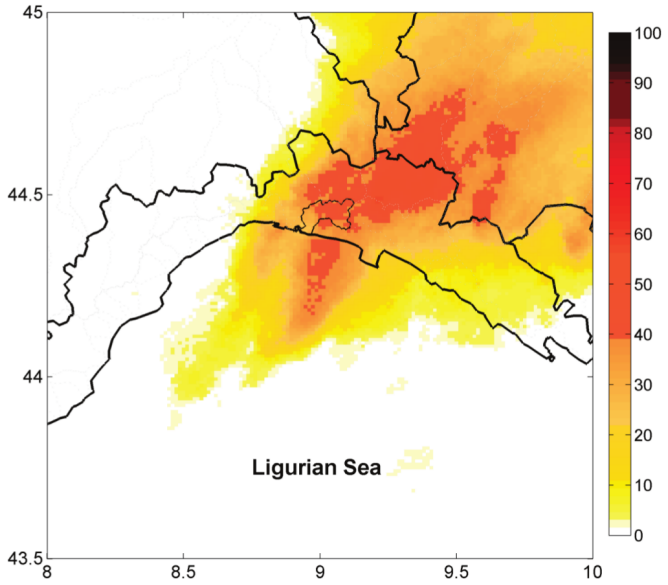

Figure 3.4: The percentage of the day in which the rain rate was larger than 1 mm h^{-1}, as observed by the Italian radar network on the 9 October 2014, is shown. The thin black line denotes the Bisagno catchment (Fiori et al., 2017).

atmospheric model, the goal of the present work is to investigate the importance of the mechanisms controlling the SST-wind relationship in a realistic setup, with structures characterized by O(hours) time scales and $O(1-10$ km) length scales. In particular, a pre-HPE midlatitudes setup is chosen and starting from a realistic simulation of the 9 October 2014 Genoa HPE (Faccini et al., 2015; Silvestro et al., 2015; Cassola et al., 2016; Fiori et al., 2017; Lagasio et al., 2017), the SST forcing field is artificially modified to explore the sensitivity of the above mentioned SST-wind mechanisms on the spatial length scales and variance of the SST itself. Figure 3.4 shows the observed percentage of the day in which the rainfall rate was larger than 1 mm h^{-1} during the event just mentioned. The typical V-shape of such structures can be noticed. Section 3.2 describes the numerical simulation setup, with the detailed description of the SST forcing fields. Section 3.3 is devoted to a short description of the HPE under study, while in sections 3.4 and 3.5 the spatial statistics for the variables of interest are shown for the various simulations. Discussion and conclusions are provided in section 3.6.

3.2 Numerical simulations

Model setup

The Weather Research and Forecast (WRF) model (Skamarock et al., 2008) solves the non-hydrostatic fully compressible primitive equations on a Arakawa-C grid with mass-based terrain following coordinates. In this work, it is used with its Advanced Research WRF (ARW) dynamical core, version 3.6.1, in the following two configurations. The former one is used in a preparatory simulation and is made of three two-way nested domains, shown in the panel (a) of figure 3.5. This simulation is run to downscale the European Center for Medium-Range Weather Forecasts - Integrated Forecast System (ECMWF-IFS) numerical weather prediction model product (Simmons et al., 1989), used to initialize and force the simulations at the boundaries, from its native horizontal resolution of 0.125° to the resolution of interest, 1.4 km. In the latter configuration, a series of simulations is run using the inner domain of the previous simulation (d03) only, initialized and forced at the boundaries with the preparatory output files of the intermediate domain (d02), appropriately re-gridded with the NDOWN tool (Skamarock et al., 2008). In the preparatory simulation, the Euro-Cordex domain (Jacob et al., 2014) is used as the largest computational domain, d01, with a grid spacing of 12 km in the horizontal. The intermediate domain, d02, has a grid spacing of 4 km and covers an area that roughly spans the ranges $[-10°, 35°]$ longitude and $[25°, 50°]$ latitude. The inner domain, d03, shown in the right panel of figure 3.5, is defined to cover the entire Ligurian sea with a resolution of 1.4 km. The numerical grid has 84 vertical levels with a finer resolution in the lower atmosphere. The advantages of having such a high number of vertical levels, in terms of better precipitation volume and spatial distribution, can be found in Fiori et al. (2014). The cylindrical equidistant projection with a rotated North Pole is used.

The physical parameterizations activated in all the simulations, that are chosen according to previous sensitivity studies in the same location and for the same kind of meteorological event (Fiori et al., 2014), are summarized in table 3.1. In Fiori et al. (2014) two different microphysics schemes (WRF Single Moment - 6 class, WSM6, and Thomson) and three different convection schemes (explicit, Kain-Fritsch and Betts-Miller-Janjic) were tested in a setup similar to the one considered here. In terms of convective parameterization, the Betts-Miller-Janjic scheme has an adjustment procedure to a climatological sounding, which, thus, does not take into account the current dynamical conditions. While the Kain-Fritsch scheme rearranges the mass in the air column following a CAPE-consuming procedure. Among its drawbacks, there is the possibility to overestimate the post-convective stratiform precipitation due to unrealistically saturated deep layers (Fiori et al., 2014). Not surprisingly, it is found that both the Betts-Miller-Janjic and the Kain-Fritsch underperform the runs with explicit convection, which is the option chosen in the current work. As for the microphysics, Fiori et al. (2014) found that the Thomson scheme performs slightly better than the WSM6, but because of technical issues on the high performance computer cluster, the WSM6 scheme was chosen instead of the Thomson one, since they are both suitable for high

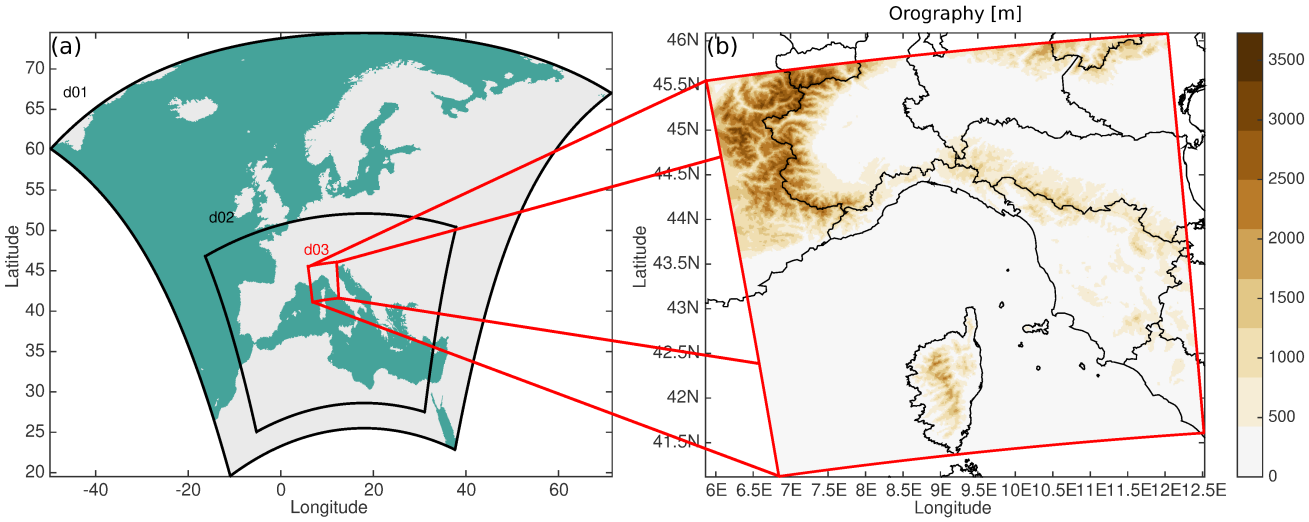

Figure 3.5: (a): The three domains of the preparatory simulation, d01, d02, d03 with horizontal grid spacing $\Delta x = 12$ km, 4 km and 1.4 km respectively. (b): The single domain used in the simulations of interest (CNTRL, ANML_HALF, ANML_DOUBLE, SM1, SM2, SM4, SM8, SM16, SM32, SM64), which corresponds to d03 of the preparatory simulation. The orography is shown in false colors.

resolution simulations.

The choice for the vertical diffusion parameterization is a three dimensional turbulent kinetic energy (TKE) closure scheme that mixes the full fields and not only the perturbations. This choice is motivated by the fact that the innermost domain grid spacing, equal to 1.4 km, almost falls in the so-called terra incognita range for turbulence modeling (Wyngaard, 2004). Such a range is generally considered to be between 100 m - 1 km and it is defined as the range where neither the LES nor the mesoscale turbulent parameterizations were developed for. In particular, it is defined as the range where the ratio l/Δ is order 1, where l is the turbulent energy containing lengthscale and Δ is the scale of the spatial filter used on the equations of motion, i.e. the scale of the resolved processes (Wyngaard, 2004; Fiori et al., 2010). Since the scale of mesoscale models is generally 10 km (or above) and the scale of LES is 100 m or below (Fiori et al., 2010), one could even argue that the terra incognita range is between 100 m and 10 km and, thus, the value of 1.4 km used in the present simulations would explicitly fall in the critical range. Previous studies for idealized (Fiori et al., 2010) and real case studies (Ricard et al., 2013; Fiori et al., 2017) suggest that a fully three-dimensional TKE approach is preferrable to the ones based on boundary layer approximation, where the planetary boundary layer scheme is taking care of the vertical mixing.

Table 3.1: Options chosen for the physical parameterizations in all the simulations.

Process	Scheme	Reference
Microphysics	WRF Single-Moment 6-Class	Hong and Lim (2006)
Planetary boundary layer	Mellor-Yamada Nakanishi Niino lev 2.5	Nakanishi and Niino (2009)
Cumulus (on d01 only)	Tiedtke	Tiedtke (1989)
Longwave radiation	RRTM	Mlawer et al. (1997)
Shortwave radiation	Goddart	Chou and Suarez (1999)
Land surface	5-layer thermal diffusion	Dudhia (1996)
Surface layer	revised MM5 similarity	Beljaars (1994)

SST forcing fields

All the simulations of the present work have the same atmospheric boundary conditions, obtained from the d02 output files of the preparatory simulation described above, and differ from one another only for the time independent SST forcing. They run for four days, from 0000 UTC 6 October 2014 to 0000 UTC 10 October 2014. The reference SST forcing field, used in the CNTRL simulation, is obtained from an oceanic primitive equation model spinup. The Regional Ocean Modeling System (ROMS) in its Coastal and Regional Ocean COmmunity (CROCO) version (Penven et al., 2006; Debreu et al., 2012) is run for three weeks preceding the beginning of the current simulation (from 0000 UTC 15 September 2014 to 0000 UTC 06 October 2014), forced at the upper boundary with the same ECMWF-IFS product used to force the atmosphere and at the lateral boundaries by the Mediterranean Forecasting System (MFS) product (Oddo et al., 2009), which also provides the initial oceanic conditions. All the details about the ocean model setup can be found in chapter 4, where the role of the coupled ocean dynamics and, in particular, of the thermal oceanic vertical structure is studied. This spinup simulation is run in order to obtain a fine scale SST field, on the same grid of the WRF model, to be used a lower boundary condition in the CNTRL simulation.

Given a local cartesian frame of reference $\{x\hat{\mathbf{i}}, y\hat{\mathbf{j}}, z\hat{\mathbf{k}}\}$, with $\hat{\mathbf{k}}$ against the local effective gravitational acceleration vector, let $\mathrm{SST}_0(x, y)$ be the SST field of the last instant of the oceanic spinup simulation mentioned above, that corresponds to 0000 UTC 6 October 2014. This is the forcing of the CNTRL simulation. Denoting with $|\mathrm{sea}|$ the area of the fraction of the numerical domain covered by the sea, the SST_0 horizontal average value is

$$\overline{\mathrm{SST}} = \frac{1}{|\mathrm{sea}|} \iint_{\mathrm{sea}} \mathrm{d}x\mathrm{d}y\, \mathrm{SST}_0(x, y) = 22.58°\mathrm{C}. \tag{3.1}$$

In the simulation UNIF, the SST is prescribed as a homogeneous and constant field equal to $\overline{\mathrm{SST}}$.

In order to explore the effects of changing the horizontal SST gradients without changing its spatial mean value, two simulations are run with the SST field obtained as follows. Take the anomaly of the $\mathrm{SST}_0(x, y)$ with respect to its horizontal average,

$\mathrm{SST}'(x,y) = \mathrm{SST}_0(x,y) - \overline{\mathrm{SST}}$, then the forcing fields of the simulations of the series ANML_α are obtained as

$$\mathrm{SST}_\alpha(x,y) = \overline{\mathrm{SST}} + \alpha \cdot \mathrm{SST}'(x,y). \tag{3.2}$$

The simulations ANML_HALF and ANML_DOUBLE have $\alpha = 0.5$ and $\alpha = 2$, respectively, while CNTRL would have $\alpha = 1$ and UNIF would have $\alpha = 0$. With the above definition, it is clear that the role of the factor α is to amplify (or attenuate, if smaller than 1) the horizontal SST gradients and the SST standard deviation pointwise, withouth changing its average value.

In the series SMϕ, instead, the simulations have smoothed SST fields, obtained by convoluting over the sea the reference field $\mathrm{SST}_0(x,y)$ with a gaussian-like filter defined as

$$G_\phi(x,y) = \begin{cases} \exp\left(-\dfrac{x^2+y^2}{2\phi^2}\right) & \text{for } (x^2+y^2)^{1/2} < 3\phi, \\ 0 & \text{otherwise.} \end{cases} \tag{3.3}$$

In this way, the forcing SST fields are explicitly

$$\mathrm{SST}_\phi(x,y) = G_\phi * \mathrm{SST}_0 = \frac{1}{A(x,y)} \iint_{\mathrm{sea}} \mathrm{d}x'\mathrm{d}y'\, G_\phi(x-x', y-y')\mathrm{SST}_0(x,y), \tag{3.4}$$

with the normalization factor

$$A(x,y) = \iint_{\mathrm{sea}} \mathrm{d}x'\mathrm{d}y'\, G_\phi(x-x', y-y'). \tag{3.5}$$

The length ϕ is the standard deviation of the filter and appears in the name of the simulation expressed in km. It is well known that with a gaussian low-pass filter, its standard deviation is related to the cutoff length imposed by the filter itself. In particular, it is easy to show with classical Fourier transform arguments (Arfken and Weber, 2006) that the cutoff wavenumber, which determines the minimum resolved length scale in the filtered field, is inversely proportional to the standard deviation of the gaussian filter in the physical space. For example, by choosing as a cutoff value the wavenumber that corresponds to 3 standard deviation in the spectral domain (where the gaussian function is roughly 1% of its value in the origin), the minimum resolved length is roughly twice the standard deviation of the gaussian filter, ϕ. Thus, to compare the various simulations of this work, it is useful to define the minimum resolved length μ as twice the standard deviation of the filter, for the simulations with smoothed SST fields, and as equal to the grid spacing for all the others. In symbols,

$$\mu = \begin{cases} 2\phi & \text{simulations: SM}\phi, \\ \Delta x & \text{simulations: CNTRL, ANML\_}\alpha, \end{cases} \tag{3.6}$$

where Δx is the numerical domain grid spacing. Note that the UNIF simulation would have $\mu \to +\infty$ because there are no structures in its forcing SST field.

Table 3.2: Summary of the SST forcing fields of the various simulations. $\mathrm{SST}_0(x,y)$ is the fine scale reference field, $\overline{\mathrm{SST}}$ its horizontal average value as in equation (3.1), $\mathrm{SST}'(x,y)$ its departure from the average value and $*$ denotes the convolution product defined in equation (3.4).

Name of the simulation	SST forcing
CNTRL	$\mathrm{SST}_0(x,y) = \overline{\mathrm{SST}} + \mathrm{SST}'(x,y)$
UNIF	$\overline{\mathrm{SST}}$
ANML_HALF	$\overline{\mathrm{SST}} + 0.5 \cdot \mathrm{SST}'(x,y)$
ANML_DOUBLE	$\overline{\mathrm{SST}} + 2 \cdot \mathrm{SST}'(x,y)$
SM1	$G_1 * \mathrm{SST}_0(x,y)$
SM2	$G_2 * \mathrm{SST}_0(x,y)$
SM4	$G_4 * \mathrm{SST}_0(x,y)$
SM8	$G_8 * \mathrm{SST}_0(x,y)$
SM16	$G_{16} * \mathrm{SST}_0(x,y)$
SM32	$G_{32} * \mathrm{SST}_0(x,y)$
SM64	$G_{64} * \mathrm{SST}_0(x,y)$

It is interesting to underline that in the series ANML_α, the minimum resolved length of the SST is unchanged and the gradients are modified pointwise analytically (they are increased or reduced depending on whether α is greater or less than one) with respect to CNTRL. While in the series SMϕ, as the filter gets larger, the smoothing of the forcing field induces both a reduction of the variance of the SST and an increase in the minumum resolved length, with a net decrease in the gradient pointwise, but no changes in the average mean value of the SST. A summary of the SST forcing fields used in the simulations is given in table 3.2.

3.3 The simulated event

A detailed description of the 9 October 2014 HPE is given by Fiori et al. (2017); Lagasio et al. (2017). At the synoptic scales, this event was characterized by an upper-level trough roughly centered over Ireland, which caused a low-level wind to blow from the Mediterranean sea, channeled between the Corsica island and mainland Italy, towards the Liguria region (Cassola et al., 2016; Fiori et al., 2017). The encounter of the warm moist low-level jet with the colder and drier continental air spilling over the sea through the Turchino pass, in the Ligurian Appennines, is analyzed by means of very high resolution numerical simulations by Fiori et al. (2017). They find that the colder air mass acts as a virtual orographic barrier for the moist low-level jet, which, by reaching its level of free convection, produces the heavy convective rain.

It is important to underline that in the present work the goal is not to improve the forecast of such systems trying to match as much as possible the simulations with the observations, but to eventually study the sensitivity of the precipitation to changes in

the SST spatial structure down to the km scale, through the well-known mechanisms controlling the mesoscale SST-wind relationship (Small et al., 2008). Thus, the UNIF simulation, despite its known differences with respect to the observations (not shown), is taken as reference case in a sense that is clarified in what follows. These differences, in particular, are mainly in the position of the convergence line leading to the rainfall on the 9 October and in the total rain amount. In fact, the simulations of this work do not capture the convergence line that was observed over the sea, off the coasts in front of the city of Genoa, but they produce the convective rain thanks to the orographic lifting provided by the Apennines mountains (see the right panel of figure 3.7 for the UNIF simulation). As for the total volume of rain, in the simulations it is underestimated with respect to the observations. Both issues improve by initializing the simulations closer to the HPE. Other works (Cassola et al., 2016; Fiori et al., 2017) and other unpublished simulations run by the authors show that the proper dynamical stucture of the convergence line over the sea and a more realistic total rain volume are simulated by initializing the model no more than 36 hours before the convective rain of the 9 October.

An overview of the general behavior of all the simulations is given by figure 3.6, where the domain integral of the hourly rain rate is shown as a function of time for some of the simulations considered, namely CNTRL, UNIF, ANML_HALF, ANML_DOUBLE. The first high peak during the morning of the 7 October corresponds to a convective rain organized along two convergence lines over the sea, off the coasts of southern France and western Liguria. By looking at different simulations, the height of this peak increases following this order: ANML_DOUBLE , CNTRL, ANML_HALF, UNIF because the total amount of rain volume is controlled by the SST of the sea area nearby the event (Pastor et al., 2001; Lebeaupin et al., 2006), and in such area the average SST in increasingly warmer following the same order of simulations. On the 8 October, a very weak convergence line is formed along the coasts of Liguria (not shown), but it does not produce much rain. While on the 9 October, the heavy-rain-producing MCS discharges its rain volume over the land, because of the orographic uplifting provided by the Apennines.

The spatial structures of the rainfall on the 7 and 9 October from the UNIF simulation are shown in figure 3.7. The two convergence lines that develop on the 7 October correspond to the two intense rainfall patches (shown in red) between $[6.5°, 8°]$ longitude and $[42.5°, 42.8°]$ latitude and $[8°, 8.7°]$ longitude and $[43.2°, 43.5°]$ latitude shown in the left panel. While the fact that the convection on the 9 October is triggered by the orography is evident in the right panel of the same figure, where the majority of the intense rain is shown to fall along the northern Appenines.

3.4 Analysis

Metrics

In the context of tropical instability waves, Liu et al. (2000) describe how the two main mechanisms controlling the SST-wind relationship, PA and DMM, can be distinguished

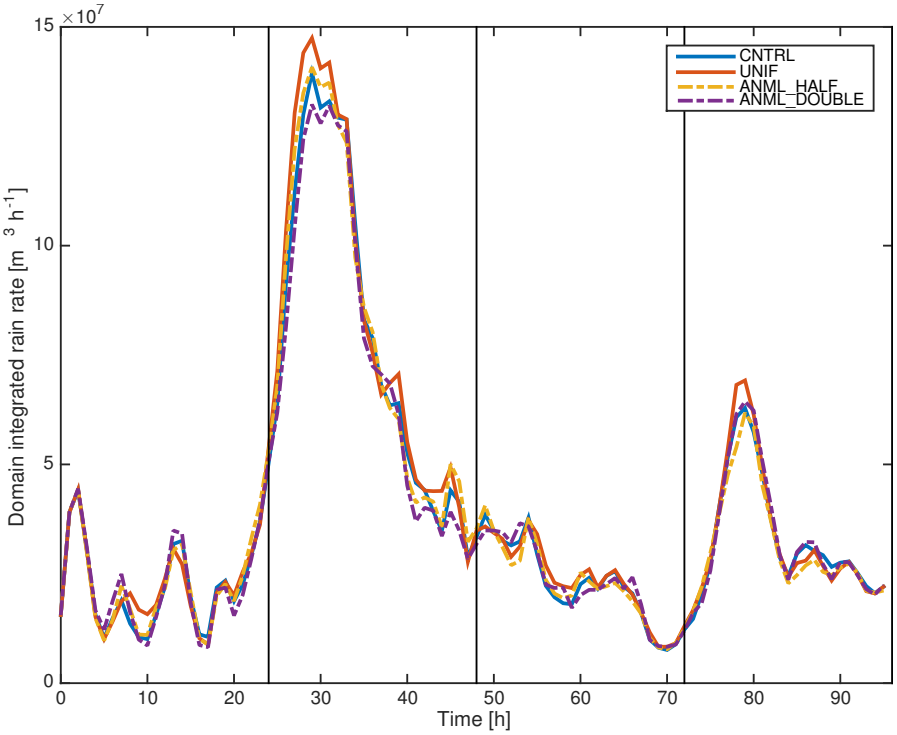

Figure 3.6: Spatial integral over the entire domain of the simulation of the hourly rain rate as a function of time from initialization (0000 UTC 6 October 2014). Data from different simulations are shown (CNTRL, UNIF, ANML_HALF and ANML_DOUBLE) and the vertical black lines denote the midnight. The highest peak, in the morning of the 7 October, i.e. around 30 hours after initialization, corresponds to a heavy rainfall event over the sea, while the second peak in the morning of the 9 October (80 hours from initialization) corresponds to the HPE that hit the city of Genoa.

from each other by looking at the phase difference between SST and wind speed signals. When the PA mechanism dominates, the wind speed is 90° out of phase with respect to the SST, while it is in phase with it when the DMM mechanism prevails. This, in turns, implies that when the PA mechanism dominates, surface wind convergence happens in correspondence of local maxima of SST, while when the DMM one dominates, surface wind convergence occurs at the SST fronts. Here, a similar idea is applied for time averaged two dimensional spatial fields. In particular, the analysis of the spatial correlation coefficients between some specific time averaged variables, defined below, enables to infer the relative importance of the PA and DMM mechanisms over O(hours) time scales and in the realistic midlatitudes pre-HPE setting considered. Let us discuss why the process involving the Coriolis term highlighted by Spall (2007) is neglected here. As mentioned in the introduction, while the turbulent stress term is known to react on lenght scales of the same order of the SST front scales, the Coriolis one needs

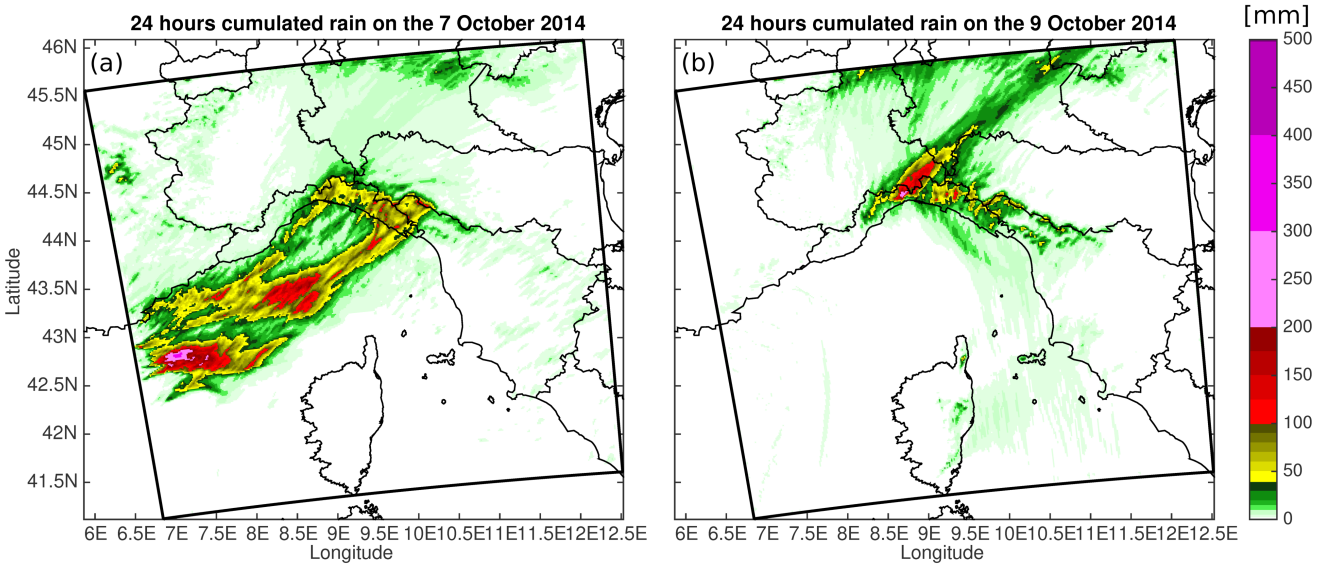

Figure 3.7: The rain cumulated over 24 hours on the 7 (a) and 9 October (b) is shown with the data of the UNIF simulation.

more time to adjust. In a midlatitudes setup with $f \sim 10^{-4}$ rad s^{-1} and with typical wind speed $U \sim 10$ m s^{-1}, the Coriolis term is relevant for the SST-wind relationship on $Uf^{-1} \sim 100$ km scales. This means that in the present setup, where there is not a clear SST front as in Spall (2007), but the SST structure contains eddies and filaments on the $O(1-10$ km) scales, the Coriolis term dominated mechanism proposed by Spall (2007) does not have time to significantly relate the surface wind with the SST. The analysis of the present section, thus, only focuses on the PA and DMM mechanisms.

Let the time average run between the instants t_0 and $t_0 + \tau$, with $\tau > 0$ and let capital letters denote time averaged quantities, such as:

1. the 10 meters wind magnitude

$$\mathcal{U}_{10}(x,y) = \frac{1}{\tau}\int_{t_0}^{t_0+\tau} \mathrm{d}t\, |\mathbf{u}_{10}(x,y,t)|; \tag{3.7}$$

2. the 10 meters wind horizontal convergence

$$\mathcal{C}_{10}(x,y) = \frac{1}{\tau}\int_{t_0}^{t_0+\tau} \mathrm{d}t\, \left[-\boldsymbol{\nabla}\cdot\mathbf{u}_{10}(x,y,t)\right]; \tag{3.8}$$

3. the downwind SST gradient

$$\mathcal{D}_{10}(x,y) = \frac{1}{\tau}\int_{t_0}^{t_0+\tau} \mathrm{d}t\, \left[\hat{\mathbf{u}}_{10}(x,y,t)\cdot\boldsymbol{\nabla}\mathrm{SST}(x,y)\right]; \tag{3.9}$$

where $\mathbf{u}_{10}(x,y,t) = u_{10}(x,y,t)\hat{\mathbf{i}} + v_{10}(x,y,t)\hat{\mathbf{j}}$ is the instantaneous 10 meters wind vector decomposed on the local cartesian frame of reference, $|\mathbf{u}_{10}(x,y,t)|$ its magnitude and $\hat{\mathbf{u}}_{10}(x,y,t)$ its corresponding unit vector. In addition, the $\mathrm{SST}(x,y)$ field itself and its laplacian $\mathrm{LSST}(x,y) = \nabla^2\mathrm{SST}$ are considered, but since they are constant, they need no time average.

In order to remove the large-scale structures, that are imposed by the forcing at the boundaries, the time averaged fields defined above taken from the UNIF simulation, which are controlled by the dynamics with zero SST gradients within the domain, are subtracted from the time averaged fields of the other simulations. This operation is denoted with a Δ, so that, for example, for a given simulation, $\Delta\mathcal{U}_{10}$ is the difference between the time averaged 10 meters wind magnitude calculated from the simulation considered and the same time averaged field obtained from the UNIF simulation; namely, for the CNTRL simulation,

$$\Delta\mathcal{U}_{10}^{\mathrm{CNTRL}} = \mathcal{U}_{10}^{\mathrm{CNTRL}} - \mathcal{U}_{10}^{\mathrm{UNIF}}. \tag{3.10}$$

Spatial statistics

Given a time independent field $q(x,y)$ and a region Ω with area $|\Omega| = \iint_\Omega \mathrm{d}x\mathrm{d}y$, the spatial mean and the variance of $q(x,y)$ are

$$\overline{q} = \frac{1}{|\Omega|}\iint_\Omega \mathrm{d}x\mathrm{d}y\, q(x,y), \tag{3.11}$$

$$\sigma_q^2 = \frac{1}{|\Omega|}\iint_\Omega \mathrm{d}x\mathrm{d}y\, [q(x,y) - \overline{q}]^2, \tag{3.12}$$

respectively. After defining the isotropic autocorrelation function for the field $q(x,y)$ as

$$R_q(r) = \frac{1}{2\pi}\int_0^{2\pi} \mathrm{d}\theta\, R_q(r\cos\theta, r\sin\theta), \text{ with} \tag{3.13}$$

$$R_q(\xi,\eta) = \frac{1}{\sigma_q^2|\Omega|}\iint_\Omega \mathrm{d}x\mathrm{d}y\, [q(x,y) - \overline{q}][q(x+\xi, y+\eta) - \overline{q}]$$

and with the usual change of variables to go from cartesian coordinates $\{\xi,\eta\}$ to polar coordinates $\{r,\theta\}$, the isotropic autocorrelation length λ_q can be defined as the distance for which the autocorrelation function decays of a factor e, namely

$$\lambda_q \quad \text{satisfies} \quad R_q(\lambda_q) = \mathrm{e}^{-1}. \tag{3.14}$$

This gives a measure of the typical size of the structures in the field $q(x,y)$ and can be used to find a simple estimate of its effective number of spatial degrees of freedom (dof), N^*. Following Bretherton et al. (1999), for a two-dimensional gridded field with no large-scale structure, N^* can be found as follow. Let $|\Omega|$ be the area of the region considered. Once a measure of the autocorrelation length λ_q is known, the typical size of the autocorrelated stuctures in the field is simply λ_q^2. If this value is larger than the

grid cell area, it means that neighbouring values of $q(x, y)$ are not independent from one another and thus the effective number of dof is smaller than the number of gridpoints. A simple estimate of N^* is then

$$N^* = \frac{|\Omega|}{\lambda_q^2}. \tag{3.15}$$

This number is particularly important when the statistical significance of the spatial correlation coefficient needs to be evaluated. Given two time independent fields, $a(x, y)$ and $b(x, y)$ with spatial averages $\overline{a}$, $\overline{b}$ and variances σ_a^2, σ_b^2 respectively, their spatial correlation coefficient over the region Ω is defined as

$$\rho[a, b] = \frac{1}{\sigma_a \sigma_b |\Omega|} \iint_\Omega \mathrm{d}x\mathrm{d}y \, [a(x, y) - \overline{a}][b(x, y) - \overline{b}]. \tag{3.16}$$

To test its statistical significance, a 95% confidence interval for the null hypothesis of zero correlation between the two fields $a(x, y)$ and $b(x, y)$ is calculated as follows. Considering a high enough N^*, the distribution of the null correlation coefficient is known to be a gaussian with zero mean and standard deviation $\sigma_0 = 1/\sqrt{N^*}$ (Press et al., 1992). The amplitude of the 95% confidence interval is then easily found as $1.96\sigma_0$ and if the correlation coefficient falls outside this confidence interval is significant at the 95% level. To make sure that the null correlation coefficient distribution is gaussian, its first four moments were estimated by reshuffling the two fields $a(x, y)$ and $b(x, y)$, previously subsampled over a grid with horizontal spacing equal to λ, which is the shortest autocorrelation length between the two λ_a and λ_b. For a sufficiently high number of reshuffling (5000), the sample moments were found to converge to those of a normal distribution with zero mean and standard deviation σ_0 (not shown).

Note that, by definition, the autocorrelation function $R_q(r)$ is equal to one at zero lag, as well as the spatial correlation coefficient of a field with itself. In symbols, $R_q(0) = \rho[q, q] = 1$, so that the above definitions are all consistent with one another. The extension of the domain of the current simulations is so small that the distorsion of the grid cells due to the cylindrical projection and the curvature of the earth are neglected while calculating all the above statistics. This is justified because it introduces relative errors of the order $O(10^{-3})$.

3.5 Results

The analysis of the spatial correlations of the variables defined in the previous section enables to infer the importance of the DMM and PA mechanisms at different time scales over the spatial structures determined by the various SST forcing fields considered. The effects on the precipitation, then, can be studied as a function of the controlling mechanism just mentioned.

Atmospheric response mechanisms

Starting from the 9 October 2014, which is the day of the HPE that hit the city of Genoa and it has no simulated deep convective activity over the sea, consider the time

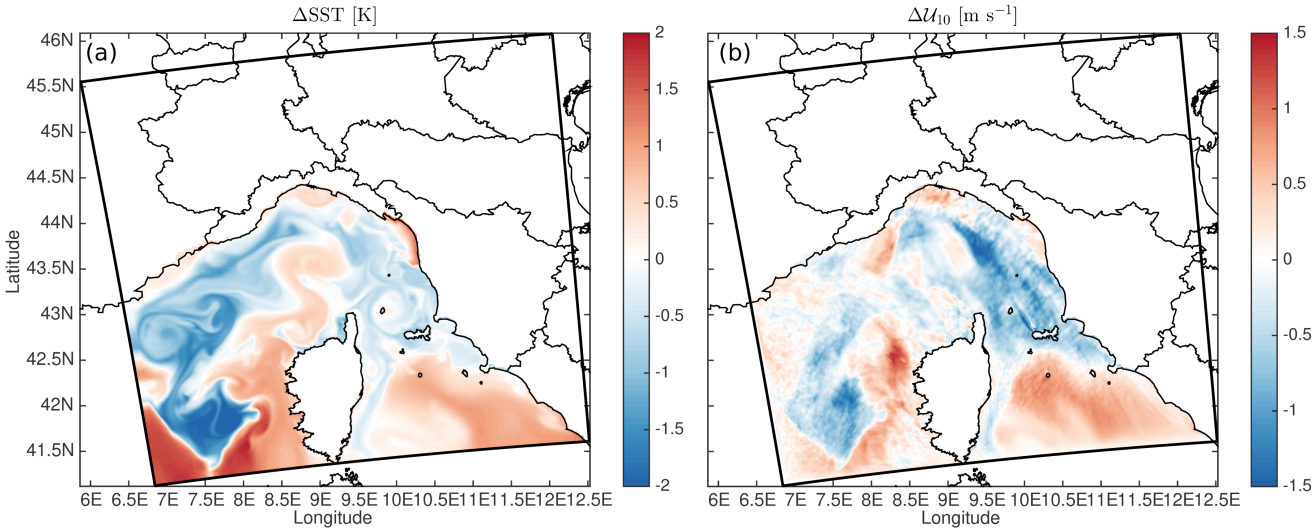

Figure 3.8: ΔSST (a) and $\Delta\mathcal{U}_{10}$ (b) of the CNTRL simulation calculated on the 9 October. The correspondence of the $O(10$ km) structures is quite remarkable.

average of the SST and the surface wind magnitude fields between 0000 UTC 9 October 2014 and 0000 UTC 10 October 2014. In the left panel of figure 3.8, as an example, the ΔSST of the CNTRL simulation highlights the presence of spatial features on the scale of $O(1-10$ km), arranged in a complex eddy-containing structure. The SST anomalies with respect to the UNIF case can be as high as 2 K and the SST horizontal gradients can be of the order of 1 K / 10 km. In the right panel of the same figure, the $\Delta\mathcal{U}_{10}$ field from the same simulation is shown. Even if one can see that there is some variability on smaller spatial scales, compared to the ΔSST field of the left panel, it is remarkable how well the atmosphere can respond to the $O(1-10$ km) spatial structure of the SST forcing.

To quantify this, figure 3.9 shows the autocorrelation functions, as defined in equation (3.13), of the ΔSST (a) and $\Delta\mathcal{U}_{10}$ (b) fields for the CNTRL and SMϕ simulations. In the left panel, it is easy to see that the larger the width of the filter ϕ, the slower the decay of the autocorrelation function of the SST, as expected. This, following the definition of equation (3.14), gives in the CNTRL simulation an autocorrelation lenght $\lambda_{\mathrm{SST}} = 38$ km that reaches $\lambda_{\mathrm{SST}} = 140$ km in the simulation SM64. The right panel, instead, shows that for high values of ϕ, in particular for SM32 and SM64, the 10 meters wind magnitude field has at first a rapid decay at the short scales and then decreases at a slower rate. This is interpreted as a signature of the action of the three dimensional direct turbulent energy cascade in the marine boundary layer. In particular, when the SST forcing does not have small scale structure, the small scale structure in the wind field is randomly determined by the turbulence and thus the autocorrelation function has a sharp initial decay.

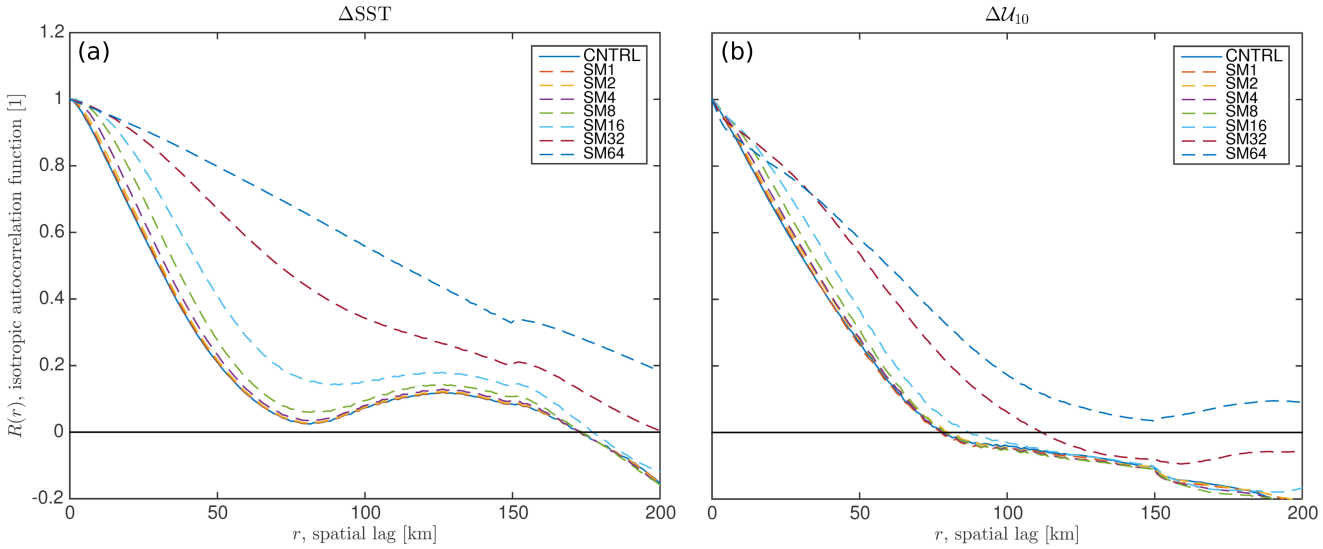

Figure 3.9: Autocorrelation functions, as in equation (3.13), of the ΔSST and $\Delta\mathcal{U}_{10}$ on the 9 October from the simulations listed in the legend.

The spatial correlation coefficients between ΔSST and $\Delta\mathcal{U}_{10}$ for all the simulations of interest, calculated as in equation (3.16) over the sea for the same time interval as before (the entire day of the 9 October), are shown in figure 3.10. The amplitude of the 95% confidence interval is shown in grey shading, indicating that all the correlation coefficients are statistically significant. For high values of minimum resolved length of the SST μ, the correlation coefficients decrease, suggesting again that the absence of small scale forcing in the SST leads to a more turbulence-dominated wind magnitude field, which is thus less correlated with the SST itself.

If one, then, looks at the same correlation coefficients between ΔSST and $\Delta\mathcal{U}_{10}$ averaged over different time intervals τ, it appears that for shorter τ the values of the ρ coefficients decrease. Figure 3.11 shows the $\langle\rho[\Delta\text{SST}, \Delta\mathcal{U}_{10}]\rangle$ calculated for different time average intervals, with data taken from 0000 UTC 7 October 2014 to 0000 UTC 10 October 2014. In particular, the coefficients shown in this figure are the arithmetic mean of the ρ coefficients calculated over all the possible time intervals of a certain duration τ in such time range (7-8-9 October). This operation is denoted with the $\langle\,\rangle$. The visible trend of decreasing correlation for shorter time average interval is simply explained considering that longer averages are able to smooth the short time scale turbulent wind fluctuations better. Despite the smaller values of the $\langle\rho[\Delta\text{SST}, \Delta\mathcal{U}_{10}]\rangle$ coefficients for shorter time averages, the fact that they are still statistically significant is indicative that the atmosphere, at least in the current model, is able to respond to mesoscale SST features over hourly time scales.

The statistically significant high spatial correlation coefficients $\rho[\Delta\text{SST}, \Delta\mathcal{U}_{10}]$ of figures 3.10 and 3.11 suggest that the surface atmospheric layer response to SST fronts is

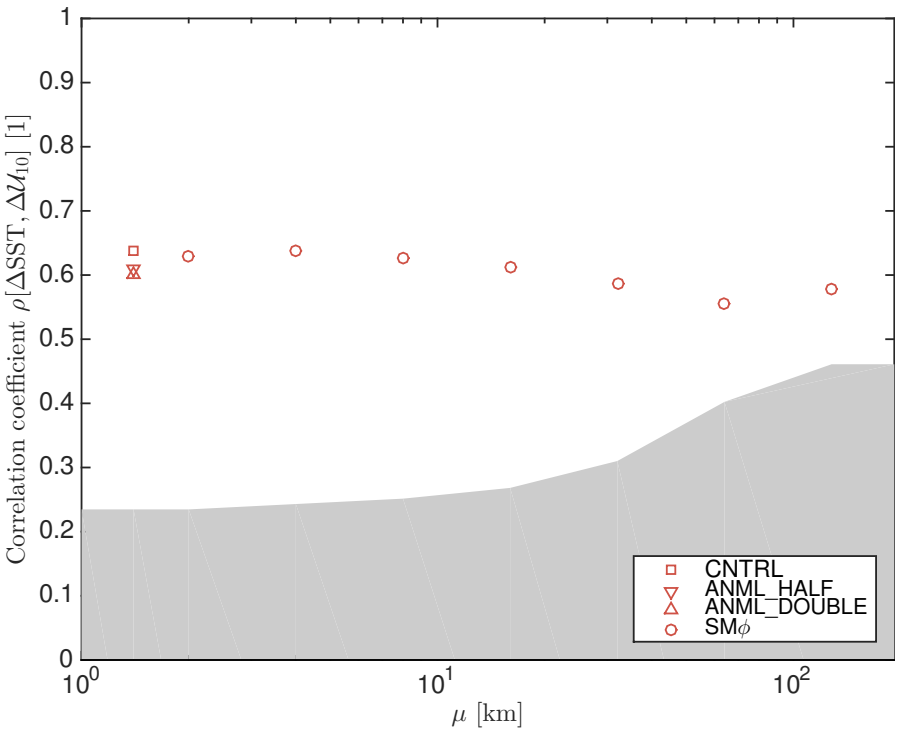

Figure 3.10: Spatial correlation coefficients between ΔSST and $\Delta\mathcal{U}_{10}$ averaged between 0000 UTC 9 October and 0000 UTC 10 October, as a function of the minimum resolved length μ defined in equation (3.6).

dominated by the DMM mechanism. In fact, the high spatial correlation between ΔSST and $\Delta\mathcal{U}_{10}$ corresponds to a small phase difference between the two fields, following Liu et al. (2000) approach. This interpretation is confirmed by the fact that $\rho[\Delta\mathcal{D}_{10}, \Delta\mathcal{C}_{10}]$ are higher (in absolute value) than $\rho[\Delta\text{LSST}, \Delta\mathcal{C}_{10}]$, as shown in figure 3.12 for a 24 hours time average, on the 9 October. The negative sign of the correlation between $\Delta\mathcal{D}_{10}$ and $\Delta\mathcal{C}_{10}$ of the upper panel of this figure captures the fact that when an air parcel crosses a SST front from warm to cold temperature, surface convergence is induced because the wind is decelerated on the downwind side of the front itself. Not only is the dependence of $\rho[\Delta\mathcal{D}_{10}, \Delta\mathcal{C}_{10}]$ on μ evident, but also on the amplification factor α of the ANML_α simulations. For smaller SST variance, as in ANML_HALF, the SST variations at the fronts are less sharp and, thus, $\Delta\mathcal{D}_{10}$ is weaker everywhere over the sea. In the limit of vanishing $\Delta\mathcal{D}_{10}$, i.e. uniform SST, it is evident that the surface wind convergence cannot be controlled by the SST structure, which is absent. In some sense, this also applies pointwise when some SST structure is present: in a small interval near $\Delta\mathcal{D}_{10} = 0$, nonzero values of $\Delta\mathcal{C}_{10}$ indicate that some other mechanism is generating surface convergence, with respect to the UNIF simulation. The fact that the two dimensional distribution of $(\Delta\mathcal{D}_{10}; \Delta\mathcal{C}_{10})$, as shown in figure 3.13, stretches along a line with a negative trend going from the ANML_HALF to the CNTRL, and then to

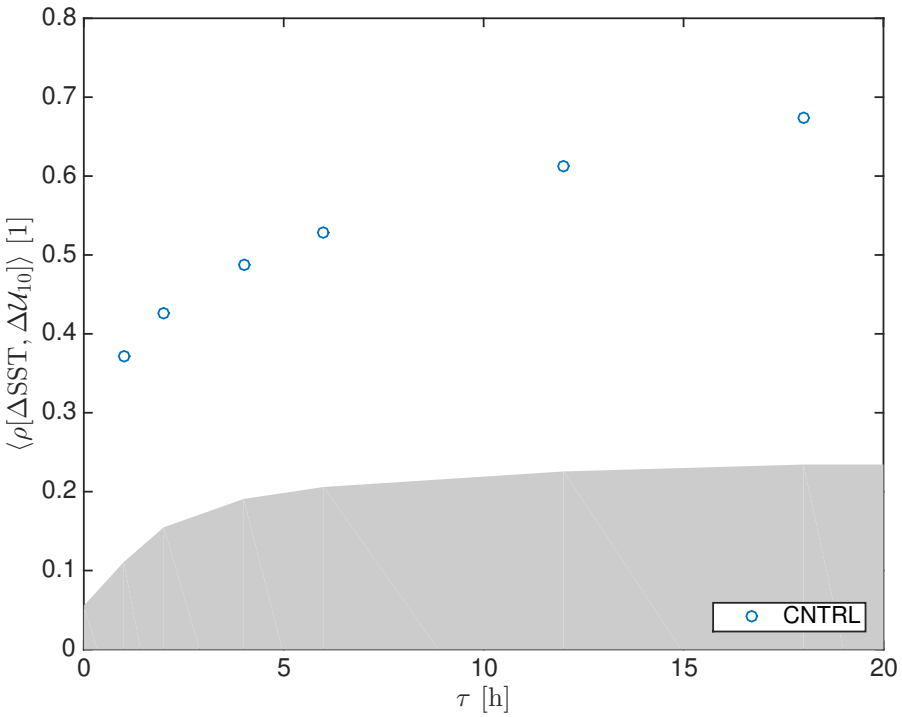

Figure 3.11: Arithmetic mean of the correlation coefficients $\rho[\Delta\mathrm{SST}, \Delta\mathcal{U}_{10}]$ calculated between 0000 UTC 7 October 2014 and 0000 UTC 10 October 2014 for running time average of width τ. The confidence interval of the null hypothesis of zero correlation (see section 3.4 for details) is estimated using the average autocorrelation length of $\Delta\mathcal{U}_{10}$ for a fixed τ.

the ANML_DOUBLE simulation is indicative of the significant action of the downwind SST gradient in the generation of surface wind convergence. This means that for sharp SST gradients, even if extended over short length scales, the vertical stability-instability process controlling the DMM mechanism is effective in slowing down the wind on the colder side of the fronts, generating surface wind convergence.

Concerning the correlation between ΔLSST and $\Delta\mathcal{C}_{10}$, the lower panel of figure 3.12 explicitly shows that for most simulations the correlation coefficients are not significant at the 95% level and, when they are so, they are very small. This happens for large values of μ, where $\rho[\Delta\mathrm{LSST}, \Delta\mathcal{C}_{10}]$ are statistically significant and comparable to $\rho[\Delta\mathcal{D}_{10}, \Delta\mathcal{C}_{10}]$, indicating that the PA mechanism needs longer length scales with respect to the DMM one to be effective. In fact, the $(\Delta\mathrm{LSST}; \Delta\mathcal{C}_{10})$ 2D distribution (not shown) is much more symmetrical with respect to the origin compared to the $(\Delta\mathcal{D}_{10}; \Delta\mathcal{C}_{10})$ one. This is a clear indication that the spatial phase difference between local SST maxima and surface wind convergence is not close to zero and, thus, the PA mechanism is not important in the SST-wind relationship over the relatively short spatial and temporal scales of the setup considered.

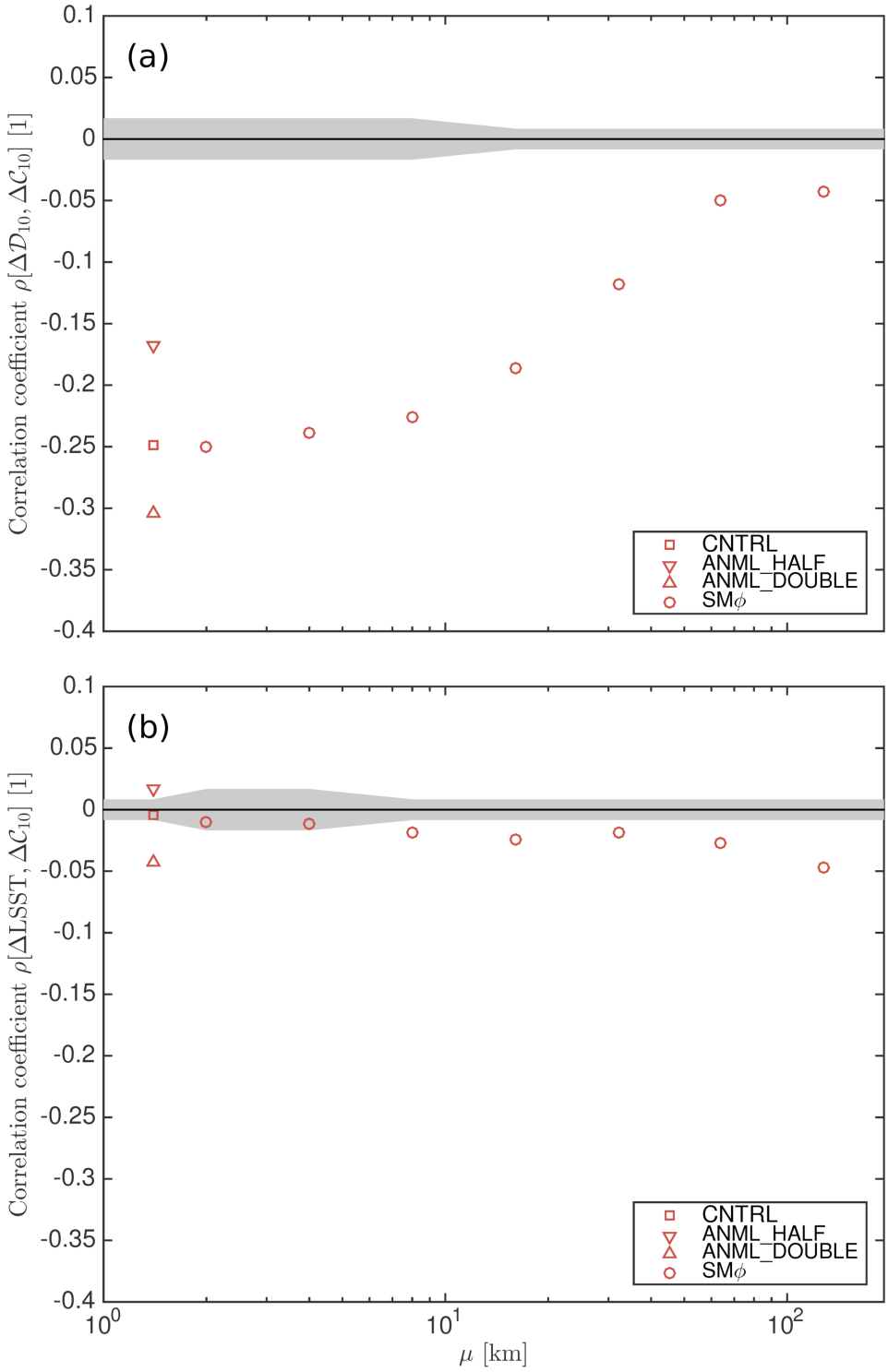

Figure 3.12: Spatial correlation coefficients between $\Delta\mathcal{D}_{10}$ and $\Delta\mathcal{C}_{10}$ (a) and between ΔLSST and $\Delta\mathcal{C}_{10}$ (b) averaged between 0000 UTC 9 October and 0000 UTC 10 October.

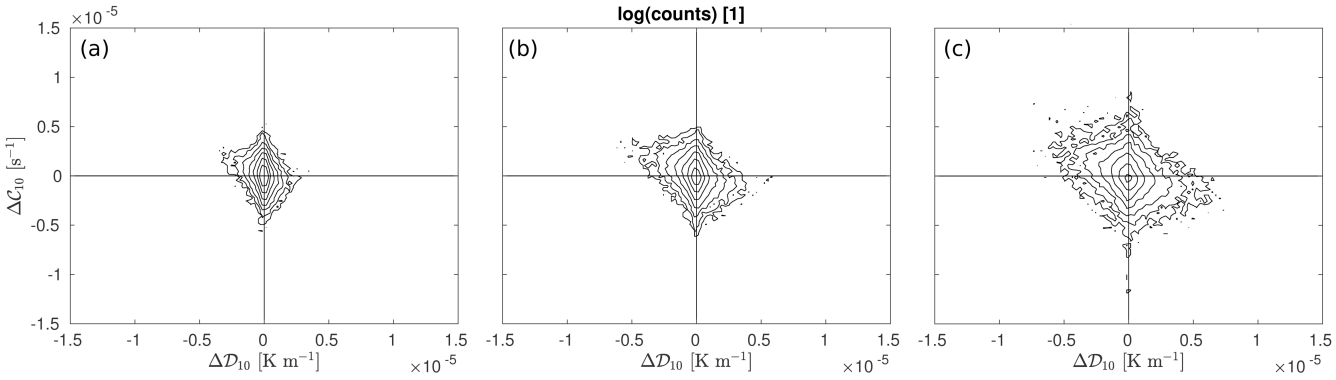

Figure 3.13: Two dimensional sample distribution of $(\Delta\mathcal{D}_{10}; \Delta\mathcal{C}_{10})$ for the simulations ANML_HALF (a), CNTRL (b) and ANML_DOUBLE (c). The presence of other mechanisms generating surface wind convergence is indicated by the significantly non-zero values of $\Delta\mathcal{C}_{10}$ around $\Delta\mathcal{D}_0$. Although, the negative correlation between the two fields become more and more evident going from panel (a) to panel (c).

A common feature of both panels of figure 3.12 is that the width of the 95% confidence interval is one order of magnitude smaller than the width of the same confidence interval of figure 3.10, where $\rho[\Delta\text{SST}, \Delta\mathcal{U}_{10}]$ are shown. This happens because the $\Delta\mathcal{D}_{10}$, $\Delta\mathcal{C}_{10}$ and ΔLSST all contain spatial derivatives of either the SST or the surface wind fields, which determines shorter autocorrelation lengths. This, in turns, increases the number of effective degrees of freedom (dof) and, thus, decreases the width of the confidence interval, as described in details in section 3.4. As an example of these shorter autocorrelation lengths, figure 3.14 shows the autocorrelation function of the $\Delta\mathcal{D}_{10}$ and $\Delta\mathcal{C}_{10}$ fields, in the left and right panel respectively, of different numerical simulations, averaged on the 9 October.

Figure 3.15, then, shows the fields $\Delta\mathcal{D}_{10}$ (a) and $\Delta\mathcal{C}_{10}$ (b), averaged on the 9 October. Even simple visual inspection of this figure suggests the good spatial correlation that exists between the downwind gradient SST field and the surface convergence one, as quantitatively shown above.

Rain band displacement

The same spatial correlation analysis can be performed on the appropriate time averaged variables on the 7 October 2014, which, in the current simulations, is characterized by intense convective rains due to two persistent convergence lines that form in the first half of the day over the sea (see the left panel of figure 3.7). All the same comments done for the correlation coefficients calculated on the 9 October apply to those of the 7 October (not shown), as well. In particular, the $\rho[\text{SST}, \Delta\mathcal{U}_{10}]$ and $\rho[\Delta\mathcal{D}_{10}, \Delta\mathcal{C}_{10}]$ are statistically significant at the 95% level, while most of the $\rho[\Delta\text{LSST}, \Delta\mathcal{C}_{10}]$ are not so; increasing the width of the SST filter decreases, in absolute value, the correlation coefficients due to the more effective action of the direct turbulent energy cascade; and

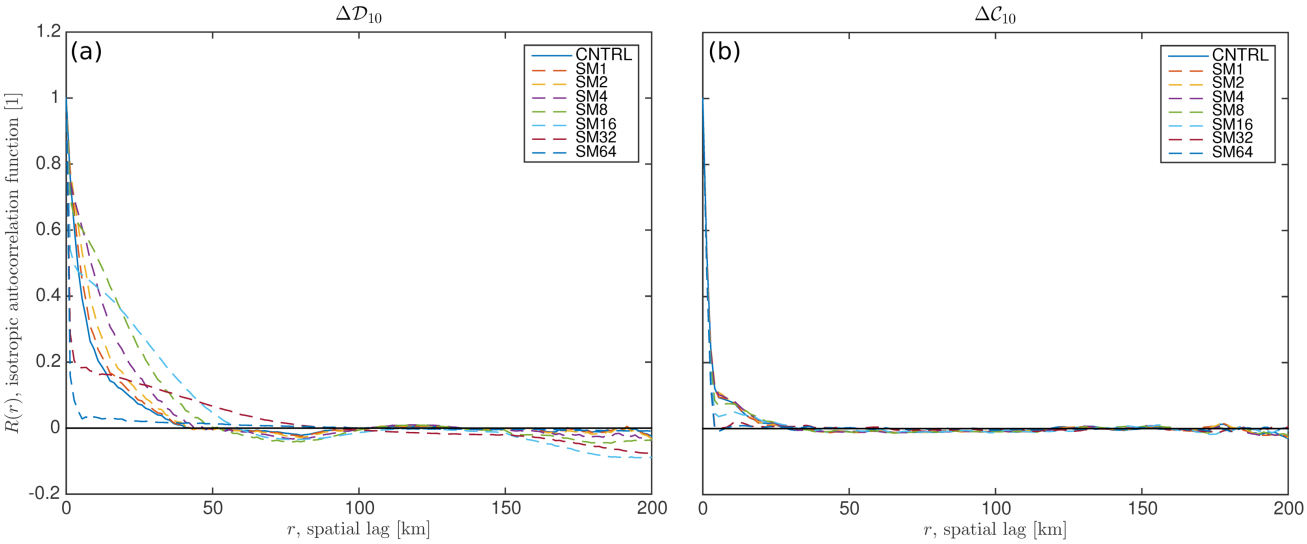

Figure 3.14: Autocorrelation functions of $\Delta\mathcal{D}_{10}$ and $\Delta\mathcal{C}_{10}$ on the 9 October for different simulations. With respect to the autocorrelation function of figure 3.9, these decay on much shorter length scales.

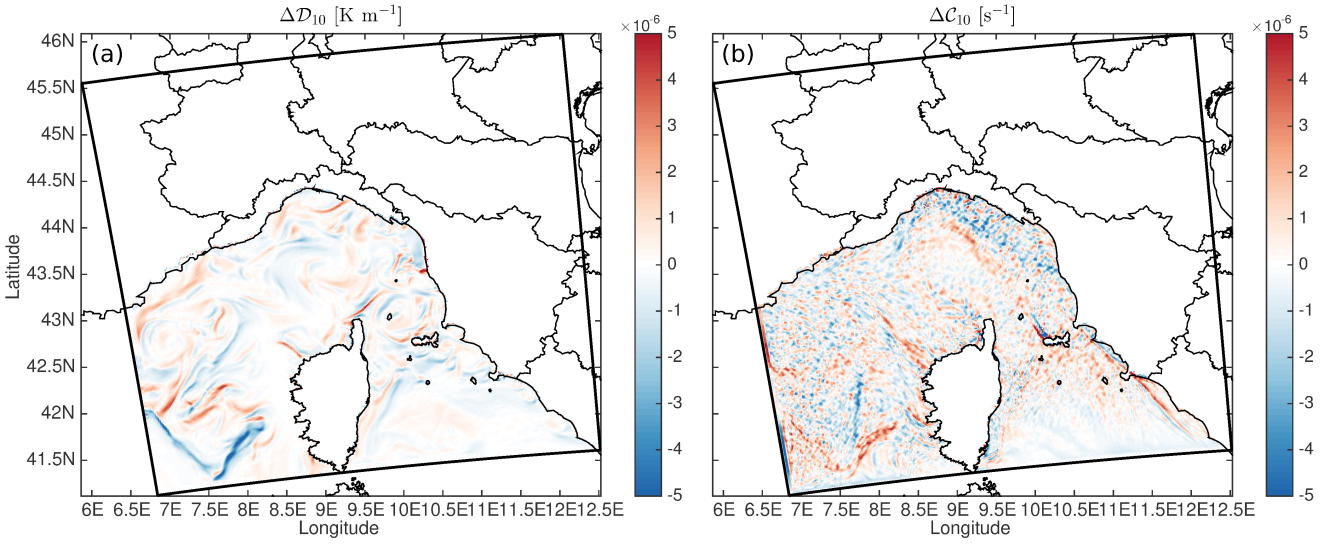

Figure 3.15: $\Delta\mathcal{D}_{10}$ in the panel (a) and $\Delta\mathcal{C}_{10}$ in the right one, for the 9 October of the CNTRL simulation.

the longer the duration of the time averages, the stronger the correlations. This suggests that even when deep convection is happening, the PA mechanism is not important and, through the DMM one, the surface wind convergence can be spatially controlled by the presence of SST gradients. The only remarkable difference between the 7 and 9 October correlation coefficients is that the absolute values of the significant ρ calculated on the 7 October are systematically smaller than those calculated on the 9 October (not shown) and possible explanation for that is based on the dynamics that leads to the heavy rain on the 7 October. In fact, the two convergence lines that trigger the deep convection are caused by the encounter of a cold dry continental air mass with a warmer and moister low-level jet coming from the sea, as the snapshot of figure 3.16 shows. This means that, with respect to a situation where the winds were only blowing from the sea towards the land (as it is, roughly, on the 9 October), the ocean-atmosphere imbalances are, on average, stronger. Thus, despite the more intense fluxes at the air-sea interface, this is likely to result in lower absolute value spatial correlation coefficients betweeen the fields considered.

It is interesting that, through the DMM mechanism, the presence of nonzero downwind SST gradients is able to displace one of the two convergence lines of the 7 October HPE. Figure 3.17 shows both the difference in the surface wind convergence between the CNTRL and UNIF simulations, $\Delta\mathcal{C}_{10}$, and the difference in the 24 hours cumulated precipitation $\Delta\mathcal{P}$. It appears that the convergence line close to the western boundary of the domain is not affected by the different SST forcings much, because it does not have the time to respond to the variations and is controlled by the large-scale forcing provided by the boundary conditions. But the convergence line above the Corsica island, instead, is clearly displaced, as the precipitation field shows. This displacement, of the order of 50 km, would be important for the forecast and is an evidence of how the SST structure can control the rainfall pattern through the modification of the surface wind convergence field. In the current simulations, the rain of the 9 October does not feel any similar effect, because the convection is triggered over land by the orography, which is the same in all the simulations.

3.6 Discussion and conclusions

The relative importance of the mechanisms controlling the SST-wind relationship (Small et al., 2008) is studied using a spatial correlation analysis of the appropriate time averaged variables, obtained from two series of numerical simulations in a pre-convective midlatitudes setup. In the literature, these mechanisms have been observed to be important over climatological time scales of months or, even, years (Chelton and Xie, 2010). While idealized numerical modeling works, generally characterized by simple geometries with SST fronts extending over 10-100 km scales, have investigated the fundamental processes involved also on shorter time scales, but lacking the complexity of the spatial structure of the real oceans (Skyllingstad et al., 2007; Spall, 2007).

In this work, by means of fully compressible primitive equation simulations, the PA and DMM mechanisms are studied over hourly time scales with the SST fields containing

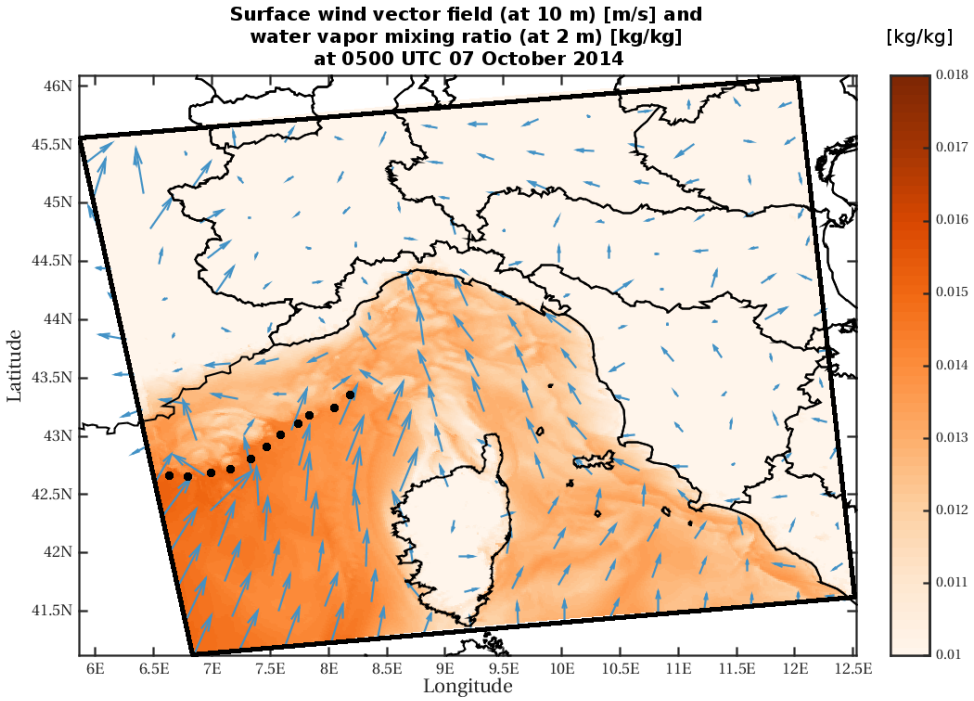

Figure 3.16: Snapshot of the surface wind vector field and the surface water vapor mixing ratio taken at 0500 UTC 7 October 2014 from the CNTRL simulation. The dots help to visualize the instantaneous convergence line, due to the encounter of a relatively drier air mass coming from the land and a relatively moister one coming from the sea.

up to few km spatial structures. It is found that the downward mixing of momentum induced by the increased air column instability while crossing a front from cold to warm is the mechanism that produces a remarkable spatial correlation between the SST and the wind magnitude, with the large-scale circulation removed. The competing mechanism, controlled by the air pressure adjustment above the SST local minima and maxima, is found to be of negligible importance for the submesoscale eddy-containing SST fields considered. Only for very smooth SST fields, with variations of temperature taking place over $O(100$ km) length scales, the two mechanisms have comparable importance, which, however, appears to be of secondary order.

The reason why the PA mechanism is not significantly contributing to the control of the wind structure by the SST is because it is effective over relatively long length scales. It fact, is has been shown to act over the horizontal length scale $L_p = h^2U/\kappa$, where h is the planetary boundary layer height, U is the typical wind speed and κ is the

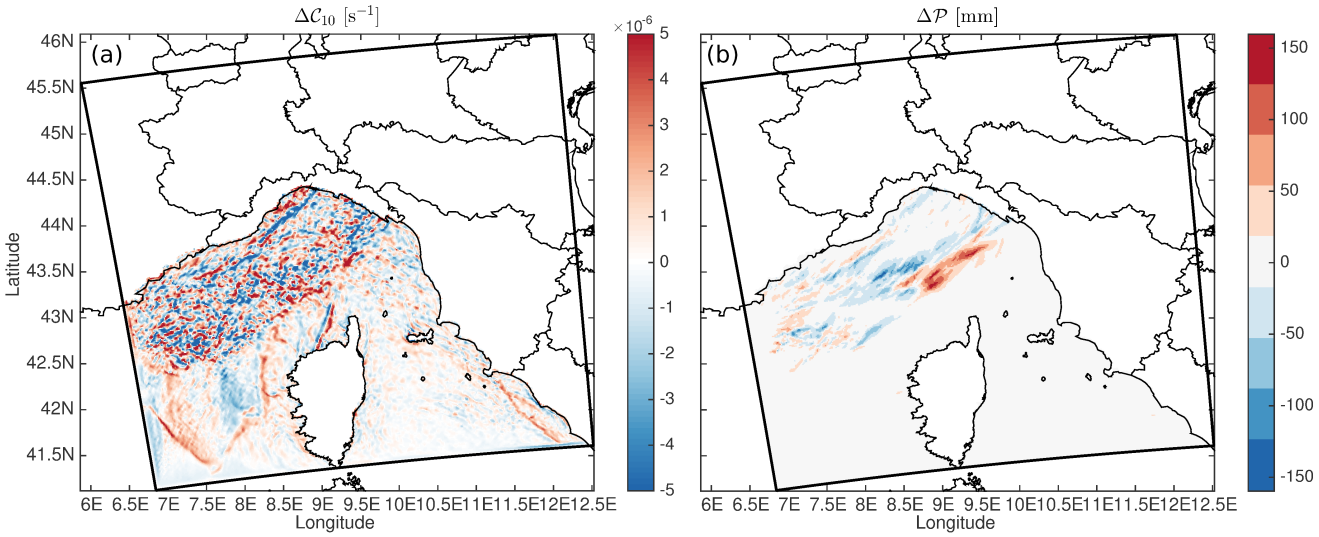

Figure 3.17: Difference in surface wind convergence (a) and precipitation cumulated on 24 hours on the 7 October (b) between the CNTRL and the UNIF simulations. A significant displacement of the rainband of the order of 50 km is visible right above the Corsica island.

turbulent eddy diffusion coefficient (Small et al., 2008). This length scale arises from the temperature advective-diffusive equation describing an air parcel crossing a SST front and modifying its temperature by the same amount as the frontal SST variation. Taking as typical values $h \sim 500$ m, $U \sim 10$ m s^{-1} and $\kappa \sim 10$ m^2 s^{-1}, one finds that L_p is of the order of few hundreds of km, which is at least an order of magnitude larger than the SST structures of most of the simulations considered.

From a lagrangian point of view, an air parcel moving above a fine structure SST field filters out the fast variations of the temperature forcing, due to its thermal inertia. This can be represented in an extremely simple way by discretizing the advective-diffusive equation over two layers, where the surface layer temperature T_s responds to the SST instantaneously and the overlying layer one T_o, at height h, changes because of the turbulent heat transfers controlled by the diffusion κ. Using D/Dt to denote the material derivative, the spatial variations of the SST in an eulerian description correspond to temporal variations of the surface layer forcing temperature in a lagrangian one. The advective-diffusive equation is then written as

$$\gamma \frac{DT_o}{Dt} = T_s - T_o, \tag{3.17}$$

with $\gamma = h^2/\kappa$. Transforming the forcing function $T_s(t)$ in the Fourier space with

$$\hat{T}_s(\omega) = \frac{1}{\sqrt{2\pi}} \int_{-\infty}^{+\infty} \mathrm{d}\omega \, \mathrm{e}^{i\omega t} T_s(t) \tag{3.18}$$

as a function of the frequency ω and with i denoting the imaginary unit (Arfken and Weber, 2006), the solution for the top layer temperature, the unknown, is

$$\hat{T}_o(\omega) = \frac{\hat{T}_s(\omega)}{1 - \gamma i\omega}, \tag{3.19}$$

which shows the low-pass behavior of the air parcel, since the transfer function

$$\frac{|\hat{T}_o|}{|\hat{T}_s|} = \frac{1}{\sqrt{1 + \gamma^2\omega^2}} \tag{3.20}$$

decays for high frequencies ($\omega \to +\infty$). Then, the cutoff temporal scale is found to be proportional to γ, which is directly related to the length scale L_p introduced above.

This is consistent with previous observations (Minobe et al., 2008) and numerical works (Takatama et al., 2012, 2015), where the PA mechanism was found to be dominant over large-scale structures such as the western boundary currents. Thus, for SST fields with remarkable structure at the submesoscale, where the variations of the forcing temperature can be fast, the marine atmospheric boundary layer filters out the high frequencies through the PA mechanism. The only possibility for the small SST structures to influence the overlying atmosphere is by reducing the surface stability enough to mix momentum in the vertical direction, which happens if the horizontal SST gradients are sharp enough.

In a more holistic approach, atmosphere-ocean-wave coupled simulations Carniel et al. (2016); Ricchi et al. (2016, 2017) could be used to further study the SST-wind relationship considered in the this chapter. In particular, the acceleration of the surface wind through the DMM mechanism might be influenced. In fact, for high wind intensities the inclusion of wave dynamics reduces the wind speed because of a higher surface momentum flux from the atmosphere to the ocean thanks to the large wave height. Thus, if the wind speed ahead of the SST front impacts the wave height and, thus, the momentum flux, for a fixed SST gradient across the front, the surface wind acceleration would be reduced in the case of high waves.

Finally, it is found that through the DMM mechanism, the submesoscale SST structure can affect the position of the convective rain bands, by partially controlling the surface convergence over the sea. The simulated displacement is of the order of 50 km, which would be particularly significant from a forecasting point of view, and it is found in the numerical simulations during the HPE over the sea on the 7 October, which is not particularly relevant for the society. But since it has been observed that even the HPEs that hit cities over land are generally produced by convergence lines that form over the sea, this finding encourages more efforts in modeling the air-sea interactions at even shorter temporal and spatial scales, to correctly capture the dynamics over the sea.

Although, it is important to underline that there are cases in which the dynamics of the trigger of the deep convection might not be dominated by the DMM mechanism. In fact, it could happen that the virtual orography that causes the low-level jet lifting might be thick and stable enough so that the DMM mechanism is not able to produce deep convection by locking the surface convergence lines along the SST fronts.

By studying other HPEs, which are not rare along the coasts of the Mediterranean sea, then one could try to identify more precisely the conditions for which the DMM controls the position of the convergence lines and better understand whether these processes have some form of threshold behavior in terms, for example, of the intensity of the SST gradient needed to produce deep convection given the upstream surface wind speed.

Four

Oceanic vertical thermal structure role in the modulation of HPEs

The importance of the upper ocean thermal vertical structure (mixed layer depth and stratification) in the control of the precipitation during a heavy-rain-producing mesoscale convective system is investigated by means of numerical simulations. In particular, the fully compressible, non-hydrostatic equations for the atmosphere and the hydrostatic Boussinesq equations for the ocean are numerically integrated to study the effect of the ocean-atmosphere coupling both with realistic initial and boundary conditions and with simpler, semi-idealized ocean temperature vertical profiles. It is found that the action of the winds associated with the synoptic system, in which the heavy precipitation event is embedded, can entrain deep and cold water in the oceanic mixed layer, generating surface cooling. In the case of shallow mixed layer and strongly stratified water column, this decrease in sea surface temperature can significantly reduce the air column instability and, thus, the total amount of precipitation produced.[1]

4.1 Introduction

The Mediterranean basin is a semi-enclosed sea with high orography surrounding it. The presence of such mountains near the coasts impacts the coastal meteorology and the ocean dynamics through intense air-sea exchanges, due to interaction of cold dry continental winds with warm moist air over the sea (Flamant, 2003; Lebeaupin Brossier and Drobinski, 2009).

Such strong and complex interactions among land, air and sea are known to produce heavy precipitation events (HPEs) that are characterized by small spatial (10-100 km) and temporal scales (hours) (Ducrocq et al., 2014). Often, these heavy rainfalls are carried by mesoscale convective systems (MCSs), in which deep convective cells re-form in the same position for several hours (Schumacher and Johnson, 2005, 2008, 2009).

[1]For most part, this chapter has been submitted for peer review as Meroni, A. N., L. Renault, A. Parodi and C. Pasquero, 2018 (expected): Role of the oceanic vertical thermal structure in the modulation of heavy precipitations over the Ligurian Sea. *Pure Appl. Geophys.*

Previous works have studied the effect of increasing the horizontal resolution of the sea surface temperature (SST) used to force atmospheric numerical simulations of HPEs (Millán et al., 1995; Pastor et al., 2001; Lebeaupin et al., 2006; Cassola et al., 2016) finding that, generally, finer resolution SST fields improve the total precipitation forecast. Using an atmospheric numerical model, Pastor et al. (2001) and Lebeaupin et al. (2006) show that the mean SST over a certain area not too far from the precipitation event controls the amount of rain and that the SST structure modulates the precipitation. In particular, variations in the average SST value modify the surface air stability and the intensity of the warm low-level jet, which is often responsible for the intensity of the precipitation in such events. Warmer average SST moistens and heats up the marine boundary layer, which becomes more unstable and can trigger larger rainfalls. A similar dependence of the intensity of an extreme storm on the average SST in the Mediterranean sea has been found also by De Zolt et al. (2006). Instead, the presence of fine structure SST features, on the km scale, has been shown to play a minor role in terms of the total cumulated precipitation, but to substantially improve the spatial structure of the local heat fluxes, especially in an atmosphere-ocean coupled setup (Carniel et al., 2016; Ricchi et al., 2016, 2017). More on the role of the SST horizontal structure in influencing the precipitation is contained in chapter 3. The focus of the present chapter is to understand the role of the oceanic thermal vertical structure in the control of the HPE, using an ocean-atmosphere coupled approach, which has already proved to be of interest in the region (Lionello et al., 2003; Small et al., 2011, 2012).

In one of the first coupled model experiments for this geographical area, Lebeaupin Brossier et al. (2013) show how the coupled dynamics can be particularly important in some events. In their case study, the ocean dynamics connects two events that would be independent from an atmospheric point of view. In fact, the surface cooling associated with the enhanced air-sea fluxes and with the vertical mixing between mixed layer water and deeper (and colder) waters during a mistral event reduces the upper ocean heat content available for the subsequent HPE, resulting in a decrease in the total precipitation compared to an uncoupled case. Berthou et al. (2015), using similar numerical simulations as Lebeaupin Brossier et al. (2013), strengthen the role of the ocean in connecting strong wind events with HPEs. In particular, they show that there are heavy precipitation events in which submonthly atmosphere-ocean coupling mechanisms, such as the SST cooling after a mistral event, play a significant role in controlling, for example, the rainfall location.

At different latitudes, a very interesting negative feedback mechanism takes place at the air-sea interface below tropical cyclones: the intense winds of the cyclonic system entrain cold water from the base of the oceanic mixed layer, that reduces the enthalpy fluxes at the sea surface and, thus, reduces the intensity of the cyclone itself (Schade and Emanuel, 1999; Mei et al., 2015). The goal of the analysis presented in this chapter is to explore whether a similar mechanism takes place in the midlatitudes systems that lead to heavy-rain-producing MCSs. In particular, the hypothesis is that the intense winds of the synoptic system that drives the MCS, by cooling and deepening the oceanic mixed layer in the days preceding the HPE, can reduce the SST which, in turns, can reduce

the precipitation.

Three-dimensional numerical simulations, both in atmosphere-only and in ocean-atmosphere coupled configurations, are run to study a heavy-rain-producing MCS at midlatitudes, in Liguria, which is a region in the North-West of Italy where multiple HPEs of this kind have been observed in the past few years (Rebora et al., 2013; Buzzi et al., 2014; Fiori et al., 2014; Cassola et al., 2015, 2016; Fiori et al., 2017). In particular, the focus is on the 9 October 2014 event, that hit the Bisagno catchment and the city of Genoa (Faccini et al., 2015; Silvestro et al., 2015; Cassola et al., 2016; Fiori et al., 2017; Lagasio et al., 2017), causing a flash flood that was responsible for one casualty and damages worth up to roughly 100 M€. In section 4.2 the setup of the different numerical simulations is described. Section 4.3 is devoted to analyse the effect of the ocean-atmosphere coupling in the event studied using fine scale and realistic initial and boundary conditions. In section 4.4, instead, the role of the mixed layer depth (MLD) and oceanic stratification is analysed by means of numerical coupled simulations forced with simpler oceanic vertical temperature profiles and section 4.5 is for discussion and conclusions.

4.2 Setup of the numerical simulations

Two primitive equation models, the Weather and Research Forecast model, WRF version 3.6.1, (Skamarock et al., 2008) and the Regional Ocean Modeling System (ROMS) in its Coastal and Regional Ocean COmmunity (CROCO) version (Penven et al., 2006; Debreu et al., 2012) are coupled to investigate the role of the oceanic vertical thermal structure in the modulation of the HPE considered.

Atmospheric model configuration

For the atmospheric component, a three domain two-way nested simulation is first run with WRF stand-alone (figure 4.1, left panel). It is initialized and forced at the boundary with the operational ECMWF-IFS NWP model (Simmons et al., 1989), which has a horizontal resolution of 0.125°. It runs for four days, from 0000 UTC 06 October 2014 to 0000 UTC 10 October 2014.

The configuration of the domains is the same as the one of the simulations of the previous chapter. The largest domain, d01, is the Euro-Cordex one (Jacob et al., 2014) and has a resolution of 12 km. The intermediate domain, d02, covers the entire western Mediterranean basin, most of southern Europe and northern Africa with a resolution of 4 km. The smallest domain, d03, which has a resolution of 1.4 km, covers the Ligurian Sea, where the events of interest happen (see figure 4.1). In the vertical direction the grid has 84 levels, as in Fiori et al. (2014), and the cylindrical equidistant projection with a rotated North Pole is used.

The physical parametrizations, chosen according to previous sensitivity experiments in very similar setup (Fiori et al., 2014), are the following: the WRF Single-Moment 6-Class scheme, WSM6 (Hong and Lim, 2006), for the microphysics; the Mellor-Yamada

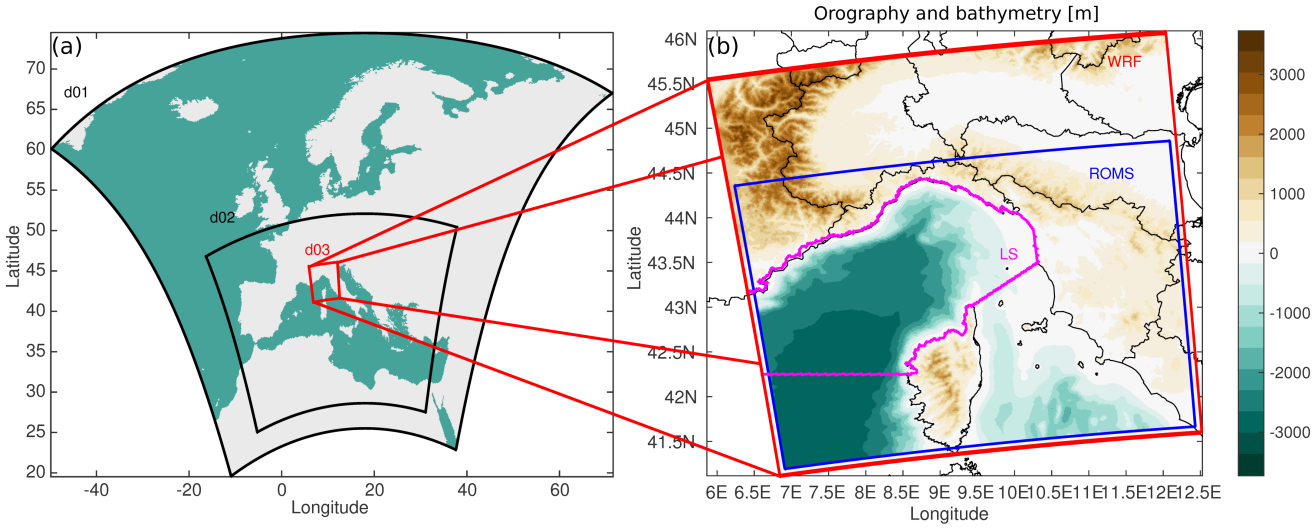

Figure 4.1: (a): The three domains (d01, d02, d03) used in the double-nested preparatory WRF simulation. (b): In red the extesion of the WRF domain used in CNTRL, CPLD, UNIF and L*_M*_sea simulations, that corresponds to the d03 domain of the preparatory simulation; in blue the extension of the ROMS domain used in the coupled simulations, CPLD and L*_M*_sea. The false colors show the orography and the bathymetry of the domains in meters. The Ligurian Sea (LS), which is a region over which some diagnostics are defined in the text, is highlighted in magenta.

Nakanishi Niino level 2.5 option (Nakanishi and Niino, 2006, 2009) for the planetary boundary layer; the Tiedtke option (Tiedtke, 1989; Zhang et al., 2011) for the cumulus parameterization, activated only on the largest domain, d01; the RRTM longwave scheme (Mlawer et al., 1997) and the Goddard shortwave scheme (Chou and Suarez, 1999; Chou et al., 2001) for the radiative fluxes; the 5-layer thermal diffusion scheme (Dudhia, 1996) for the land surface; the revised MM5 similarity scheme (Beljaars, 1994) for the surface layer. Vertical diffusion is performed with a three dimensional turbulent kinetic energy closure scheme that mixes the full fields and not only the perturbation fields.

Oceanic model configuration and spin-up

For the oceanic counterpart, a spin-up simulation with ROMS stand-alone is run for three weeks before the event, starting from 0000 UTC 15 September 2014. The Mediterranean Forecasting System product (Oddo et al., 2009) is used as initial and lateral forcing, while the surface forcing comes from the ECMWF-IFS NWP model (Simmons et al., 1989), as for the atmospheric model, and provides the momentum, heat and freshwater fluxes. The domain (figure 4.1, right panel) does not contain all the land points of and, over the sea, is slightly smaller than the d03 WRF domain described above (345x262 grid-points

for ROMS instead of 358x370, as in WRF) but has the same 1.4 km grid spacing in the horizontal. In the vertical, the grid is made of 60 levels, with a finer vertical resolution near the free surface according to the algorithm of Shchepetkin and McWilliams (2009), with the following stretching parameters: $h_{cline} = 250$ m, $\theta_b = 2$ and $\theta_s = 7$.

The bathymetry is obtained from the Shuttle Radar Topography Mission global bathymetry and elevation data at 30 arc s resolution with data voids filled (SRTM30_PLUS) dataset (available at http://topex.ucsd.edu/WWW_html/srtm30_plus.html). This product is based on the 1-min resolution Sandwell and Smith (1997) global dataset. In order to avoid aliasing and to ensure a smooth bathymetry in the grid model, a gaussian filter is applied to the input SRTM30_PLUS data. A second filter is then applied on the topography where its steepness exceeds a threshold value $r = 0.2$. This is done in order to avoid errors in the pressure gradient computations due to steep bathymetric slope in shallow region with terrain-following coordinates (Beckmann and Haidvogel, 1993). Radiative open boundary conditions for baroclinic velocities and tracers are imposed on the western and southern sides (Orlanski, 1976; Raymond and Kuo, 1984).

Lateral advection is integrated with a third order upstream scheme (Shchepetkin and McWilliams, 1998) for momentum and with a split and rotated third order upstream scheme for tracers (Marchesiello et al., 2009; Lemarié et al., 2012). This reduces the spurious diapycnal mixing that would be produced along the sigma level and is, thus, suitable for realistic applications with variable bathymetry. Vertical advection, instead, is integrated with a semi-implicit scheme both for momentum and for tracers (Shchepetkin, 2015). As for the turbulent mixing, it is represented with the Smagorinsky parameterization in the horizontal (Smagorinsky, 1963) and with the nonlocal K-profile parameterization in the vertical (Large et al., 1994). The selected nonlinear equation of state is described in Shchepetkin and McWilliams (2003) and it is a modified version of the Jackett and McDougall (1995)'s one.

Numerical simulations of interest

All the simulations are initialized at 0000 UTC 06 October 2014 and run for four days, up to 0000 UTC 10 October 2014, in a single WRF domain (d03 of the preparatory simulation described above), coupled to the ROMS domain, when needed (figure 4.1, right panel). The atmospheric initial and boundary conditions are all obtained from the output files of the intermediate domain, d02, of the preparatory simulation described in section 4.2 with the NDOWN tool (Skamarock et al., 2008). Four model configurations are considered. They differ from one another in the initial SST field, in the fact that they are coupled or not and, for the coupled ones, in the structure of the initial and lateral vertical ocean temperature forcing, as explained in what follows.

The CNTRL simulation is not coupled to the ocean model and is forced at the surface with the SST field obtained from the last output of the ROMS spin-up simulation at 0000 UTC 06 October 2014. The SST is then kept constant until the end, exactly as in chapter 3.

In the CPLD simulation, the atmospheric model is coupled to the ocean model through the Ocean Atmosphere Sea Ice Soil coupler, version 3.0 (OASIS3) (Valcke,

2013). Every hour, the two models exchange the following fields over the sea-points of the domain: ROMS produces the SST and the surface currents for WRF and WRF sends to ROMS the freshwater, heat and momentum fluxes estimated with the COARE bulk formulae (Fairall et al., 2003). The ocean initial conditions are obtained from the ROMS-alone spin-up simulation, as described in section 4.2. The ROMS grid is defined starting from the WRF one, so that the definition of the land and sea masks are straightforward.

The UNIF simulation, which has already been introduced in the previous chapter, is run with WRF stand-alone and has a homogeneous SST field, equal to the horizontal average over the sea of the SST of the CNTRL simulation, which is, here, not allowed to evolve in time. If $\mathrm{SST}_0(x, y)$ is the initial field of the CNTRL simulation, its horizontal average is simply

$$\overline{\mathrm{SST}} = \frac{1}{|\mathrm{sea}|} \iint_{\mathrm{sea}} \mathrm{d}x\mathrm{d}y \, \mathrm{SST}_0(x, y) = 22.58°\mathrm{C}, \tag{4.1}$$

where $|\mathrm{sea}|$ the area of the domain that is occupied by the sea.

The series of simulations L*_M*_sea are coupled to ROMS, they have the same homogeneous initial SST field as the UNIF case, $\overline{\mathrm{SST}} = 22.58°\mathrm{C}$, and they differ in the two parameters that define the vertical temperature profile of the initial and boundary conditions. In particular, the idealized potential temperature profile prescribed everywhere in the domain at the beginning of the simulation and at the open boundaries during the runs, is of the form

$$\theta(z) = \begin{cases} \theta_{ML} & \text{for } z > M \\ (\theta_{ML} - \theta_d) \exp\left[(z - M)/L\right] + \theta_d & \text{for } z_b < z < M, \end{cases} \tag{4.2}$$

where the depth z is negative below the sea surface down to the bottom topography value z_b, $\theta_{ML} = \overline{\mathrm{SST}}$ is the mixed layer temperature and $\theta_d = 12.84°\mathrm{C}$ is representative of the temperature at depth in the domain considered (taken from the CPLD simulation). Thus, these simulations differ in the values of M, the initial MLD, and L, the e-folding length of the exponential profile. The name of the simulations contains the values of these two parameters in meters: for example, a simulation named L5_M25_sea is characterized by a decaying e-folding length of 5 m and a MLD of 25 m. Following the climatology of D'Ortenzio et al. (2005), which shows that in the Ligurian Sea in October the average MLD is between 15 and 30 m deep, the values of M are chosen to vary between 5 m and 35 m, with two possible values of L, 5 m and 35 m. Figure 4.2 shows four examples of potential temperature profiles used to force the appropriate L*_M*_sea simulations. The salinity is imposed to be equal to 38.25 psu, that correponds to 38.43 g kg $^{-1}$ in units of absolute salinity, everywhere in the basin at the beginning of the simulations and, then, along both open boundaries (South and West). These simple temperature and salinity vertical profiles, that are defined using relevant values of parameters for the setup considered, are used both as initial conditions and as lateral forcing along the southern and western open boundaries.

In all these simulations (CNTRL, CPLD, UNIF, L*_M*_sea), the subgrid parameterization options are the same as the ones described in the previous subsections on

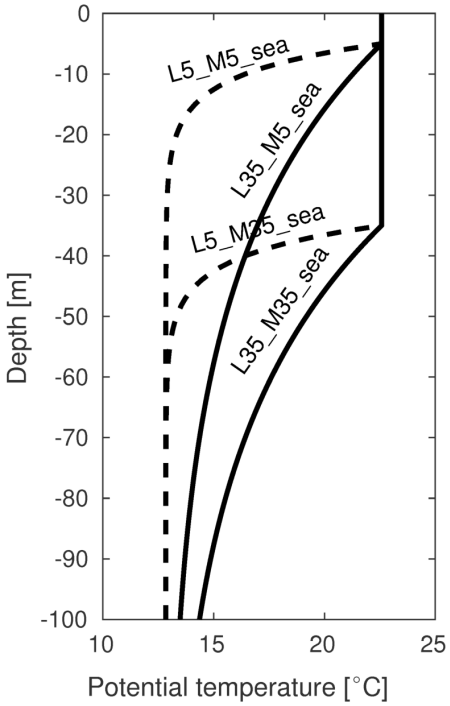

Figure 4.2: Examples of potential temperature profiles used to force some simulations, as indicated in the figure.

Table 4.1: Summary of the simulations of interest. The $\mathrm{SST}_0(x, y)$ is obtained from the ROMS spin-up simulation as described in the text and $\overline{\mathrm{SST}}$ is the horizontal average of the $\mathrm{SST}_0(x, y)$ field, as in equation 4.1.

Name	Initial SST	Coupling
CNTRL	$\mathrm{SST}_0(x, y)$	no
CPLD	$\mathrm{SST}_0(x, y)$	yes
UNIF	$\overline{\mathrm{SST}}$	no
L*_M*_sea	$\overline{\mathrm{SST}}$	yes

the preparatory simulations, both for the atmospheric model and for the oceanic one. A summary of the configurations of the numerical experiments containing the initial SST field and the switch for the coupling is given in table 4.1.

4.3 Effect of the ocean-atmosphere coupling

The synoptic conditions leading to the 9 October HPE are well described by Cassola et al. (2016); Fiori et al. (2017). They mainly consisted of an upper-level trough over the

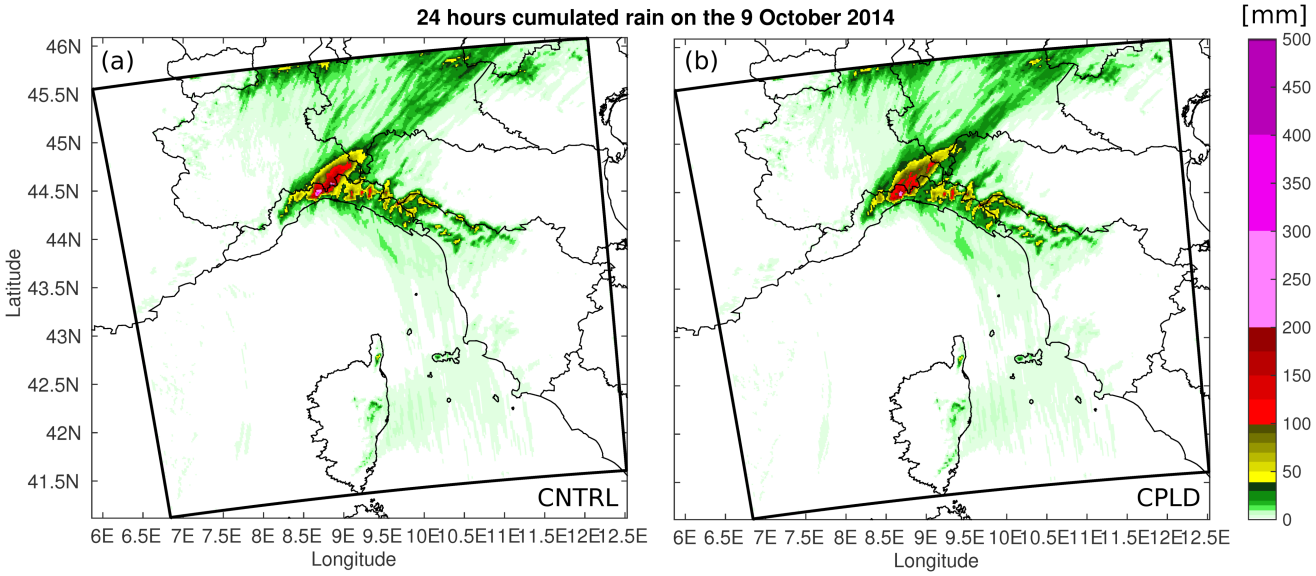

Figure 4.3: Maps of the total rain cumulated over 24 hours [mm] on the 9 October in the simulations CNTRL (a) and CPLD (b).

Atlantic Ocean, near Ireland, which produced a low-level flow blowing from South over the gulf of Genoa. On the 9 October 2014, a relatively cold and dry air mass flowing over the gulf of Genoa from the land played the role of a virtual orographic step, so that the warmer and more humid low-level jet blowing over the sea could overcome its level of free convection, generating the heavy-rain-producing MCS under study (Fiori et al., 2017).

Since the goal of this work is not to develop a more accurate forecast of the HPE, in this chapter, the CNTRL simulation is taken as reference, even if it is known that it differs from reality in terms, for example, of the total precipitation (it underestimates it) or of location of the convective rain (in the simulation it does not rain over the sea as observed, but over the land only). As already mentioned, the reasons why no rain is simulated over the sea are to be found in the time of initialization of the model. In the present work, the choice of initializing the simulations three days before the event is done in order to let the sea respond to the wind forcing of the synoptic system associated with the MCS.

The previous chapter gives a more detailed description of the simulated event, while here, only the features relevant to the discussion about the ocean coupling are introduced. In particular, figure 4.3 shows the maps of the total precipitation cumulated on the 9 October 2014 in the CNTRL simulation (a) and the CPLD one (b). It is clear that the coupling with the fully resolved ocean dynamics does not have a relevant impact on the precipitation field cumulated over 24 hours.

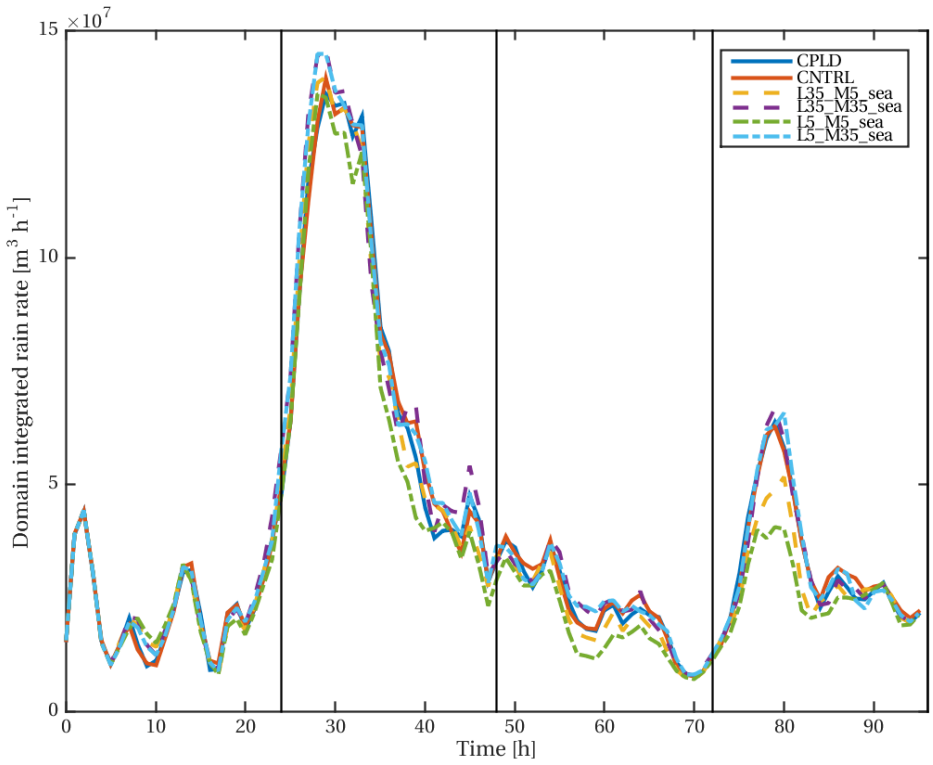

Figure 4.4: The hourly precipitation rate integrated over the entire domain of the simulation is shown as a function of time. The vertical black lines denote the midnight. Two high peaks are visible, one around 0700 UTC 7 October 2014 and the other around 0800 UTC 9 October 2014. The two least-rain-producing simulations are the ones with the shallowest initial mixed layer, L5_M5_sea and L35_M5_sea.

In figure 4.4, which is the equivalent of figure 3.6 of the previous chapter, one can see the hourly precipitation rate integrated over the entire domain as a function of time. There is a first high peak of precipitation around 0700 UTC 7 October 2014, which corresponds to a HPE over the sea, and then a second peak around 0800 UTC 9 October 2014, which is the heavy rainfall that hit the Bisagno catchment and the city of Genoa. Even if the first peak, which happened only over the sea on the 7 October, is higher than the second one, the focus of the following analysis is on the rainfall of the 9 October because it happened over land and, thus, it has been more relevant for the society. Once again, the coupling with the ocean dynamics modifies the evolution of the precipitation so little that the CPLD line is almost indistinguishable from the CNTRL one.

The hypothesis for an explanation of such little influence of the ocean dynamics on

the HPE is that the oceanic mixed layer is deep enough so that it is able to insulate the stratified (colder) water at its base from the vertical mixing action of the winds. In fact, in a thermally stratified ocean, if the mixing is strong enough to deepen and cool down the mixed layer, then the SST and, together with it, the surface heat fluxes are affected by the presence of a dynamical ocean. Otherwise, if the mixing is confined to the mixed layer, no surface expression of the presence of subsurface heat anomalies can impact the thermodynamics of the atmospheric boundary layer and, thus, the precipitation.

Following the definition of MLD given by Houpert et al. (2015), namely the depth at which the temperature is 0.1°C colder than the SST, the instantaneous maps of MLD can be calculated from the CPLD simulation. Figure 4.5 shows the MLD at the beginning of the simulation (0000 UTC 6 October 2014) and after three days from the beginning, i.e. after two days of intense winds but before the day of the HPE (at 0000 UTC 9 October 2014). It is easy to see that qualitatively it has not changed much and, in fact, by calculating its horizontal average over the sea,

$$\overline{\mathrm{MLD}} = \frac{1}{|\mathrm{sea}|} \iint_{\mathrm{sea}} \mathrm{d}x\mathrm{d}y\, \mathrm{MLD}(x, y), \tag{4.3}$$

one finds that it has changed from $\overline{\mathrm{MLD}} = 21.65$ m at 0000 UTC 6 October 2014 to $\overline{\mathrm{MLD}} = 21.83$ m at 0000 UTC 9 October 2014, much less than the vertical resolution of the grid (few meters in the upper ocean). Also figure 4.8 shows that the sea averaged MLD does not change in time throughout the CPLD simulation.

4.4 Role of the vertical oceanic thermal structure

Effects on the SST

The goal of the series of simulations L*_M*_sea is to explore a portion of the parameter space that defines the vertical thermal structure of the ocean, described with the simple potential temperature profile of equation (4.2), to see how the initial state of the ocean can affect the heavy precipitation of a MCS.

Figure 4.6 shows that the intense winds associated with the synoptic cyclone in which the heavy-rain-producing MCS is embedded start blowing over the domain on the 7 October, a couple of days before the HPE that hit the city of Genoa. The reason why all the simulations are initialized at 0000 UTC 6 October 2014 is to let the ocean responds to the wind forcing that is ahead of the intense rainfall. The two days of intense winds preceding the rainfall peak of the 9 October reduce the average SST in the Ligurian sea mostly by entrainment in the mixed layer of deeper and colder water. Depending on the initial vertical profile, this effect is more or less pronounced, as shown in figure 4.7, where the daily mean of the SST averaged over the Ligurian sea is displayed as a function of time for some simulations. For a shallow initial mixed layer ($M = 5$ m), the cooling can be as large as 1°C ($L = 35$ m) or 2°C ($L = 5$ m), while for a deeper initial mixed layer ($M = 35$ m), it can be as small as 0.1°C. The simulation with the highest cooling is the one with the shallowest initial mixed layer ($M = 5$ m) and the strongest stratification ($L = 35$ m).

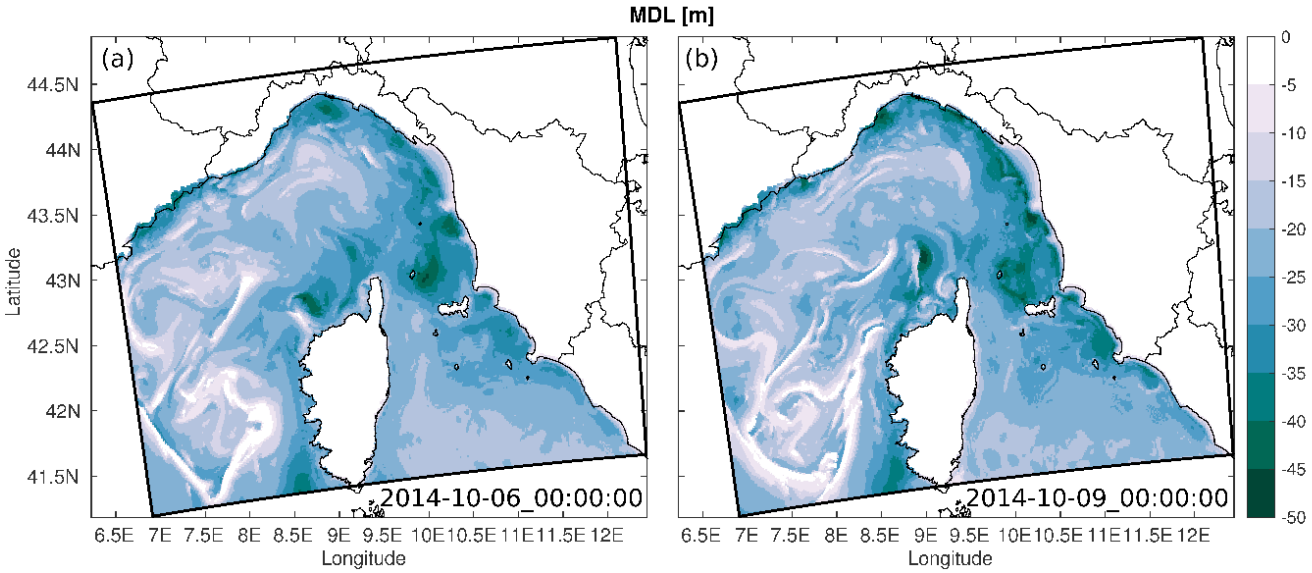

Figure 4.5: MLD [m] from the CPLD simulation at two different instants: at the beginning of the simulation (a) and after three days, at the midnight before the HPE (b).

In the case where the mixed layer is too deep, there is a restratification at the base of the mixed layer due to the shear turbulent heat fluxes due to an imbalance of the current and temperature initial conditions. This restratification causes a shallowing of the mixed layer, because the mixing happens in the upper thermocline, near the temperature interface. Figure 4.8 supports this interpretation, by showing the daily mean MLD, averaged over the sea as a function of time for some simulations. For a shallow initial mixed layer ($M = 5$ m), the winds are able to deepen it, in particular when the underlying stratification is relatively weak ($L = 35$ m). For a deeper initial mixed layer ($M = 35$ m), the deep and cold water at its base are insulated from the mixing action of the winds and thus the MLD is basically constant, as well as the SST shown in the previous figure. For the case with strong stratification ($L = 5$ m), there is a slight thinning of the MLD during the first simulated day, because of the shear induced mixing at the sharp temperature vertical gradient at the base of the mixed layer. The CPLD case average MLD does not change much over the duration of the simulation, which suggests that the winds are not strong enough to affect it, as previously explained.

By looking again at figure 4.7, it is interesting to note that the IFS SST (Simmons et al., 1989), that is used to force atmospheric model as described in section 4.2, shows a significant reduction over the course of the second day period, while in the coupled simulation, where the mixed layer is about 20 meters deep, the average SST reduction is almost one order of magnitude smaller. A SST reduction similar to the IFS one is

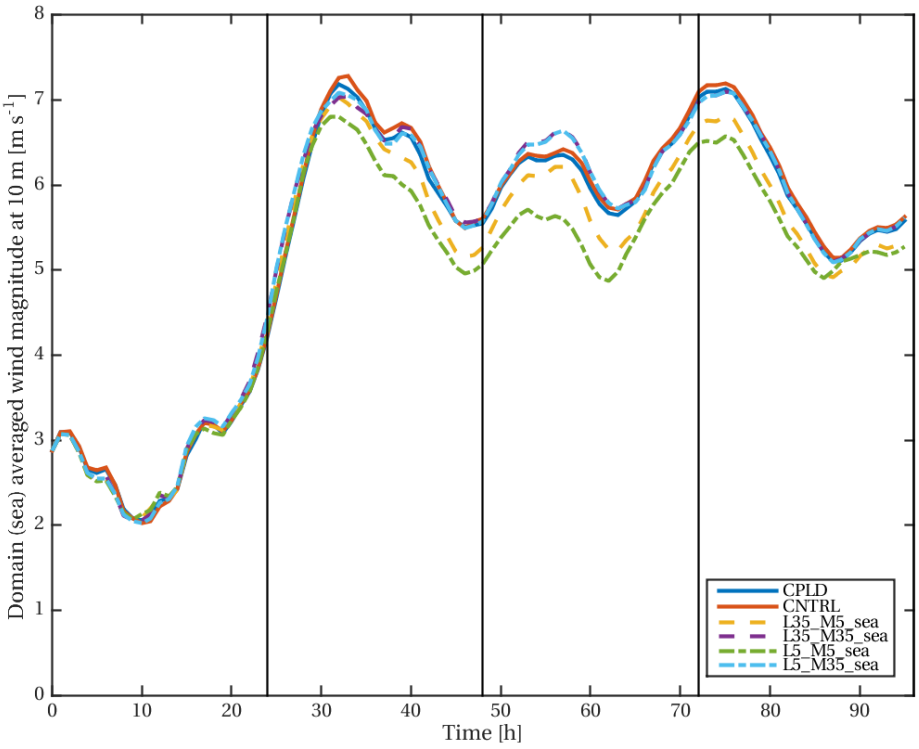

Figure 4.6: Horizontal average over the sea of the wind magnitude at 10 m over the sea as a function of time for some of the simulations.

found for a significantly shallower initial mixed layer (5 meters), suggesting that either the winds are underestimated in WRF and/or the ocean vertical mixing scheme does not perform well under these conditions.

Effects on the precipitation

In figure 4.9, the total rain volume cumulated over the domain on the 9 October is shown as a function of the daily mean (on the 8 October) horizontal average SST over the Ligurian sea for all the simulations considered, namely CNTRL, CPLD, UNIF and L*_M*_sea with $L \in [5, 35]$ m and $M \in [5, 10, 15, 20, 25, 30, 35]$ m. There is a clear increase in the total precipitation with increasing average SST, as known from Pastor et al. (2001); Lebeaupin et al. (2006). The underlying trend is estimated to be roughly 1×10^8 m^3 K^{-1}, which, in percentage, means that per each degree the total cumulated rain changes by roughly 10%, in agreement with the findings of Lebeaupin et al. (2006). Since this trend appears to be robust, it is used to find an estimate of the uncertainty on

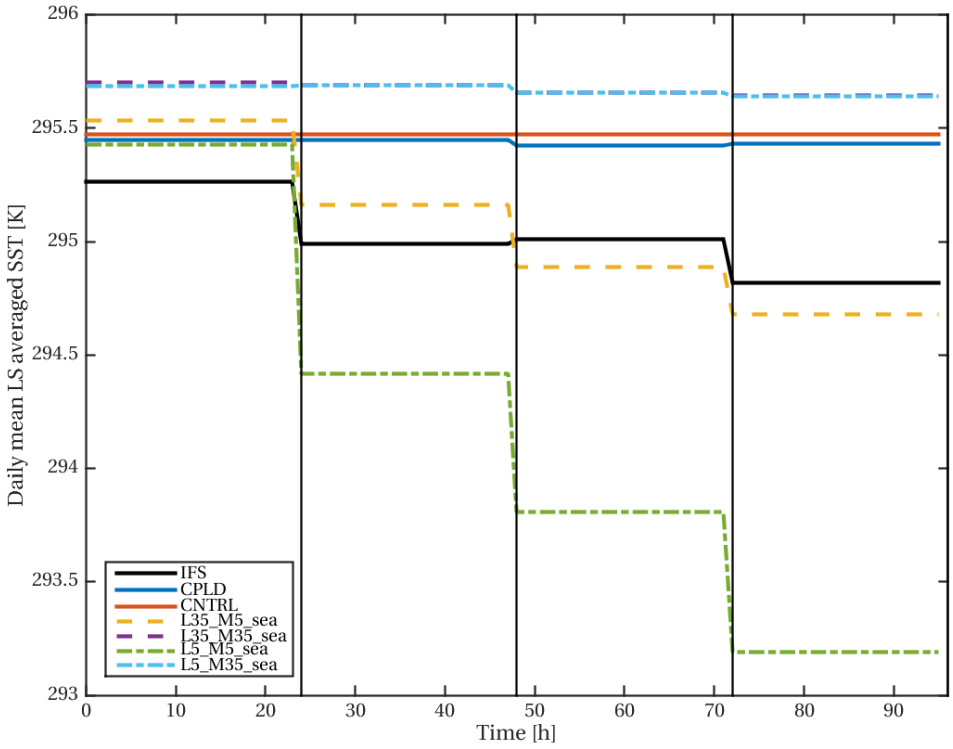

Figure 4.7: Daily mean of the horizontal average of the SST over the Ligurian sea (LS) as a function of time for some of the simulations.

the rain volume as follows. Consider all the data with SST in the interval [295.5, 295.7] K. Since their standard deviation $\sigma_{rv} = 2 \times 10^7$ m^3 is larger than the linear increase due to the background trend in the aforementioned temperature interval, this is taken as an estimate of the spread of the value of the rain volume around the background trend and corresponds to a relative uncertainty of roughly 3%.

The slight decrease in precipitation between the CNTRL and CPLD simulations, roughly 2%, thus falls within the uncertainty and is not significant, confirming that the coupled dynamics is not important in this case study. Instead, considering the series of simulations with $L = 35$ m, the reduction of cumulated rain of the case L35_M5_sea with respect to the CNTRL case is around 13%, while for $L = 5$ m, in the case L5_M5_sea the reduction is roughly 20%. The cases with the lowest precipitation are the ones where the initial MLD is the shallowest, namely $L = 5$ m, which are also the cases with lowest average SST.

Therefore, the different initial vertical thermal structures respond to the intense wind forcing preceding the HPE in different ways, generally reducing the SST in the area in

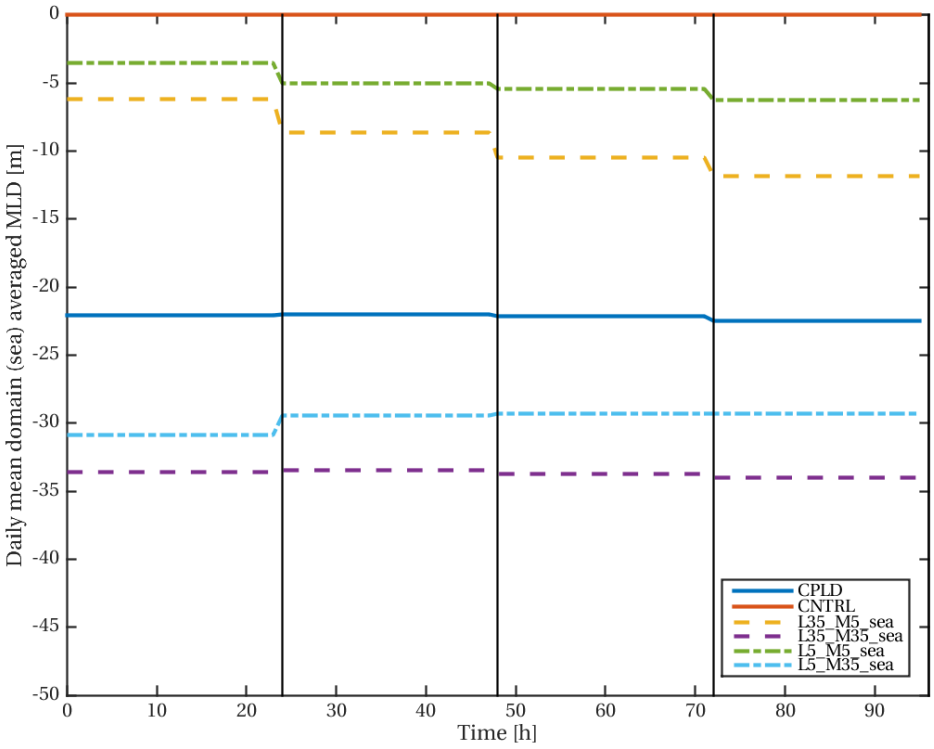

Figure 4.8: Daily mean of the horizontal average of the MLD over the sea as a function of time for some of the simulations.

the vicinity of the convective rain event, which reduces the air column instability and its ability to produce intense rainfalls. This is proved by figure 4.10, where the maps of the convective available potential energy (CAPE), introduced in section 1.1, of the surface air parcel at 0000 UTC 9 October 2014, the midnight before the HPE, are shown for two different simulations, L5_M5_sea in the left panel and L5_M35_sea in the right one. The CAPE is here calculated as the integral of the difference between the adiabatic lifted surface air parcel temperature profile and the local temperature profile between the level of free convection and the equilibrium level of the surface air parcel itself. From figure 4.10, it is clear that, for a shallow initial mixed layer ($M = 5$ m, left panel) the CAPE is strongly reduced with respect to a case with a deeper one ($M = 35$ m, right panel).

A closer look at the data of figure 4.9, then, suggests that when the initial MLD is 25 meters or deeper, the average SST is independent of the exact oceanic vertical thermal structure, as indicated by the very similar value of SST for the cases L5_M25, L5_M30, L5_M35, L35_M25, L35_M30, L35_M35, UNIF. This is indicative of a sort

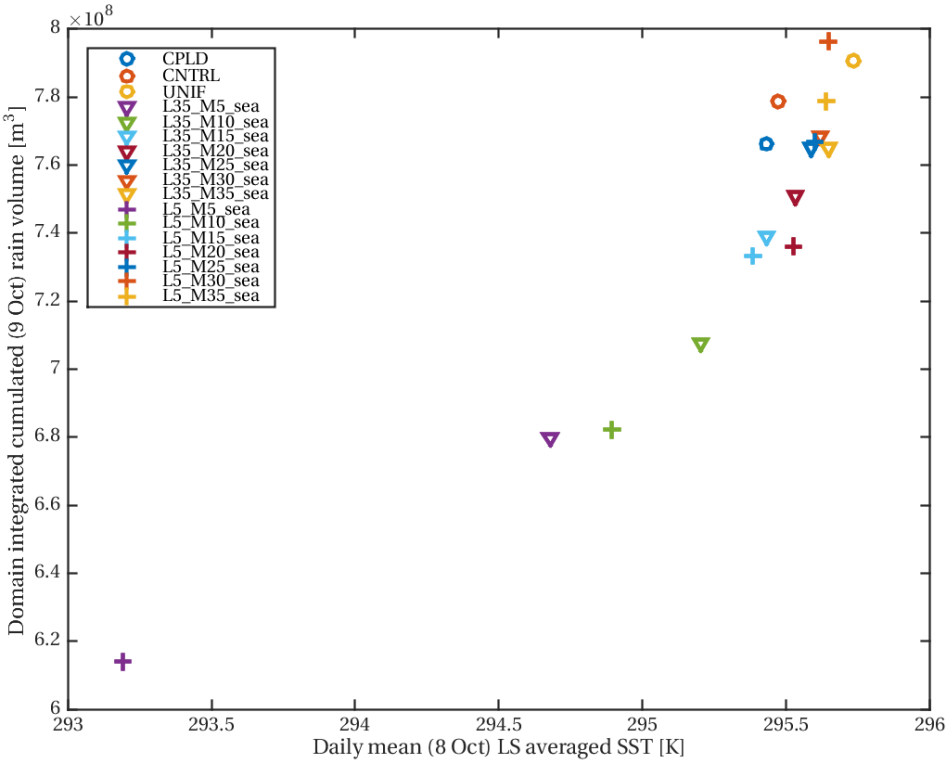

Figure 4.9: Domain integrated rain volume cumulated on the 9 October as a function of the SST averaged on the Ligurian sea on the 8 October.

of threshold behaviour of the total precipitation as a function of the initial MLD, via the control of the average SST. In fact, when looking at the rain volume cumulated on the 9 October as a function of the initial MLD, as in figure 4.11, it is easy to see that the rain volume increases, at first, and then saturates around $M = 25$ m. The differences between the two series with different values of stratification, L, are within the uncertainty estimated above (except for the case $M = 5$ m) and thus are thought to be caused by some secondary mechanisms.

For example, this might be due to the presence of sharper horizontal SST gradients in the case of small L, which are the subject of the previous chapter and are not discussed here further. In fact, imposing a shorter e-folding length L in the initial temperature profile corresponds to increase the stratification at the base of the mixed layer. This means that, on the one hand, it is harder to mix the water column, because of the stronger vertical density gradient to overcome, but on the other hand, when the wind is intense enough, the mixing results in a stronger surface cooling. Since the winds are not homogeneous over the sea, but have a rapidly-changing spatial structure with localized

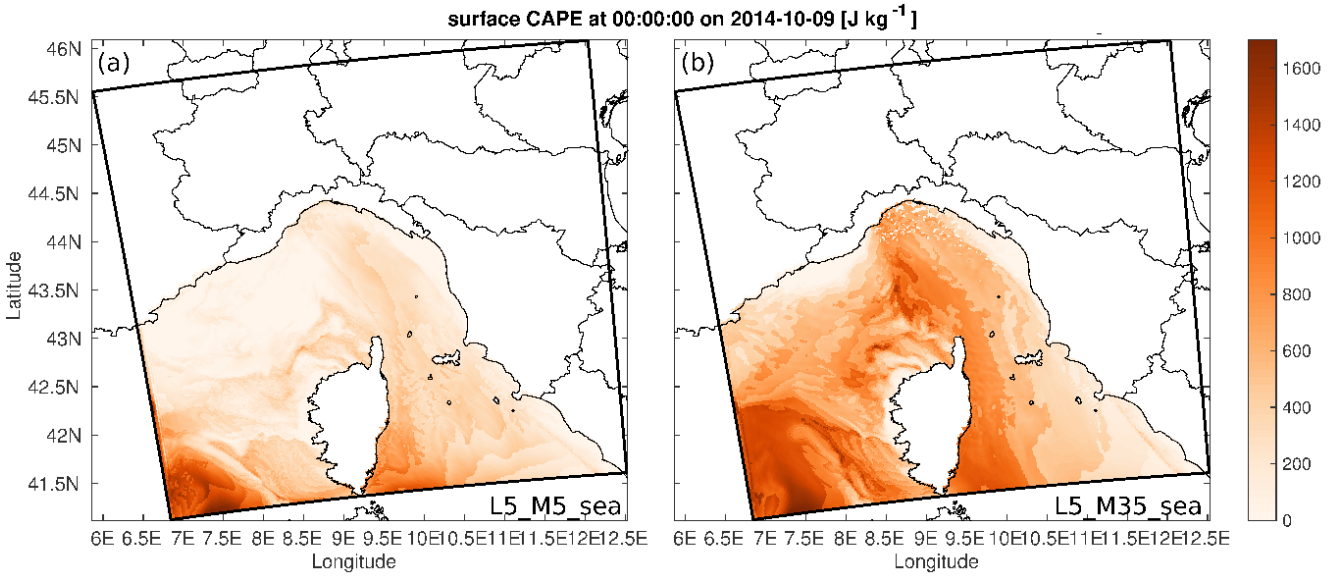

Figure 4.10: Snapshot of the CAPE [J kg^{-1}] at 0000 UTC 9 October 2014 from the simulations L5_M5_sea (shallow mixed layer) in panel (a) and L5_M35_sea (deep mixed layer) in panel (b).

gusts, those two effects combined induce relatively sharper horizontal gradients in the SST field after few days from the initialization in the simulation with relatively stronger stratification. Figure 4.12 shows it, by displaying the SST field at 0000 UTC 9 October 2014 from the simulations L35_M25_sea (a) and L5_M25_sea (b). Starting from the same MLD, $M = 25$ m, it is possible to see that for stronger stratification (small L), the horizontal SST gradients are sharper.

4.5 Discussion and conclusions

The mechanism through which the thermal vertical oceanic structure can control the precipitation of a HPE is found to be the following. For a shallow oceanic mixed layer, the intense winds of the synoptic system that drives the heavy-rain-producing MCS are able to entrain deep and cold water in the mixed layer, resulting in a substantial reduction of the average SST in the region near the HPE, of the order of 1°C. This does not happen if the initial mixed layer is deep enough so that the effect of the winds is to mix water within the mixed layer itself. The change in SST, then, is known to control the amount of precipitation (Pastor et al., 2001; Lebeaupin et al., 2006), through, for example, changes in the air column stability.

This suggests that the reason why the coupling with the ocean seems to be totally ineffective in the case study considered is because the MLD in the coupled simulation is

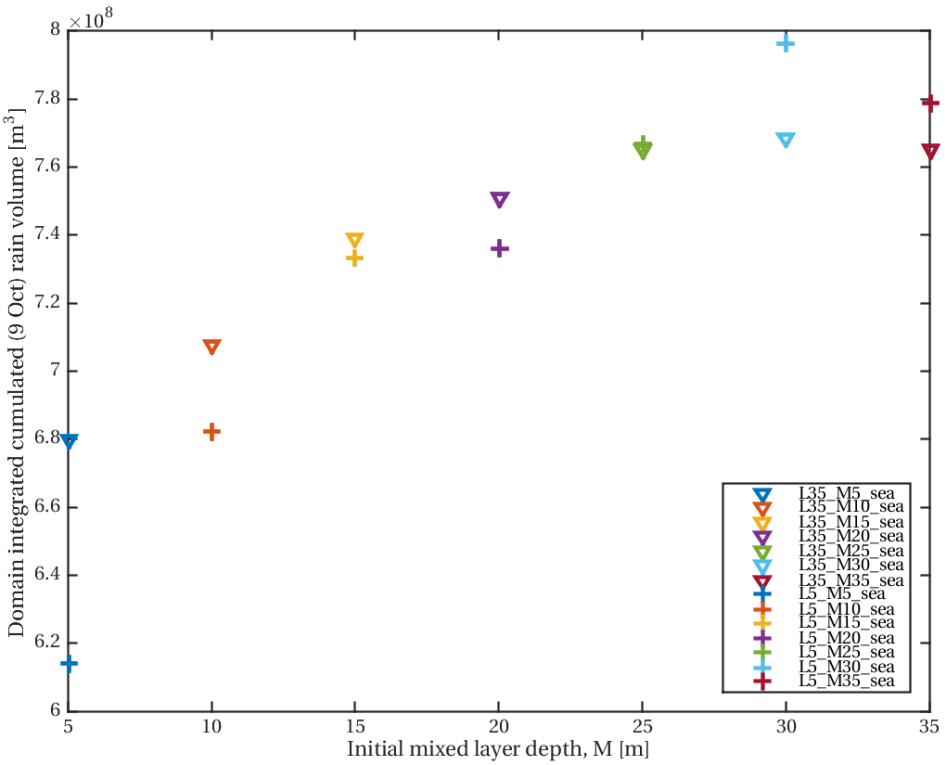

Figure 4.11: Rain cumulated over 24 h on the 9 October and integrated over the domain as a function of the initial mixed layer depth M. The uncertainty is estimated to be $\sigma_{rv} = 2 \times 10^7$ m^3 (see text for details).

deep enough to insulate the colder and deeper water from the mixing action of the winds. Thus, since in the coupled simulation (CPLD) the reduction of the SST with respect to the uncoupled one (CNTRL) is very small, the difference in total precipitation between a case with a fully resolved three dimensional ocean dynamics and a case with a time independent SST forcing field appears to be negligible. The coupling with the ocean dynamics is more important in the case of shallower mixed layer, as the series of simulations forced with simple vertical temperature profiles, L*_M*_sea, shows. Reductions of the total precipitation of roughly 20% are found in the shallowest mixed layer cases, indicating that the vertical thermal structure of the ocean can considerably reduce the amount of rainfall in such HPEs, in specific conditions.

The MLD threshold value that determines whether the ocean dynamics is important or not depends on the magnitude of the winds of the system considered. In this case study, the intense surface winds of the synoptic system driving the HPE have a spatial average magnitude of 6.5 m s^{-1}, with local peak values of the order of 20 m s^{-1}. In other

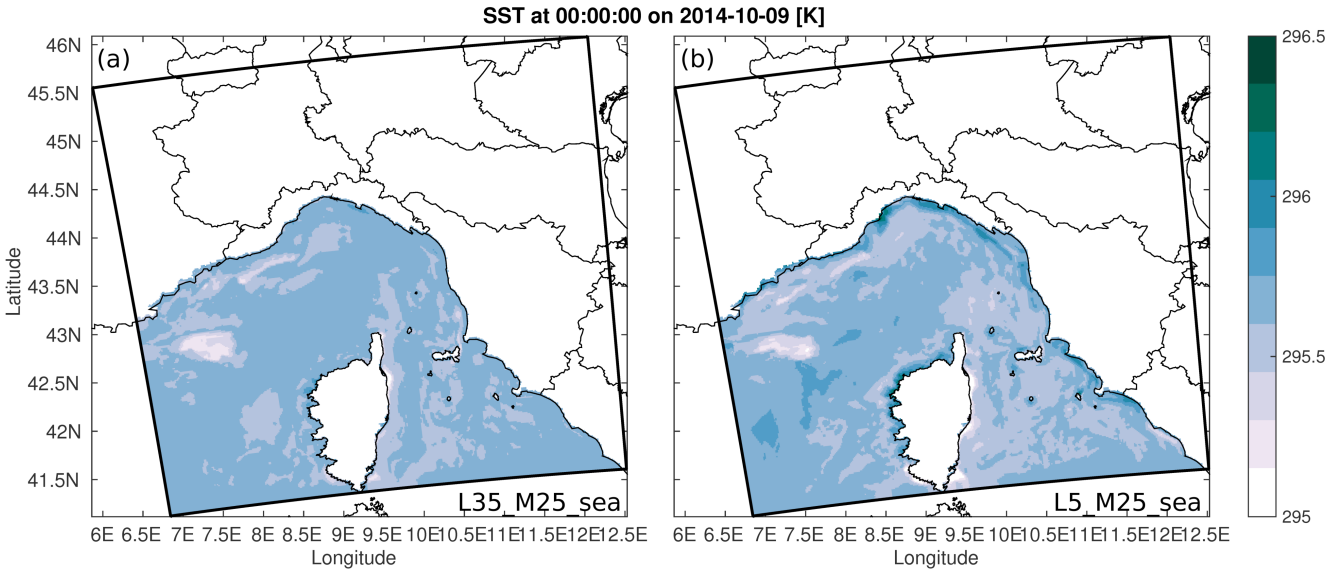

Figure 4.12: Snapshot of the SST [K] at 0000 UTC 9 October 2014 from the simulations L35_M25_sea (weaker stratification) in the left panel and L5_M25_sea (stronger stratification) in the right panel.

HPEs along the coasts of the western Mediterranean, e.g. those described in Lebeaupin et al. (2006), the low-level jet has been observed to reach wind speed of roughly 30 m s^{-1}, suggesting that the range of parameters involved in the mechanism described extends to even stronger wind events.

The conditions that maximize the mitigating effect of the ocean dynamics on the precipitation in such HPEs are typical of the end of the summer, when the first cyclones arrive in the area. In fact, when the ocean has been heated up by the strong summer solar heat flux, it has a shallow mixed layer and a strong stratification beneath it (D'Ortenzio et al., 2005; Houpert et al., 2015). In such conditions, the strong winds associated with the heavy-rain-producing MCS can mix up cold water, that is relatively close to the surface, and the colder SST can feedback on the MCS, reducing its instability and, thus, the total cumulated rain. When, then, in autumn, stronger winds deepen the mixed layer, the ability of the sea to reduce the lower atmosphere instability through a colder SST is attenuated. As a consequence, this might partially explain the timing of such HPEs, which do not generally happen right at the end of the summer, but in mid and late autumn. To test that this is the case, it is indeed desirable to do similar analysis on other case studies, with different synoptic conditions and different upper ocean thermal structure.

Further analysis could be also performed on the heat fluxes, due to their importnace in the SST-wind relationship studied in chapter 3. Take, for example, the sensible heat

flux, which is proportional to the air-sea temperature difference and the surface wind speed. At a sharp SST front, say from cold to warm, the increase in sea temperature firstly determines an increase in heat flux. This drives, then, an increase in surface speed, due to the DMM mechanism, which contributes to keep the heat flux high, even if the temperature difference is decreasing. Then, because of the heat flux itself, the air-sea temperature difference goes to zero, suppressing the heat flux consequently. In such a picture, supposing that the wind is strong enough to entrain cold water from the base of the mixed layer, the role of the ocean dynamics would be to reach the zero air-sea temperature difference faster, leading to a faster equilibration of the system and a reduced net heat flux from the ocean to the atmosphere. But in order to study such a mechanism, an idealized setup similar to the one used by Skyllingstad et al. (2007) would be more appropriate to the one described in the thesis.

Although, it is planned for future work to extend the spatial correlation analysis described in chapter 3 to the heat fluxes to shed light on the importance of the increase in surface speed following the DMM mechanism in the control of the heat fluxes themselves. In particular, always having the sensible heat flux in mind, this can be accomplished by comparing the product of the surface wind speed and the air-sea temperature difference taken from different simulations. For example, if the quantity $u_{10}^{\mathrm{CNTRL}}\Delta T^{\mathrm{CNTRL}}$ is proportional to the heat flux from the CNTRL simulation, with u_{10} being the magnitude of the surface wind and ΔT the air-sea temperature difference, the quantity $u_{10}^{\mathrm{UNIF}}\Delta T^{\mathrm{CNTRL}}$ would be the equivalent of the heat flux where the winds are unaware of the SST structure. Thus, introducing the appropriate temporal and spatial averages, this would show how much the DMM is important in the determination of the sensible heat flux. A similar reasoning could be done for the moisture flux (intimately related to the latent heat flux), which is proportional to the surface wind speed and the difference in water vapor saturation pressure of the surface air and at the sea surface temperature.

Finally, it is important to underline that this work was not intended to improve the forecast of these heavy-rain-producing MCSs, but to understand more about the importance of the vertical thermal structure of the upper ocean in the control of such HPEs. This is the reason why the analysis of the results are not invalidated by some of the biases of the model, such as the absence of rain over the sea on the 9 of October or the underestimation of the surface cooling in the coupled ocean-atmosphere simulation with respect to what happened in reality. In fact, the reasons for such biases are known (choice of initialization and difficulty to resolve the wind gusts or vertical mixing parameterization), as explained in the previous sections, and do not affect the mechanism described above.

Five

Conclusions

5.1 Oceanic internal wave interactions in the wake of a tropical cyclone

An outstanding question in physical oceanography is how the internal wave energy is transferred to the molecular scales, where mixing happens and energy is effectively dissipated. In particular, internal wave breaking is thought to be important in the interior of the ocean, far from the surface layer, where wind-induced turbulence efficiently mixes the upper ocean, and far from the bottom topography, which is known to produce large amount of three-dimensional turbulence, through interactions with tides (Ferrari and Wunsch, 2009). Internal waves are thought to be a key factor in the ocean interior mixing, because, when they are characterized by strong vertical shear, they trigger instabilities that generate overturning across the density surfaces and, thus, small-scale mixing (Staquet and Sommeria, 2002). Among the sources of internal waves there are, indeed, tropical cyclones, which, even if intermittent in space and time, with their extremely intense winds are known to produce a three-dimensional baroclinic internal wave wake that radiates energy in the ocean interior (Price, 1981; Gill, 1984). The importance of the spectral characterization of this energy input in the ocean by the wind forcing, both in terms of frequency and in terms of vertical wavenumber, is in the dependence of the energy propagation speed on such spectral features (Niwa and Hibiya, 1997). Low vertical mode waves propagate faster than high vertical mode ones and superinertial frequency waves are likely to propagate further than near-inertial ones, because they are less inclined to undergo critical latitude reflection.

In order to better constrain the extent and the velocity of the energy propagation from the tropical cyclone track, thus, in chapter 2, a new analytical description of the energy exchanges among internal waves in the baroclinic wake is introduced.

With respect to previous works on the same topic (Niwa and Hibiya, 1997; Danioux and Klein, 2008; Zedler, 2009) a realistic ocean stratification and a detailed decomposition of internal modes enable to describe in details all the possible energy exchanges among modes and frequencies, with a set of coefficients defined analytically from the equations of motion. This, in turns, allows to identify an achievable pathway for the energy to cascade from the large scales, typical of the atmospheric forcing, to the dissipative

scales in a location far from the wave generation site.

Through the internal mode decomposition of the equations of motion in the spectral space, the steady state solution for the linear problem is found analytically. The nonlinear advective terms, then, act as forcing in the spectral domain and bring to or remove energy from the double inertial peak of the lowest internal mode waves. Multiple wave interactions (with three or five modes involved) are associated with energy transfer coefficients and it is found that the energy transfer across modes is dominated by the advection of some high mode waves by the second or third mode waves, which are the most energetic in the near-inertial range.

In particular, it is shown that for typical values of tropical cyclone parameters (in terms of dimension, translation speed and ocean stratification), the transfer of energy from some high vertical mode near-inertial range to a lower vertical mode double inertial range generally corresponds to an increase in the horizontal energy propagation speed. Since superinertial waves can propagate further than near-inertial ones, this suggests that by including the nonlinear terms in the equations of motion, the energy input by the wind stress can propagate faster and further with respect to an equivalent simplified linear ocean and, thus, nonlinear effects are relevant for the lateral energy propagation. Moreover, even if the double inertial energy fraction is small with respect to the near-inertial one, its generation is found to be a crucial step in the energy cascade towards the dissipative scales, in agreement with other recent theoretical and modeling works (Wagner and Young, 2016; Sutherland, 2016).

Further developments of the theory might include the presence of spatially varying bottom topography, which would modify the vertical structure of the modes, and the time evolution of the transient oceanic response that leads to the steady state considered in the analysis presented in this thesis. In fact, the analytical coefficients that measure the transfer of energy among waves are found for the oceanic response steady state solution with a tropical cylone moving at constant speed along a straight line. Real tropical cyclones are observed to change their intensity, mainly according to the upper ocean thermal state (Mei et al., 2015), and their propagation speed and direction, following the large-scale atmospheric circulation (Emanuel, 2003). Thus, it would be interesting to investigate the time scales needed to achieve the steady state solution described here, to understand more precisely in which conditions it is relevant. The comparison between the steady state analytical linear solution and the fully nonlinear time dependent one for the internal wave wake shows good agreement between the two and seems to indicate that transient behaviors decay on scales of the order of a day.

Analysis of observations of current data taken from a mooring in the western Atlantic at roughly 16° North show a significant increase in the near-inertial energy range following the passage of tropical cyclones in the region (Köhler et al., 2018). Preliminary analysis on the same data set do not disagree with the possibility of faster propagating double inertial internal waves, but more work is needed to test its significance. Transient features might be important, as well as interactions with the mean oceanic circulation, that were excluded from the theoretical analysis of the present work.

5.2 Importance of the upper ocean thermal state on heavy-rain-producing MCS dynamics

Heavy-rain-producing mesoscale convective systems (MCSs), as introduced in chapters 3 and 4, are meteorological phenomena characterized by very intense rain rates that release significant fractions (of the order of one third) of the local yearly rainfall amount and are not rare along the coasts of the Mediterranean sea (Dayan et al., 2015). This tipically triggers an intense hydrological response that can cause significant economical damages and, in the worst case, some casualties (Nuissier et al., 2008; Ducrocq et al., 2014). The formation of these MCSs is conditioned to the occurrence of four simultaneous factors: a slowly evolving synoptic structure, the presence of atmospheric conditionally instability, high low-level moisture content and a mesoscale lifting trigger (Nuissier et al., 2008).

It has been known for many years that the mean sea surface temperature (SST) affects the total precipitation volume of the MCSs: the warmer the sea, the more it rains (Pastor et al., 2001; Lebeaupin et al., 2006). In this thesis, the focus has been on the role that the SST patterns with spatial scales of the order of $O(1-10$ km) and the upper ocean thermal vertical structure have on these heavy precipitation events. It is found that total precipitation is not affected by horizontal SST fine structure, but this can affect the location of the heavy rain, by controlling the spatial pattern of surface wind convergence. As for the upper ocean thermal vertical structure, it is found that in particular conditions it can enhance the atmospheric surface layer stability and, thus, supress deep convection. To understand the physical processes at play, different sets of atmosphere-only and coupled ocean-atmosphere numerical simulations are run with state-of-the-art numerical models in a midlatitudes realistic setup leading to the development of a heavy-rain-producing MCS, the 9 October 2014 Genoa case, in northwestern Italy (Fiori et al., 2017).

In the first place, in chapter 3, spatial correlation analysis between the appropriate time averaged variables is used to assess the relative importance of the mechanisms controlling the SST-wind relationship (Small et al., 2008). In particular, time averages of surface wind magnitude, SST, surface wind convergence, downwind SST gradient and SST laplacian are considered. The two principal mechanisms controlling the SST-wind relationship are a downward momentum mixing (DMM) mechanism (Wallace et al., 1989; Hayes et al., 1989) and a pressure adjustment (PA) one (Lindzen and Nigam, 1987). According to the former, when an air parcel crosses a SST front from a cold region to a warm one, the instability associated with the enhanced heat fluxes on the warm side of the front leads to stronger vertical turbulent mixing that accelerates the surface flow by bringing momentum from the relatively faster upper layers. Thus, in correspondence of the front, when going from cold to warm (warm to cold) a band of local divergence (convergence) is generated. Instead, according to the latter mechanism, an increase in SST leads to a surface pressure low that drives local convergence. Therefore, surface wind convergence is associated with areas of local maximum of SST.

Atmospheric numerical simulations are run with different SST forcing fields in order to explore the effects of changing the intensity of the SST gradients and their character-

istic length scales. With respect to previous observational and modeling studies, that have focused either on climatological time scales (Chelton and Xie, 2010) or on idealized settings with simple geometrical SST structures (Skyllingstad et al., 2007; Spall, 2007), the present work focuses on realistic SST spatial structures of the order of $O(1-10$ km) and O(hours) time scales.

It is found that there is a significant atmospheric response, on the spatial and temporal scales considered, dominated by the DMM mechanism. This, by affecting the position of the surface convergence lines, is also found to be likely to affect the position of the rain bands, with possible horizontal displacements of the order of tens of km. The precise conditions for which such rain band displacements take place are still to be determined, because there are cases where the position of the convergence line is likely to be controlled by the atmospheric large-scale dynamics, that leads to the formation of a thick layer of cold and dry air that acts as a virtual orographic barrier for the warm low-level jet. It is thought that the strong stability associated with this kind of stratification might be too hard to be eroded throught the DMM mechanism and, thus, the SST structure would have a negligible effect on the surface convergence spatial patterns (Fiori et al., 2017).

As explored in chapter 4, then, another way through which the ocean can influence the dynamics of the MCSs is the suppression of the air column conditional instability by reduction of the heat fluxes at the air-sea interface. This is found to happen as a consequence of the vertical oceanic mixing due to the action of the intense surface winds associated with the large-scale atmospheric structure in which the MCS is embedded. Previous works have studied the effects of intense wind events on the subsequent develoment of a heavy-rain-producing MCS (Lebeaupin Brossier et al., 2013), in a situation where the two events are indipendent from an atmospheric point of view. There, it is only through the ocean thermal memory that the wind-induced vertical mixing, with its subsequent surface cooling, can suppress the air column instability.

In the present thesis, two series of coupled atmosphere-ocean simulations with different initial mixed layer depth and underlying stratification are run. It is found that in particular conditions, where the surface mixed layer is shallow and the stratification is strong, which are typical of the late summer period, the winds of the large-scale system feeding the MCS can produce a relatively large vertical mixing so that the SST is cooled down enough (with variations of the order of 1 K) to inhibit atmospheric convection. Colder SST is known to induce colder and drier surface air, which is associated with lower values of convective available potential energy and, thus, less precipitation (Lebeaupin et al., 2006). This might be one among other factors explaining why MCSs generally develop in late autumn, when the oceanic mixed layer is deeper than at the end of the summer, because of the action of intense winds, typical of this season.

Future developments might include the extension of the present analysis to other case studies in order to expand the set of dynamical atmospheric and oceanic conditions explored and to further generalize the results. In particular, this might shed light on the relative importance of the DMM mechanism with respect to the large-scale dynamics in the control of the position of the convergence line that triggers the deep convection.

Moreover, it would be interesting to test whether a similar process is relevant for the intense precipitations over land, with the role played by the SST spatial structures being played by the soil temperature patterns. A possible extension of the analysis in this direction might be relevant to understand the observed larger precipitation amounts on the leeward side of cities, which are known to create warm surface anomalies and, thus, to affect the planetary boundary layer stability.

Ringraziamenti

Ci sono molte persone che vorrei ringraziare per aver contribuito in tanti modi diversi ad aver reso questi anni di dottorato così ricchi e interessanti.

Sicuramente, sono molto riconoscente a Claudia, per essere sempre stata di supporto, con lo spirito costruttivo che la contraddistingue, che aiuta a non affondare nei momenti più complicati e suggerisce l'entusiasmo al momento giusto. Mi ha insegnato tanto e mi ha davvero permesso di fare esperienze diverse, girare un po' il mondo e capire cosa significhi fare ricerca.

For all the technical skills that I've learned in the use of the numerical models, I certainly owe many thanks to Madeline, Antonio and Lionel, who, in different parts of the world have taught me a lot. I also would like to thank Alex Hall for the possibility of visiting his group in UCLA and Eli Tziperman for the work that we've done together.

This last year, I've had the chance to go to the GFD summer program at WHOI and I surely want to acknowledge the staff of the school, in particular Claudia Cenedese, Bruce Sutherland and Craig McConnochie, for the rich summer that we've spent together doing science and melting ice. Not only the school, but also the people have been great, Madi, Thomasina, Earle, Robert, Eric, Margaret, thanks.

Indubbiamente, questo dottorato non sarebbe stato lo stesso senza gli insostituibili compagni di ufficio, prima Valentina e Fabio e, poi, Francesco e Giulia. Ho quasi capito che il fondale oceanico non è piatto ma soprattutto che il supporto morale, le risate, le discussioni, il confronto, i pranzi in compagnia rendono il tutto un po' più bello. Non vuol dire che chi sta in un altro ufficio, poi, sia da ringraziare meno, Luca, Chiare, Mostafa, Giovanni, Sara, grazie. I vostri spunti, idee, inviti sono sempre molto graditi.

Poi ci sono i tanti preziosi colleghi e amici incontrati qui e lì nelle varie attività di ricerca. Vorrei ringraziare, in particolare, Francesca per l'ospitalità a Savona e le avventure (gastronomiche) in giro per il mondo e Marta per aver tentato di imparare con me a giocare a Cirulla, the friends from LA, Max, Chantelle, Jowaan for the invaluable time spent together e l'equipaggio della R/V Minerva Uno, che mi ha fatto vedere il mare. Quello vero.

Mentre uscendo dall'università, un profondo grazie va ai miei imprevedibili coinquilini, Orio, Ste, Hasan, Noor, Eli, con cui ogni giorno c'è qualcosa di nuovo da mettere in padella e condividere. Non meno sentito, chiaramente, è il grazie per gli amici, che in un modo o nell'altro ci sono sempre, Alby, Davide, Giorgio, Richi e tutti gli altri sparsi in giro per il mondo.

Infine, ultima ma non meno importante, la mia bella famiglia che non smette mai di soprendermi. Mamma, papà, Agni, Bea, siete unici.

Bibliography

Arfken, G. B., and H. J. Weber, 2006: *Mathematical methods for physicists*. 6th ed., Elsevier Academic Press, 1182 pp.

Beckmann, A., and D. B. Haidvogel, 1993: Numerical simulation of flow around a tall isolated seamount. part I: Problem formulation and model accuracy. *J. Phys. Oceanogr.*, **23**, 1736–1753, doi:10.1175/1520-0485(1993)023<1736:NSOFAA>2.0.CO;2.

Beljaars, A. C. M., 1994: The parameterization of surface fluxes in large-scale models under free convection. *Quart. J. Roy. Meteor. Soc.*, **121**, 255–270.

Berthou, S., S. Mailler, P. Drobinski, T. Arsouze, S. Bastin, K. Béranger, and C. Lebeaupin Brossier, 2015: Sensitivity of an intense rain event between atmosphere-only and atmosphere-ocean regional coupled models: 19 september 1996. *Quart. J. Roy. Meteor. Soc.*, **141**, 258–271, doi:10.1002/qj.2355.

Black, W. J., and T. D. Dickey, 2008: Observation and analysis of upper ocean responses to tropical storms and hurricanes in the vicinity of Bermuda. *J. Geophys. Res.*, **113**, C08009, doi:10.1029/2007JC004358.

Bretherton, C. S., M. Widmann, V. P. Dymnikov, J. M. Wallace, and I. Bladé, 1999: The effective number of spatial degrees of freedom of a time-varying field. *J. Climate*, **12**, 1990–2009.

Buzzi, A., S. Davolio, P. Malguzzi, O. Drofa, and D. Mastrangelo, 2014: Heavy rainfall episodes over Liguria in autumn 2011: numerical forecasting experiments. *Nat. Hazards Earth Sys. Sci.*, **14 (5)**, 1325–1340, doi:10.5194/nhess-14-1325-2014.

Carniel, S., A. Benetazzo, D. Bonaldo, F. M. Falcieri, M. M. Miglietta, A. Ricchi, and M. Sclavo, 2016: Scratching beneath the surface while coupling atmosphere, ocean and waves: analysis of a dense water formation event. *Ocean Model.*, **101**, 101–112, doi:10.1016/j.ocemod.2016.03.007.

Cassola, F., F. Ferrari, and A. Mazzino, 2015: Numerical simulations of Mediterranean heavy precipitation events with the WRF model: a verification exercise using different approaches. *Atmos. Res.*, **164-165**, 210–225, doi:10.1016/j.atmosres.2015.05.010.

Cassola, F., F. Ferrari, A. Mazzino, and M. M. Miglietta, 2016: The role of the sea in the flash floods events over Liguria (northwestern Italy). *Geophys. Res. Lett.*, doi: 10.1002/2016GL068265.

Chang, S. W., and R. A. Anthes, 1978: Numerical simulations of the ocean's nonlinear, baroclinic response to translating hurricanes. *J. Phys. Oceanogr.*, **8**, 468–480.

Chappell, C., 1986: Quasi-stationary convective events. *Mesoscale meteorology and forecasting*, P. S. Ray, Ed., American Meteorological Society: Boston, 289–310.

Chelton, D. B., and S.-P. Xie, 2010: Coupled ocean-atmosphere interaction at oceanic mesoscales. *Oceanography*, **23 (4)**, 52–69.

Chelton, D. B., and Coauthors, 2001: Observations of coupling between surface wind stress and sea surface temperature in the eastern tropical Pacific. *J. Climate*, **14**, 1479–1498, doi:10.1175/1520-0442(2001)014<1479:OOCBSW>2.0.CO;2.

Chou, M. D., and M. J. Suarez, 1999: A solar radition parameterization for atmospheric studies. *NASA Tech. Memo. 104606*, **15**, 40 pp.

Chou, M. D., M. J. Suarez, X. Z. Liang, and M. M. H. Yan, 2001: A thermal infrared radiation parameterization for atmospheric studies. *NASA Tech. Memo. 104606*, **19**, 68 pp.

Danioux, E., and P. Klein, 2008: A resonance mechanism leading to wind-forced motions with a $2f$ frequency. *J. Phys. Oceanogr.*, **38**, 2322–2329.

D'Asaro, E. A., E. B. Sanford, P. P. Niiler, and E. J. Terrill, 2007: Cold wake of hurricane Frances. *Geophys. Res. Lett.*, **34**, L15609, doi:10.1029/2007GL030160.

Davolio, S., A. Volonté, A. Manzato, A. Pucillo, A. Cicogna, and M. E. Ferrario, 2016: Mechanisms producing different precipitation patterns over north-eastern Italy: insights from HyMeX-SOP1 and previous events. *Quart. J. Roy. Meteor. Soc.*, doi: 10.1002/qj.2731.

Dayan, U., K. Nissen, and U. Ulbrich, 2015: Review article: atmospheric conditions inducing extreme precipitation over the eastern and western Mediterranean. *Nat. Hazards Earth Sys. Sci.*, **15**, 2525–2544, doi:10.5194/nhess-15-2525-2015.

De Szoeke, S. P., and C. S. Bretherton, 2004: Quasi-Lagrangian large eddy simulations of cross-equatorial flow in the East Pacific atmospheric boundary layer. *J. Atmos. Sci.*, **61 (15)**, 1837–1858.

De Zolt, S., P. Lionello, A. Nuhu, and A. Tomasin, 2006: The disastrous storm of 4 November 1966 on Italy. *Nat. Hazards Earth Sys. Sci.*, **6**, 861–879, doi:10.5194/nhess-6-861-2006.

Debreu, L., P. Marchesiello, P. Penven, and G. Cambon, 2012: Two-way nesting in split-explicit ocean models: algorithms, implementation and validation. *Ocean Modelling*, **49**, 1–21.

D'Ortenzio, F., D. Iudicone, C. de Boyer Montegut, P. Testor, D. Antoine, S. Marullo, R. Santoleri, and G. Madec, 2005: Seasonal variability of the mixed layer depth in the Mediterranean Sea as derived from in situ profiles. *Geophys. Res. Lett.*, **32**, L12605, doi:10.1029/2005GL022463.

Ducrocq, V., O. Nuissier, D. Ricard, C. Lebeaupin, and T. Thouvenin, 2008: A numerical study of three catastrophic precipitating events over southern France. II: Mesoscale triggering and stationarity factors. *Quart. J. Roy. Meteor. Soc.*, **134**, 131–145, doi:10.1002/qj.199.

Ducrocq, V., and Coauthors, 2014: HyMeX-SOP1. The field campaign dedicated to heavy precipitation and flash flooding in the northwestern Mediterranean. *Bull. Amer. Meteor. Soc.*, 1083–1100, doi:10.1175/BAMS-D-12-00244.2.

Dudhia, J., 1996: A multi-layer soil temperature model for MM5. *The sixth PSU/NCAR Mesoscale Model users' workshop.*

Dufforg, F., and V. Ducrocq, 2011: Origin of the moisture feeding the heavy precipitating systems over southeastern France. *Nat. Hazards Earth Sys. Sci.*, **11**, 1163–1178, doi:10.5194/nhess-11-1163-2011.

Eden, C., 2011: A closure for meso-scale eddy fluxes based on linear instability theory. *Ocean Model.*, **39(3-4)**, 362–369.

Eden, C., 2012: Implementing diffusivities from linear stability analysis in a three-dimensional general circulation ocean model. *Ocean Model.*, **7-58**, 15–28.

Emanuel, K. A., 2003: Tropical cyclones. *Annu. Rev. Earth Planet. Sci.*, **31**, 75–104, doi:10.1146/annurev.earth.31.100901.141259.

Faccini, F., F. Luino, G. Paliaga, A. Sacchini, and L. Turconi, 2015: Yet another disaster flood of the Bisagno stream in Genoa (Liguria, Italy): October the 9th-10th 2014 event. *Rend. Online. Soc. Geol. It.*, **35**, 128–131, doi:10.3301/ROL.2015.81.

Fairall, C. W., E. F. Bradley, J. E. Hare, A. A. Grachev, and J. B. Edson, 2003: Bulk parameterization of air-sea fluxes: Updates and verification for the COARE algorithm. *J. Climate*, **16**, 571–591, doi:10.1175/1520-0442(2003)016<0571:BPOASF>2.0.CO;2.

Faranda, D., G. Messori, and P. Yiou, 2017: Dynamical proxies of North Atlantic predictability and extremes. *Sci. Rep.*, **7**, doi:10.1038/srep41278.

Ferrari, R., and C. Wunsch, 2009: Ocean circulation kinetic energy: reservoirs, sources and sinks. *Annu. Rev. Fluid Mech.*, **41**, 253–282, doi:10.1146/annurev.fluid.40.111406.102139.

Fiori, E., A. Comellas, L. Molini, N. Rebora, F. Siccardi, D. J. Gochis, S. Tanelli, and A. Parodi, 2014: Analysis and hindcast simulations of an extreme rainfall event in the Mediterranean area: the Genoa 2011 case. *Atmos. Res.*, **138**, 13–29.

Fiori, E., L. Ferraris, L. Molini, F. Siccardi, D. Kranzlmueller, and A. Parodi, 2017: Triggering and evolution of a deep convective system in the Mediterranean Sea: modelling and observations at a very fine scale. *Quart. J. Roy. Meteor. Soc.*, doi:10.1002/qj.2977.

Fiori, E., A. Parodi, and F. Siccardi, 2010: Turbulence closure parameterization and grid spacing effects in simulated supercell storms. *J. Atmos. Sci.*, **67 (12)**, 3870–3890, doi:10.1175/2010JAS3359.1.

Flamant, C., 2003: Alpine lee cyclongenesis influence on air-sea heat exchanges and marine atmospheric boundary layer thermodynamics over the western Mediterranean during a Tramontane/Mistral event. *J. Geophys. Res.*, **108 (C2)**, doi:10.1029/2001JC001040.

Garrett, C., 2001: What is the "near-inertial" band and why is it different from the rest of the internal wave spectrum. *J. Phys. Oceanogr.*, **31**, 962–971.

Garrett, C. J. R., and W. Munk, 1972: Space-time scales of internal waves. *Geophys. Fluid Dyn.*, **3**, 225–264, doi:10.1080/03091927208236082.

Garrett, C. J. R., and W. Munk, 1975: Space-time scales of internal waves: a progress report. *J. Geophys. Res.*, **80**, 291–297.

Garrett, C. J. R., and W. Munk, 1979: Internal waves in the ocean. *Annu. Rev. Fluid Mech.*, **11**, 339–369.

Gaume, E., and Coauthors, 2009: A compilation of data on European flash floods. *J. Hydrol.*, **367**, 70–78.

Geisler, J. E., 1970: Linear theory of the response of a two layer ocean to a moving hurricane. *Geophys. Fluid Dyn.*, **1**, 249–272.

Gerkema, T., L. R. M. Maas, and H. van Haren, 2013: A note on the role of mean flows in Doppler-shifted frequencies. *J. Phys. Oceanogr.*, **43 (2)**, 432–441, doi:10.1175/JPO-D-12-090.1.

Gill, A. E., 1982: *Atmosphere-ocean dynamics*. Elsevier Academic Press, 662 pp.

Gill, A. E., 1984: On the behavior of internal waves in the wakes of storms. *J. Phys. Oceanogr.*, **14**, 1129–1151.

Greatbatch, R. J., 1984: On the response of the ocean to a moving storm: parameters and scales. *J. Phys. Oceanogr.*, **14**, 59–78.

Griesel, A., C. Eden, N. Koopmann, and E. Yulaeva, 2015: Comparing isopycnal eddy diffusivities in the Southern Ocean with predictions from linear theory. *Ocean Model.*, **94**, 33–45.

Hayes, S. P., M. J. McPhaden, and J. M. Wallace, 1989: The influence of sea surface temperature on surface wind in the eastern equatorial Pacific. *J. Climate*, **2**, 1500–1506.

Heywood, K. J., A. C. N. Garabato, and D. P. Stevens, 2002: High mixing rates in the abyssal Southern Ocean. *Nature*, **415**, 1011–1014, doi:10.1038/4151011a.

Hibiya, T., Y. Niwa, K. Nakajima, and N. Suginohara, 1996: Direct numerical simulation of the roll-off range of internal wave shear spectra in the ocean. *J. Geophys. Res.*, **101**, 14 123–14 129.

Homar, V., R. Romero, C. Ramis, and S. Alonso, 2002: Numerical study of the October 2000 torrential precipitation event over eastern Spain: analysis of the synoptic-scale stationarity. *Annales Geophysicae*, **20**, 2047–2066.

Hong, S. Y., and J. O. J. Lim, 2006: The WRF single moment 6-class microphysics scheme (WSM6). *J. Korean Meteorol. Soc.*, **42**, 129–151.

Houpert, L., P. Testor, X. Durrieu de Madron, S. Somot, F. D'Ortenzio, C. Estournel, and H. Lavigne, 2015: Seasonal cycle of the mixed layer, the seasonal thermocline and the upper-ocean heat storage rate in the Mediterranean Sea derived from observations. *Progr. Oceanogr.*, **132**, 333–352, doi:10.1016/j.pocean.2014.11.004.

IPCC, 2012: *Managing the risks of extreme events and disasters to advance climate change adaptation - A special report of working groups I and II of the Intergovernmental Panel on Climate Change*, C. B. Field, V. Barros, T. F. Stocker, D. Qin, D. J. Dokken, K. L. Ebi, M. D. Mastrandrea, K. J. Mach, G.-K. Plattner, S. K. Allen, M. Tignor, and P. M. Midgley, Eds., Cambridge University Press, Cambridge, UK and New York, NY, USA, 582.

IPCC, 2013: *Climate change 2013: The physical science basis. Contribution of working group I to the fifth assessment report of the Intergovernmental Panel on Climate Change*, T. F. Stocker, D. Qin, G.-K. Plattner, M. Tignor, S. K. Allen, J. Boschung, A. Nauels, Y. Xia, V. Bex, and P. M. Midgley, Eds., Cambridge University Press, Cambridge, UK and New York, NY, USA, 1535.

Jackett, D. R., and T. McDougall, 1995: Minimal adjustment of hydrographic profiles to achieve static stability. *J. Atmos. Oceanic Technol.*, **12**, 381–389.

Jacob, D., and Coauthors, 2014: Euro-CORDEX: New high-resolution climate change projections for European impact research. *Reg. Environ. Change*, **14**, 563–578, doi: 10.1007/s10113-013-0499-2.

Jansen, M., and R. Ferrari, 2009: Impact of the latitudinal distribution of tropical cyclones on ocean heat transport. *Geophys. Res. Lett.*, **36**, L06604, doi:10.1029/ 2008GL036796.

Jansen, M., R. Ferrari, and T. A. Mooring, 2010: Seasonal versus permanent thermocline warming by tropical cyclones. *Geophys. Res. Lett.*, **37**, L03602, doi:10.1029/ 2009GL041808.

Katsafados, P., E. Mavromatidis, A. Papadopoulos, and I. Pytharoulis, 2011: Numerical simulation of a deep Mediterranean storm and its sensitivity on sea surface temperature. *Nat. Hazards Earth Sys. Sci.*, **11**, 1233–1246, doi:10.5194/nhess-11-1233-2011.

Köhler, J., G. S. Völker, and M. Walter, 2018: Response of the internal wave field to remote wind forcing by tropical cyclones. *J. Phys. Oceanogr.*, **48**, 317–328, doi: 10.1175/JPO-D-17-0112.1.

Korty, R. L., K. A. Emanuel, and J. R. Scott, 2008: Tropical cyclone-induced upper-ocean mixing and climate: application to equable climates. *J. Climate*, **21**, 638–654.

Kroll, J., 1975: Propagation of wind-generated inertial oscillations from surface into deep ocean. *J. Mar. Res.*, **33**, 15–51.

Kundu, K. P., and R. E. Thomson, 1985: Inertial oscillations due to a moving front. *J. Phys. Oceanogr.*, **15**, 1076–1084.

Lagasio, M., A. Parodi, R. Procopio, F. Rachidi, and E. Fiori, 2017: Lightning potential index performances in multimicrophysical cloud-resolving simulations of a back-building mesoscale convective system: The genoa 2014 event. *J. Geophys. Res. Atmos.*, **122 (8)**, 4238–4257, doi:10.1002/2016JD026115.

Large, W. G., J. C. McWilliams, and S. C. Doney, 1994: Oceanic vertical mixing: a review and a model with a nonlocal boundary layer parametrization. *Rev. Geophys.*, **32**, 363–403.

Lebeaupin, C., V. Ducrocq, and H. Giordani, 2006: Sensitivity of torrential rain events to the sea surface temperature based on high-resolution numerical forecasts. *J. Geophys. Res.*, **111**, D12110, doi:10.1029/2005JD006541.

Lebeaupin Brossier, C., and P. Drobinski, 2009: Numerical high resolution air-sea coupling over the Gulf of Lions during two Tramontane/Mistral events. *J. Geophys. Res.*, **114**, D10110, doi:10.1029/2008JD011601.

Lebeaupin Brossier, C., P. Drobinski, K. Béranger, S. Bastin, and F. Orain, 2013: Ocean memory effect on the dynamics of coastal heavy precipitation preceded by a mistral event in the northwestern Mediterranean. *Quart. J. Roy. Meteor. Soc.*, **139**, 1583–1597, doi:10.1007/s10236-011-0502-8.

Ledwell, J. R., E. T. Montgomery, K. L. Polzin, L. C. S. L. andR. W. Schmitt, and J. M. Toole, 2000: Evidence for enhanced mixing over rough topography in the abyssal ocean. *Nature*, **403**, 179–182, doi:10.1038/35003164.

Ledwell, J. R., A. J. Watson, and C. S. Law, 1993: Evidence for slow mixing across the pycnocline from an open-ocean tracer-release experiment. *Nature*, **364**, 701–703.

Ledwell, J. R., A. J. Watson, and C. S. Law, 1998: Mixing of a tracer in the pycnocline. *J. Geophys. Res.*, **103**, 21 499–21 529.

Lemarié, F., L. Debreu, A. F. Shchepetkin, and J. C. McWilliams, 2012: On the stability and accuracy of the harmonic and biharmonic isoneutral mixing operators in ocean models. *Ocean Model.*, **52-53**, 9–35, doi:10.1016/j.ocemod.2012.04.007.

Li, Y., and R. E. Carbone, 2012: Excitation of rainfall over the tropical western Pacific. *J. Atmos. Sci.*, **69**, 2983–2994, doi:10.1175/JAS-D-11-0245.1.

Lighthill, M. J., 1978: *Waves in fluids.* Cambridge University Press, 504 pp.

Lindzen, R. S., and R. S. Nigam, 1987: On the role of the sea surface temperature gradients in forcing low level winds and convergence in the tropics. *J. Atmos. Sci.*, **44**, 2418–2436.

Lionello, P., G. Martucci, and M. Zampieri, 2003: Implementation of a coupled atmosphere-wave-ocean model in the Mediterranean sea: Sensitivity of the short time scale evolution to the air-sea coupling mechanisms. *J. Atmos. Ocean Sci.*, **9 (1-2)**, 65–95, doi:10.1080/1023673031000151421.

Liu, W. T., X. Xie, P. S. Polito, S.-P. Xie, and H. Hashizume, 2000: Atmospheric manifestation of tropical instability wave observed by QuikSCAT and tropical rain measuring mission. *Geophys. Res. Lett.*, **27**, 2545–2548, doi:10.1029/2000GL011545.

Llasat, M. C., M. Llasat-Botija, O. Petrucci, A. A. Pasqua, J. Rosselló, F. Vinet, and L. Boissier, 2013: Towards a database on societal impact of Mediterranean floods within the framework of the HYMEX project. *Nat. Hazards Earth Sys. Sci.*, **13**, 1337–1350, doi:10.5194/nhess-13-1337-2013.

Lucarini, V., and Coauthors, 2016: *Extremes and recurrence in dynamical systems.* Wiley, New York, NY, USA, 295 pp.

Marchesiello, P., L. Debreu, and X. Couvelard, 2009: Spurious diapycnal mixing in terrain-following coordinate models: The problem and a solution. *Ocean Model.*, **26**, 156–169, doi:10.1016/j.ocemod.2008.09.004.

McComas, C. H., and F. P. Bretherton, 1977: Resonant interaction of oceanic internal waves. *J. Geophys. Res.*, **82(9)**, 1397–1412.

McComas, C. H., and P. Müller, 1981: The dynamic balance of internal waves. *J. Phys. Oceanogr.*, **11**, 970–986.

Mei, W., C. Pasquero, and F. Primeau, 2012: The effect of translation speed upon the intensity of tropical cyclones over the tropical ocean. *Geophys. Res. Lett.*, **39**, L07801.

Mei, W., S.-P. Xie, F. Primeau, J. C. McWilliams, and C. Pasquero, 2015: Northwestern Pacific typhoon intensity controlled by changes in ocean temperatures. *Sci. Adv.*, **1 (4)**, doi:10.1126/sciadv.1500014.

Millán, M. M., J. Estrela, and V. Caselles, 1995: Torrential precipitations on the Spanish east coast: the role of the Mediterranean sea-surface temperature. *Atmos. Res.*, **36**, 1–16.

Minobe, S., A. Kuwano-Yoshida, N. Komori, S.-P. Xie, and R. J. Small, 2008: Influence of the Gulf Stream on the troposphere. *Nature*, **452**, 206–209, doi:10.1038/nature06690.

Mlawer, E., J. Steven, J. Taubman, P. D. Brown, M. J. Iacono, and S. A. Clough, 1997: Radiative transfer for inhomogenous atmospheres: RRTM, a validated correlated-k model for the longwave. *J. Geophys. Res.*, **102**, 16 663–16 682.

Müller, P., G. Holloway, F. Henyey, and N. Pomphrey, 1986: Nonlinear interactions among internal gravity waves. *Rev. Geophys.*, **24**, 493–536.

Munk, W., 1981: Internal wave and small-scale processes. *Evolution of physical oceanography*, B. A. Warren, and C. Wunsch, Eds., MIT Press, 264–291.

Munk, W., and C. Wunsch, 1998: Abyssal recipes II: energetics of tidal and wind mixing. *Deep-Sea Res. I*, **45**, 1977–2010.

Nakanishi, M., and H. Niino, 2006: An improved Mellor-Yamada level 3 model: its numerical stability and application to a regional prediction of advecting fog. *Boundary-Layer Meteor.*, **119**, 397–407.

Nakanishi, M., and H. Niino, 2009: Development of an improved turbulence closure model for the atmospheric boundary layer. *J. Meteor. Soc. Japan*, **87**, 895–912.

Nilsson, J., 1995: Energy flux from traveling hurricanes to the oceanic internal wave field. *J. Phys. Oceanogr.*, **25**, 558–573.

Niwa, Y., and T. Hibiya, 1997: Nonlinear processes of energy transfer from traveling hurricanes to the deep ocean internal wave field. *J. Geophys. Res.*, **102**, 12 469–12 477.

Nuissier, O., V. Ducrocq, D. Ricard, C. Lebeaupin, and S. Anquetin, 2008: A numerical study of three catastrophic precipitating events over southern France. I: Numerical framework and synoptic ingredients. *Quart. J. Roy. Meteor. Soc.*, **134**, 111–130, doi: 10.1002/qj.200.

Nuissier, O., B. Joly, A. Joly, V. Ducrocq, and P. Arbogast, 2011: A statistical downscaling to identify the large-scale circulation patterns associated with heavy precipitation events over southern France. *Quart. J. Roy. Meteor. Soc.*, **137 (660)**, 1812–1827, doi:10.1002/qj.866.

Oddo, P., M. Adani, N. Pinardi, C. Fratianni, M. Tonani, and D. Pettenuzzo, 2009: A nested Atlantic-Mediterranean Sea general circulation model for operational forecasting. *Ocean Sci.*, **5**, 461–473, doi:10.5194/os-5-461-2009.

Olbers, D., and C. Eden, 2013: A global model for the diapycnal diffusivity induced by internal gravity waves. *J. Phys. Oceanogr.*, **43**, 1759–1779, doi:10.1175/JPO-D-12-0207.1.

Olbers, D., J. Willebrand, and C. Eden, 2012: *Ocean dynamics*. 1st ed., Springer, 708 pp.

Olbers, D. J., 1974: *On the energy balance of small-scale internal waves in the deep sea.* Hamburger Geophysikalische Einzelschriften, 91 pp.

Olbers, D. J., 1976: Nonlinear energy transfer and the energy balance of the internal wave field in the deep ocean. *J. Fluid Mech.*, **74**, 375–399, doi:10.1017/S0022112076001857.

O'Neill, L. W., D. B. Chelton, and S. K. Esbensen, 2010: The effects of SST-induced surface wind speed and direction gradients on midlatitude surface vorticity and divergence. *J. Climate*, **23**, 255–281, doi:10.1175/2009JCLI2613.1.

Orlanski, I., 1976: A simple boundary condition for unbounded hyperbolic flows. *J. Comp. Sci.*, **21 (3)**, 251–269.

Parodi, A., L. Ferraris, W. Gallus, M. Maugeri, L. Molini, F. Siccardi, and G. Boni, 2017: Ensemble cloud-resolving modelling of a historic back-building mesoscale convective system over Liguria: the San Fruttuoso case of 1915. *Clim. Past*, **13**, 455–472, doi: 10.5194/cp-13-455-2017.

Pasquero, C., 2016: A theoretical introduction to atmospheric and oceanic convection. *The fluid dynamics of climate*, A. Provenzale, E. Palazzi, and K. Fraedrich, Eds., Springer, 39–60.

Pasquero, C., and K. Emanuel, 2008: Tropical cyclones and transient upper-ocean warming. *J. Climate*, **21**, 149–162.

Pastor, F., M. J. Estrela, D. P. narrocha, and M. M. Millán, 2001: Torrential rains on the Spanish Mediterranean coast: modeling the effects of the sea surface temperature. *J. Appl. Meteor.*, **40**, 1180–1195.

Pastor, F., J. A. Valiente, and M. J. Estrela, 2015: Sea surface temperature and torrential rains in the Valencia region: modeling the role of recharge areas. *Nat. Hazards Earth Sys. Sci.*, **15**, 1677–1693, doi:10.5194/nhess-15-1677-2015.

Penven, P., L. Debreu, P. Marchesiello, and J. C. McWilliams, 2006: Evaluation and application of the ROMS 1-way embedding procedure to the central California upwelling system. *Ocean Model.*, **12**, 157–187.

Phillips, O. M., 1966: *The dynamics of the upper ocean.* 1st ed., Cambridge University Press, 261 pp.

Pickard, G. L., and W. J. Emery, 1990: *Descriptive physical oceanography.* 5th ed., Pergamon Press, 321 pp.

Pinto, J. G., S. Ulbrich, A. Parodi, R. Rudari, G. Boni, and U. Ulbrich, 2013: Identification and ranking of extraordinary rainfall events over Northwest Italy: The role of Atlantic moisture. *J. Geophys. Res. Atmos.*, **118 (5)**, 2085–2097, doi:10.1002/jgrd.50179.

Pollard, R. T., 1970: On the generation by winds of inertial waves in the ocean. *Deep-Sea Res. I*, **17**, 795–812.

Polzin, K. L., J. M. Toole, J. R. Ledwell, and R. W. Schmitt, 1997: Spatial variability of turbulent mixing in the abyssal ocean. *Science*, **276(5309)**, 93–96.

Pomphrey, N., J. D. Meiss, and K. M. Watson, 1980: Description of nonlinear internal wave interactions using Langevin methods. *J. Geophys. Res.*, **85(C2)**, 1085–1094.

Press, W. H., S. A. Teukolsky, W. T. Vetterling, and B. P. Flannery, 1992: *Numerical recipes in C.* 2nd ed., Cambridge University Press, 925 pp.

Price, J. F., 1981: Upper ocean response to a hurricane. *J. Phys. Oceanogr.*, **11**, 153–175.

Price, J. F., 1983: Internal wave wake of a moving storm. Part I: scales, energy budget and observations. *J. Phys. Oceanogr.*, **13**, 949–965.

Ragone, F., J. Wouters, and F. Bouchet, 2017: Computation of extreme heat waves in climate models using a large deviation algorithm. *ArXiv e-prints*, `1709.03757`.

Raymond, W. H., and H. L. Kuo, 1984: A radiation boundary condition for multi-dimensional flows. *Quart. J. Roy. Meteor. Soc.*, **110**, 535–551.

Rebora, N., and Coauthors, 2013: Extreme rainfall in the mediterranean: what can we learn from observations? *J. Hydrometeor.*, **14**, 906–922, doi:10.1175/JHM-D-12-083.1.

Ricard, D., C. Lac, S. Riette, R. Legrand, and A. Mary, 2013: Kinetic energy spectra characteristics of two convection-permitting limited-area models AROME and Meso-NH. *Quart. J. Roy. Meteor. Soc.*, **139 (674)**, 1327–1341, doi:10.1002/qj.2025.

Ricchi, A., M. M. Miglietta, P. P. Falco, A. Benetazzo, D. Bonaldo, A. Bergamasco, M. Sclavo, and S. Carniel, 2016: On the use of a coupled-ocean-atmosphere-wave model during an extreme cold air outbreak over the Adriatic Sea. *Atmos. Res.*, **172-173**, 48–65, doi:10.1016/j.atmosres.2015.12.023.

Ricchi, A., and Coauthors, 2017: Sensitivity of a Mediterranean tropical-like cyclone to different model configurations and coupling strategies. *Atmosphere*, **8 (92)**, doi:10.3390/atmos8050092.

Ripa, P., 1981: On the theory of nonlinear wave-wave interactions among geophysical waves. *J. Fluid Mech.*, **103**, 87–115.

Romero, R., G. Sumner, C. Ramis, and A. Genovés, 1999: A classification of the atmospheric circulation patterns producing significant daily rainfall in the Spanish Mediterranean area. *Int. J. Climatol.*, **19**, 765–785.

Rubenstein, D., 1994: A spectral model of wind-forced internal waves. *J. Phys. Oceanogr.*, **24**, 819–831.

Rudari, R., D. Entekhabi, and G. Roth, 2005: Large-scale atmospheric patterns associated with mesoscale features leading to extreme precipitation events in northwerstern Italy. *Adv. Water Resour.*, **28**, 601–614, doi:10.1016/j.advwatres.2004.10.017.

Samson, G., H. Giordani, G. Caniaux, and F. Roux, 2009: Numerical investigation of an oceanic resonant regime induced by hurrican winds. *Ocean Dyn.*, **59**, 565–586, doi:10.1007/s10236-009-0203-8.

Sandwell, D. T., and W. H. F. Smith, 1997: Marine gravity anomaly from Geosat and ERS 1 satellite altimetry. *J. Geophys. Res.*, **102**, 10 039–10 054, doi:10.1029/96JB03223.

Sanford, T. B., J. F. Price, J. B. Girton, and D. C. Webb, 2007: Highly resolved observations and simulations of the ocean response to a hurricane. *Geophys. Res. Lett.*, **34**, doi:10.1029/2007GL029679.

Schade, L. R., and K. A. Emanuel, 1999: The ocean's effect on the intensity of tropical cyclones: Results from a simple coupled atmosphere-ocean model. *J. Atmos. Sci.*, **56**, 642–651.

Schumacher, R. S., and R. H. Johnson, 2005: Organization and environmental properties of extreme-rain-producing mesoscale convective systems. *Mon. Wea. Rev.*, **133**, 961–976.

Schumacher, R. S., and R. H. Johnson, 2008: Mesoscale processes contributing to extreme rainfall in a midlatitude warm-season flash-flood. *Mon. Wea. Rev.*, **136**, 3964–3986.

Schumacher, R. S., and R. H. Johnson, 2009: Quasi-stationary, extreme-rain-producing convective systems associated with midlevel cyclonic circulations. *Wea. Forecasting*, **24**, 555–574.

Shay, L. K., R. L. Elseberry, and P. G. Black, 1989: Vertical structure of the ocean current response to a hurricane. *J. Phys. Oceanogr.*, **19**, 649–669.

Shchepetkin, A. F., 2015: An adaptive, courant-number-dependent implicit scheme for vertical advection in oceanic modeling. *Ocean Model.*, **91**, 38–69, doi:10.1016/j.ocemod.2015.03.006.

Shchepetkin, A. F., and J. C. McWilliams, 1998: Quasi-monotone advection schemes based on explicit locally adaptive dissipation. *Mon. Wea. Rev.*, **126**, 1541–1580, doi:10.1175/1520-0493(1998)126<1541:QMASBO>2.0.CO;2.

Shchepetkin, A. F., and J. C. McWilliams, 2003: A method for computing horizontal pressure-gradient force in an oceanic model with a nonaligned vertical coordinate. *J. Geophys. Res.*, **108(C3)**, doi:10.1029/2001JC001047.

Shchepetkin, A. F., and J. C. McWilliams, 2009: Correction and commentary for "Ocean forecasting in terrain-following coordinates: Formulation and skill assessment of the regional ocean modeling system" by Haidvogel et al., J. Comp. Phys. 227, pp. 3595-3624. *J. Comput. Phys.*, **228**, 3595–3624, doi:10.1016/j.jcp.2009.09.002.

Silvestro, F., N. Rebora, F. Giannoni, A. Cavallo, and L. Ferraris, 2015: The flash flood of the Bisagno creek on 9th October 2014: an "unfortunate" combination of spatial and temporal scales. *J. Hydrol.*, doi:10.1016/j.jhydrol.2015.08.004.

Simmons, A. J., D. M. Burridge, M. Jarraud, C. Girard, and W. Wergen, 1989: The ECMWF medium-range prediction models development of the numerical formulations and the impact of increased resolution. *Meteor. Atmos. Phys.*, **40**, 28–60.

Sjöberg, B., and A. Stigebrandt, 1992: Computations of the geographical distribution of the energy flux to mixing processes via internal tides and the associated vertical circulation in the ocean. *Deep-Sea Res. I*, **39**, 269–291.

Skamarock, W. C., and Coauthors, 2008: A description of the Advanced Research WRF Version 3. *NCAR Tech. Note NCAR/TN-475+STR*, 113 pp., doi:10.5065/D68S4MVH.

Skyllingstad, E. D., D. Vickers, and L. Mahrt, 2007: Effects of mesoscale sea-surface temperature fronts on the marine atmospheric boundary layer. *Boundary-Layer Meteor.*, **123**, 219–237, doi:10.1007/s10546-006-9127-8.

Smagorinsky, J., 1963: General circulation experiments with the primitive equations: I. The basic equations. *Mon. Wea. Rev.*, **91**, 99–164.

Small, R. J., T. Campbell, J. Teixeira, S. Carniel, T. A. Smith, J. Dykes, S. Chen, and R. Allard, 2011: Air-sea interaction in the Ligurian sea: assessment of a coupled ocean-atmosphere model using in situ data from LASIE07. *Mon. Wea. Rev.*, **139**, 1785–1808, doi:10.1175/2010MWR3431.1.

Small, R. J., S. Carniel, T. Campbell, J. Teixeira, and R. Allard, 2012: The response of the Ligurian and Tyrrhenian Seas to a summer Mistral event: a coupled atmosphere–ocean approach. *Ocean Model.*, **48**, 30–44, doi:10.1016/j.ocemod.2012.02.003.

Small, R. J., S. P. deSzoeke, S.-P. Xie, L. O'Neilland H. Seo, Q. Song, P. Cornillon, M. Spall, and S. Minobe, 2008: Air-sea interaction over ocean fronts and eddies. *Dyn. Atmos. Oceans*, **45**, 274–319, doi:10.1016/j.dynatmoce.2008.01.001.

Song, Q., P. Cornillon, and T. Hara, 2006: Surface wind response to oceanic fronts. *J. Geophys. Res.*, **111**, L12605, doi:10.1029/2006JC003680.

Spall, M. A., 2007: Midlatitude wind stress-sea surface temperature coupling in the vicinity of oceanic fronts. *J. Climate*, **20**, 3785–3801, doi:10.1175/JCLI4234.1.

Sriver, R. L., and M. Huber, 2007: Observational evidence for an ocean heat pump induced by tropical cyclones. *Nature*, **447**, 577–580.

Staquet, C., and J. Sommeria, 2002: Internal gravity waves: from instabilities to turbulence. *Annu. Rev. Fluid Mech.*, **34**, 559–593.

Sutherland, B. R., 2016: Excitation of superharmonics by internal modes in non-uniformly stratified fluid. *J. Fluid Mech.*, **793**, 335–352, doi:10.1017/jfm.2016.108.

Takatama, K., S. Minobe, M. Inatsu, and R. J. Small, 2012: Diagnostics for near-surface wind convergence/divergence response to the Gulf Stream in a regional atmospheric model. *Atmos. Sci. Lett.*, **13**, 16–21, doi:10.1002/asl.355.

Takatama, K., S. Minobe, M. Inatsu, and R. J. Small, 2015: Diagnostics for near-surface wind response to the Gulf Stream in a regional atmospheric model. *J. Climate*, **28**, 238–255, doi:10.1175/JCLI-D-13-00668.1.

Thorpe, S. A., 2005: *The turbulent ocean.* 1st ed., Cambridge University Press, 439 pp.

Tiedtke, M., 1989: A comprehensive mass flux scheme for cumulus parameterization in large-scale models. *Mon. Wea. Rev.*, **117**, 1779–1800.

Touchette, H., 2009: The large deviation approach to statistical mechanics. *Phys. Rep.*, **478 (1)**, 1–69, doi:10.1016/j.physrep.2009.05.002.

Toy, M. D., and R. H. Johnson, 2014: The influence of an SST front on a heavy rainfall event over the coastal Taiwan during TiMREX. *J. Atmos. Sci.*, **71**, 3223–3249, doi: 10.1175/JAS-D-13-0338.1.

Trenberth, K. E., J. T. Fasullo, and J. Kiehl, 2009: Earth's global energy balance. *Bull. Amer. Meteor. Soc.*, **90 (3)**, 311–323, doi:10.1175/2008BAMS2634.1.

Valcke, S., 2013: The OASIS3 coupler: A European climate modelling community software. *Geosci. Model Dev.*, **6**, 373–388, doi:10.5194/gmd-6-373-2013.

Vallis, G. K., 2006: *Atmospheric and oceanic fluid dynamics*. Cambridge University Press, Cambridge, U.K., 745 pp.

Wagner, G. L., and W. R. Young, 2016: A three-component model for the coupled evolution of near-inertial waves, quasi-geostrophic flow and the near-inertial second harmonic. *J. Fluid Mech.*, in press.

Wallace, J. M., and P. V. Hobbs, 2006: *Atmospheric science - An introductory survey*. 2nd ed., Elsevier Academic Press, 483 pp.

Wallace, J. M., T. P. Mitchell, and C. Deser, 1989: The influence of sea surface temperature on surface wind in the eastern equatorial Pacific: Seasonal and interannual variability. *J. Climate*, **2**, 1492–1499.

Waterhouse, A. F., and Coauthors, 2014: Global patterns of diapycnal mixing from measurements of the turbulent dissipation rate. *J. Phys. Oceanogr.*, **44**, 1854–1872, doi:10.1175/JPO-D-13-0104.1.

Whalen, C. B., L. D. Talley, and J. A. Mackinnon, 2012: Spatial and temporal variability of global ocean mixing inferred from Argo profiles. *Geophys. Res. Lett.*, **39**, L18612, doi:10.1029/2012GL053196.

Wyngaard, J. C., 2004: Toward numerical modeling in the "Terra Incongnita". *J. Atmos. Sci.*, **61 (14)**, 1816–1826, doi:10.1175/1520-0469(2004)061<1816:TNMITT>2.0.CO; 2.

Xie, X., Q. Liu, X. Shang, G. Chen, and D. Wang, 2016: Poleward propagation of parametric subharmonic instability-induced inertial waves. *J. Geophys. Res. Oceans*, **121**, 1881–1895, doi:10.1002/2015JC011194.

Zedler, S. E., 2009: Simulations of the ocean response to a hurricane: nonlinear processes. *J. Phys. Oceanogr.*, **39**, 2618–2634, doi:10.1175/2009JPO4062.1.

Zhang, C., Y. Wang, and K. Hamilton, 2011: Improved representation of boundary layer clouds over the southeast Pacific in ARW-WRF using a modified Tiedtke cumulus parameterization scheme. *Mon. Wea. Rev.*, **139**, 3489–3513.